1997

Data Analysis of the Allegro Gravitational Wave Detector.

Evan Mauceli
Louisiana State University and Agricultural & Mechanical College

INFORMATION TO USERS

This manuscript has been reproduced from the microfilm master. UMI films the text directly from the original or copy submitted. Thus, some thesis and dissertation copies are in typewriter face, while others may be from any type of computer printer.

The quality of this reproduction is dependent upon the quality of the copy submitted. Broken or indistinct print, colored or poor quality illustrations and photographs, print bleedthrough, substandard margins, and improper alignment can adversely affect reproduction.

In the unlikely event that the author did not send UMI a complete manuscript and there are missing pages, these will be noted. Also, if unauthorized copyright material had to be removed, a note will indicate the deletion.

Oversize materials (e.g., maps, drawings, charts) are reproduced by sectioning the original, beginning at the upper left-hand corner and continuing from left to right in equal sections with small overlaps. Each original is also photographed in one exposure and is included in reduced form at the back of the book.

Photographs included in the original manuscript have been reproduced xerographically in this copy. Higher quality 6" x 9" black and white photographic prints are available for any photographs or illustrations appearing in this copy for an additional charge. Contact UMI directly to order.

UMI

A Bell & Howell Information Company
300 North Zeeb Road, Ann Arbor MI 48106-1346 USA
313/761-4700 800/521-0600

DATA ANALYSIS OF THE ALLEGRO GRAVITATIONAL WAVE DETECTOR

A Dissertation

Submitted to the Graduate Faculty of the
Louisiana State University and
Agricultural and Mechanical College
in partial fulfillment of the
requirements for the degree of
Doctor of Philosophy

in

The Department of Physics and Astronomy

by
Evan Mauceli
B.S., University of New Hampshire, 1989
August 1997

Acknowledgments

There is no possible way I could begin this section other than by thanking my family. Mom. Dad. Delia and the rest of them out there (you know who you are. don't try to deny it), whose love and support made this thesis possible.

Of course. it is to my advisors Bill Hamilton and Warren Johnson that I owe any scientific ability that I now possess. "Green as grass" is how Bill likes to describe new and inexperienced graduate students and I was a green 'un upon arrival in the gravity lab. Bill let me muddle my way around until I found something interesting to do and then he let me go do it. I appreciate both the freedom he allowed me and the patience he showed towards me.

Warren Johnson was extremely helpful in all aspects of my research, but especially the pulsar search. His ability to look at a graph, ask what it is supposed to be, and then comment on whether it is right or not -and be correct- is frankly amazing. Conversations with him almost always solved a particular problem I was faced with or otherwise moved the project along in some fashion.

Old friends who have since moved on have not been forgotten. My first few years at LSU were a lot of fun thanks to Jai-Won, Vandana, and Jyotsna. Steve.

the clothes-lining, bolo-playing hacker himself was a pleasure to work and shoot hoops with. Norbert and Kenny were talented experimentalists who helped me get acquainted with the lab. There are many friends still around - Andrew, Erik, Ken, Brad (former computer guru), Philip (recent computer guru), Patrick and Paul - all of whom keep things lively. Special thanks go out to Tammy (Erik's wife) for many an excellent meal (and putting up with "the guys").

I also must thank Martin McHugh for many extremely helpful discussions on my thesis and Sam Finn for his tutorials on the DFT and the Bayesian approach to data analysis. Sam also deserves the credit for the *very* fast MATLAB version of the Allegro model. Thanks Sam.

Finally, I have to thank Karla Lockwood, Karen Richard, Beverly Rodriguez, Karen Cashio and Cathy Mixon. The fact that I don't even know how much work they have done on my behalf is a testament to how good they are at their jobs. All I know is that they made being a graduate student very easy.

This research was supported by the National Science Foundation under Grant No. PHY-9311731.

Contents

Abstract

The Allegro gravitational wave detector has been operational from 1991-1994, and 1996-present. We present a detailed description of the detector and the data acquisition system. Two distinct types of data analysis are detailed.

First, we describe the search for burst sources of gravitational radiation. These are impulse forces acting on the bar, presumably from the stellar collapse associated with supernovae. Construction of the optimal filter for burst signals is described, as well as its application to the data from the detector. The uncertainties introduced into timing and signal strength estimates due to stationary noise are measured, giving the windows for both quantities in coincidence searches.

Second, we describe a very different type of analysis, the search for a continuous source of gravitational radiation from a rotating neutron star. Unlike the burst events which last on the order of a millisecond, this signal is expected to persist for the duration of the experiment. Since Allegro is sensitive at frequencies near 1 kHz, only neutron stars with spin periods near 2 ms are potential sources. Since there are no known sources of this type for Allegro, we directed the search towards the globular cluster 47 Tucanae. This was due to the large number of millisecond

pulsars located there. No claim to have detected a CW signal is made, although a number of candidates are identified. The analysis puts a constraint of 3×10^{-24} on the gravitational strain emitted from a pulsar in 47 Tucanae.

Chapter 1

Introduction

In General Relativity (GR), gravitation is expressed as a curvature of space and time produced by the presence of matter. If the matter is accelerating, then GR predicts that propagating oscillations in space and time, called gravity waves, could be produced. This is analogous to accelerating charges producing electromagnetic radiation. Unlike the electromagnetic case where it is the dipole moment of the charge distribution which provides the largest contribution to the radiation, it is the quadrupole moment of a mass distribution which produces gravity waves. Conservation of mass excludes monopole radiation and conservation of momentum excludes dipole gravitational radiation. Gravity waves produce a fluctuating strain force perpendicular to the direction of propagation which changes the proper distance between particles. The force is tidal, so that the larger the initial separation between the particles, the greater the force. The effects of a passing gravity wave on a ring of particles is shown in Fig. 1.1.

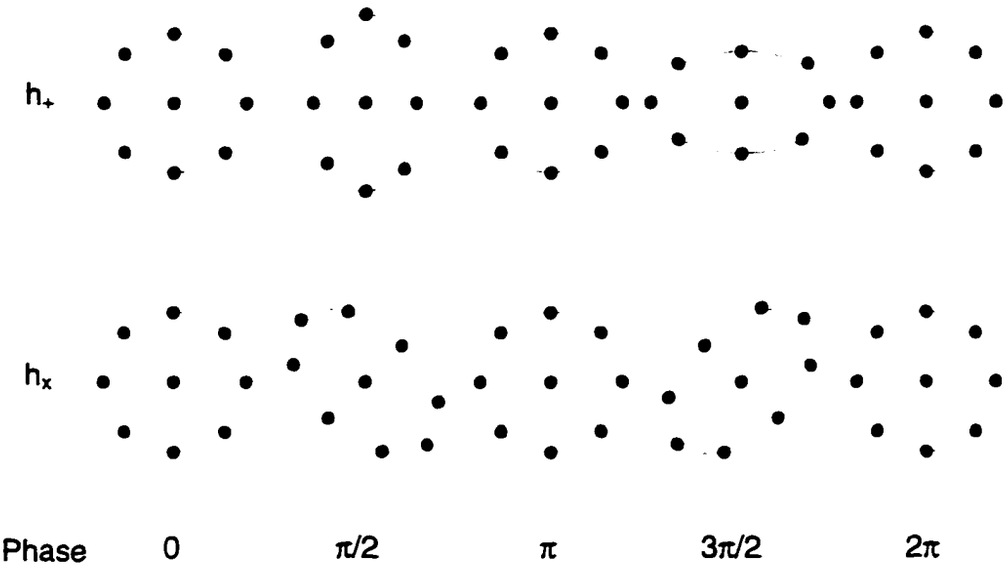

Figure 1.1: The distortion of a ring of test particles during one cycle of a gravitational wave traveling into the page. The effect of both linear polarizations is shown.

If the mass distribution producing the gravity waves is small compared to the wavelength of the wave then the amplitude of the strain can be calculated from the quadrupole approximation

$$h \sim \frac{G}{c^4 r}\frac{d^2 I}{dt^2}$$

where I is the quadrupole moment of the source, r is the distance to the source. c is the speed of light and G the gravitational constant. The second time derivative of I has units of energy and is essentially the kinetic energy of the quadrupole moment of the source. That the emitted gravity waves are small is readily seen from the factor $G/c^4 = 8 \times 10^{-45}\ \mathrm{s^2\,kg^{-1}\,m^{-1}}$. For laboratory sized objects (kilogram masses moving meters in seconds) an emitted gravitational wave changes the distance between two nearby objects by $\sim 10^{-44}$ m. This is such a small change there is nothing small enough to compare it to.

It is only through astrophysical systems where stellar-sized objects can be moving at speeds approaching the speed of light that gravity waves can be produced with large enough amplitude to be observed. Supernovae, stellar collapses to black holes, non-axisymmetric pulsars, inspiralling binary star systems, and black hole collisions are all examples of systems expected to emit gravity waves. There is only a limited amount of information which can be obtained from these systems using electromagnetic radiation because the radiation interacts strongly with matter producing the gravity waves. The gravity waves themselves, however, propagate fairly undisturbed by external influences. Therefore it is expected that gravity wave astronomy will open a new window to the universe.

1.1 A Brief History of Gravitational Wave Detectors

The effort to detect gravity waves was pioneered in the early 1960's by Weber [1]. He constructed the first resonant mass antenna, a one and a half ton aluminum right cylindrical bar operating in a vacuum and at room temperature. Piezoelectric crystal sensors were glued to the bar to detect the strain produced by a passing gravity wave. By 1969 he had achieved strain sensitivities of a few parts in 10^{16}. He operated several more detectors and his claims to have observed coincidences between them [2] generated a good deal of excitement. Other groups attempted to reproduce his results, without success.

In the early 1970's detectors with a number of improvements over Weber's original design were being proposed. One improvement was to cool the antenna to liquid helium temperatures (4 K), thus suppressing the thermal Brownian motion of the antenna [3]. Seismic motion was reduced by better vibration isolation systems. Finally, a resonant transducer with a low noise amplifier was attached to the bar to amplify mechanical vibrations and convert them to an electronic signal [4]. There are currently three detectors of this lineage operational: The Allegro detector at Louisiana State University [5], the Rome Explorer detector [6] and the Australian Niobe detector [7]. There are also bar detectors at Rome (Nautilus) and Legnaro (Auriga) which are designed to operate at ultra-low temperatures (50 mK), further reducing the Brownian noise.

The currently running detectors are sensitive enough to detect a gravity wave from a "reasonably" asymmetric (a few percent of a solar mass converted to gravitational radiation) supernova collapse in our galaxy. Unfortunately, the event rate of supernovae in our galaxy is on the order of one or two per century. To get an event rate of a few per year, detectors need look out to the Virgo cluster of galaxies, three order of magnitude further in distance. This requires major improvements in detector sensitivity.

Three ideas have been proposed for the next generation of detectors. The first proposal is to make a spherical resonant mass detector cooled to millikelvin temperatures. Although the idea has been around for twenty years [8], it has been only recently that a sphere has been shown to be a practical detector [9]. A spherical detector is much more massive for a given resonant frequency than is a bar.

increasing its gravitational wave cross-section. A sphere also has full sky coverage, so a gravity wave incident from any direction will impart the same momentum to the antenna. This feature also allows for a single sphere to determine the direction from which a gravity wave came. Proposals to build spherical detectors have been made in the U.S. (the TIGA project), Italy (OMEGA) and the Netherlands (GRAIL).

The second type of detector design is a Fabry-Perot laser interferometer. A passing gravity wave extends the length of one arm of the interferometer while shrinking the length of the other, creating a shift in the phase of the recombined laser light. The longer the arms of the interferometer, the more sensitive the detector will be. Current designs propose arm lengths of 3-4 km. The advantage of the interferometer is that it is sensitive to gravity waves in a frequency range from 100 Hz to 1 kHz. The low frequency sensitivity is limited by seismic noise, the high frequency limit is due to photon shot noise. The increased bandwidth potentially allows for the shape of the gravitational waveform to be measured. The target source for the laser interferometers is the last few minutes of an inspiraling, high-mass binary star systems. Many groups across the world are currently involved in building such detectors. The most ambitious projects are LIGO in the U.S. [10] and VIRGO in Italy [11].

The LISA project [12] involves putting a laser interferometer detector into space. Because LISA will not in be in contact with the ground, it will not be limited by seismic noise at lower frequencies. Being in space also enables the design to incorporate a much longer baseline for the arms of the interferometer. The

proposal calls for six spacecraft to form a rough triangle with two of the spacecraft at each vertex. The spacecraft would function together as a Michelson interferometer. The detector would be in heliocentric orbit and have "arm lengths" (distance between pairs of spacecraft) of roughly 5×10^6 km. Its target source is inspiralling binary systems. but since it will be sensitive at frequencies from 10^{-1} Hz to 10^{-4} Hz. LISA will be able to detect binary systems much earlier in their development than will be possible for any ground based detector.

1.2 Gravity Wave Astronomy

Observations of the binary pulsar PRR 1913 +16 have produced the most information on gravitational radiation yet available [13]. Most important is the determination that the orbit is decaying at precisely the rate predicted by the emission of gravitational radiation from GR. The orbital parameters of the binary system. including the masses of the pulsar and its companion. have been specified. Other interesting applications of the data have also been explored. such as setting upper limits to the to the energy density of a background of very low frequency gravity waves [13].

Although none of the current generation of gravitational wave detectors has detected gravity waves. a small amount of astronomical information has been obtained. There have been a number of searches for coincident burst events conducted between various detectors. In 1986 a coincidence search involving a detector located at Stanford University. the Allegro detector. and the Explorer detector was made to look for burst events [14]. Searches have also been conducted between

Allegro and Explorer in 1991 [15] and 1994. None of these searches resulted in a claim to have detected gravity waves, but upper limits were established to the incident flux of gravity waves at the Earth. In 1993 Explorer and Allegro made a directed search for evidence of gravitational radiation from supernova 1993J, again with no detection made.

Others have searched for sources of continuous gravitational radiation (CW radiation) from non-axisymmetric pulsars. The Crab detector operated by the University of Tokyo has searched for gravitational radiation from the Crab pulsar. They used a resonant mass detector tuned to the frequency of the radiation emitted by the Crab and have set an upper limit of 2×10^{-22} to the strain amplitude from the Crab pulsar [16]. Two groups (Garching and Glasgow) have used prototype laser interferometers to search for evidence of CW radiation from the supernova 1987A remnant. The Garching detector established an upper limit to the strain amplitude from a potential pulsar of 9×10^{-21} at frequencies near 2 and 4 kHz [17]. The Glasgow detector obtained an upper limit of 2×10^{-21} near 934 Hz.

There are two advantages of a single detector when searching for CW radiation as opposed to searching for burst events. 1) A CW signal can be integrated for a long time, increasing the signal to noise ratio and therefore its detectability. 2) Burst "events" occur frequently in detectors due possibly to gravity waves but more likely due to a more prosaic cause. A single detector cannot always distinguish between an event caused by some local disturbance and a gravity wave (although some events due to local disturbances can be identified as such and ruled out as potential gravity waves). To combat this problem it is necessary to have two or

more detectors operating in coincidence to separate the "candidate" events from the noise. For a CW search, the situation is much different. Because the radiation is expected to last longer than the operational time of the detector, a "trial" search can be made on a particular stretch of data. Then another trial can made on a different stretch. If the signal is observed in one trial and also in the other, then this is a positive check on the reality of the signal.

1.3 Millisecond Pulsars

The Allegro gravitational wave detector is sensitive to radiation at frequencies near 1 kHz. As shown in section 3.1, a non-axisymmetric pulsar will emit gravitational radiation at twice its rotation frequency. If the pulsar is precessing, then it can produce radiation at both its rotation frequency and twice the rotation frequency. To produce gravitational waves detectable by Allegro requires the pulsar to have a spin period of roughly 2 ms, which is fast for millisecond pulsars. In this section we give a brief review of the current understanding of millisecond pulsars.

Millisecond pulsars are characterized by high rotation rates and low surface dipole magnetic fields (10^8G vs. 10^{12}G for ordinary pulsars). Although there is nothing prohibiting pulsars from being born with a high rotation rate (the Crab pulsar is believed to have been born with a period of 16 ms) the standard explanation is that millisecond pulsars are old pulsars which have been spun up by accretion from a companion star. Accretion rates are limited by radiation pressure from the accreting star (the Eddington limit) and it is expected to take $> 10^8$ years for a pulsar to accrete enough matter to be spun up to millisecond periods.

This implies a low mass companion ($\sim 1 M_{\odot}$) since one of significantly higher mass evolves too quickly for the neutron star to reach the fastest rotational rates. The accretion onto the neutron star produces x-rays and these have been detected (low mass x-ray binary systems - LMXB). Recently, there have been direct observations of millisecond pulsars in LMXB systems, lending experimental support to the hypothesis of spin up through accretion [18].

The question of the low magnetic field strengths of millisecond pulsars remains a mystery. It is possible that the accretion process itself leads to field reduction, but not all the observations of millisecond pulsars support this hypothesis.

The existence of solitary millisecond pulsars (not in binary systems) is also somewhat of a mystery. The first millisecond pulsar discovered (PSR 1937 +21), which is also the fastest with a period of 1.56 ms, is a not in a binary orbit. One theory is that radiation from the pulsar ablated its companion. Another theory suggests that the supernova which formed the pulsar gives it a "kick" towards the companion star. The companion is disrupted, an accretion disk is formed around the pulsar and the neutron star is sped up as described previously. This also provides an explanation of the observed planetary pulsar systems, where the planetary body forms from the remains of the disrupted star.

Chapter 2

The Allegro Gravitational Wave Detector[1]

In this chapter we present a detailed description of the Allegro gravitational wave detector and of the data analysis used to look for sources of burst gravitational radiation. This chapter reproduces our discussion, with minor changes, published in Physical Review D [19], copyright 1996 The American Physical Society (see Appendix D for letter of permission).

Allegro is located in the Physics Building at Louisiana State University in Baton Rouge, Louisiana ($30° 25' N$, $91° 10' W$). It consists of a resonant bar equipped with a resonant inductive transducer and a dc SQUID amplifier all cooled to 4.2 K. It was operational from June 1991 until January of 1995 with a duty cycle approaching 95% and an average noise temperature (defined in section 2.3) less than 6 mK. Allegro started taking data again in January of 1996 and has run since then with a similar duty cycle and slightly higher noise temperature. Figure 2.1 shows a

[1]Reprinted with permission from *Physical Review D* 54,1264 (1996), "The Allegro gravitational wave detector: Data acquisition and analysis" by E. Mauceli et al. Copyright 1996 The American Physical Society.

schematic of the antenna. The schematic shows the mechanical isolator, the bar, and a close view of the transducer.

2.1 The Detector

2.1.1 The Bar

The Allegro detector was designed to look for pulses of gravity waves such as those from the collapse of a massive star. Theoretical models (although varying widely in waveform and strength estimates) predict that stellar collapse to a neutron star or black hole would produce a burst of gravitational radiation with a duration on the order of milliseconds at frequencies near 1 kHz. For a resonant mass detector, a passing gravity wave deposits momentum into a massive elastic body, changing the amplitude and phase of the existing vibrational normal mode motion. The elastic body in the Allegro detector is a cylinder of aluminum alloy 5056, 60 cm in diameter and 300 cm in length. It has a physical mass of 2296 kg. Its first longitudinal normal mode is at 913 Hz. All cylinder detectors are most sensitive to signals propagating in a direction perpendicular to the bar axis. The bar is oriented perpendicular to the plane of the great circle on the earth that passes through Geneva, the location of the Rome Explorer antenna, and midway between Baton Rouge, LA and Stanford, CA. This orientation results in the axis of Allegro being directed along a line $40^\circ\,24'$ west of North. The Explorer detector of the University of Rome is perpendicular to the same great circle and as a result is parallel to Allegro. This means that a gravity wave should deposit the same amount of momentum into each of the detectors.

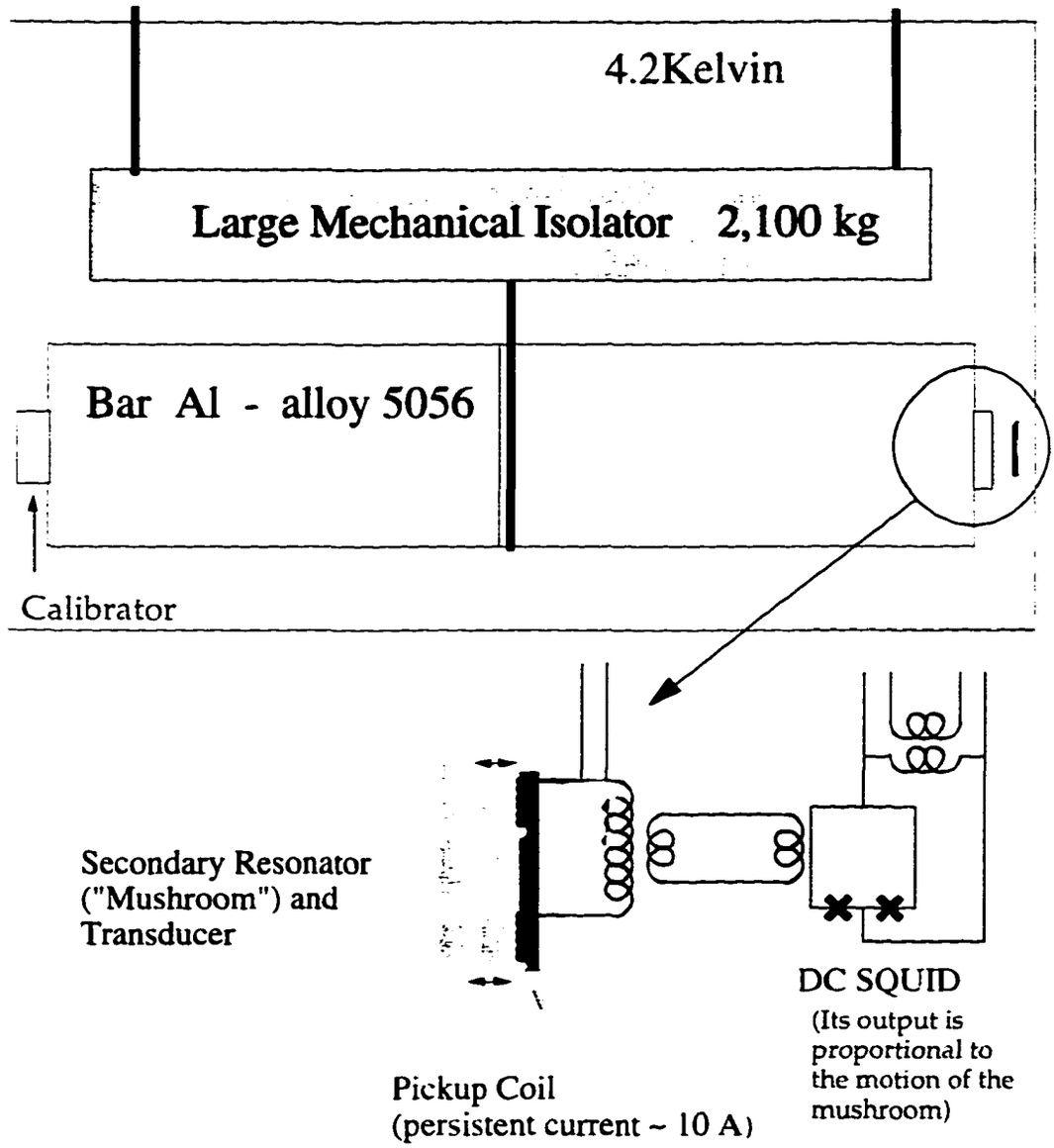

Figure 2.1: The schematic of the Allegro antenna.

2.1.2 The Transducer

Attached to one end of the bar is a smaller "mushroom" resonator resonant at the same frequency as the bar, thus making a two-mode system of coupled oscillators (referred to as the "antenna") [4, 20]. The mass of the resonator is small enough so that the effects of a passing gravity wave on it are ignored. Facing the mushroom resonator but attached firmly to the bar is a superconducting pick-up coil with a persistent supercurrent. The distance between the coil and the resonator is therefore proportional to the distance between the bar and resonator. Oscillations of the mushroom resonator change the inductance of the pick-up coil, modulating the flux through it. A dc SQUID[2] converts the changing flux to a voltage.

2.1.3 The Calibrator

An off-resonant capacitive transducer, the calibrator, is attached to the bar at the opposite end from the inductive transducer. Voltages applied to the capacitor applied forces to the antenna, which we used for a number of tasks. The calibrator was used to actively dampen the mode Q's to shorten the recovery time after large excitations and to cancel positive feedback on the antenna produced by the SQUID [20]. Under normal operating conditions the calibrator was used to excite the antenna at a frequency of 865.00 Hz, far removed from either of the modes. This "continuous systems test" provides a powerful tool for checking on the health of the detector. The calibrator was also used to provide burst signals to the antenna allowing the detector to be calibrated and allowing a study of the effects of noise on signal detection to be made.

[2]Biomagnetic Technologies, inc. 4174 Sorrento Valley Blvd. San Diego, CA 92121

2.1.4 The Antenna Model

The Allegro detector model is illustrated schematically in Fig. 2.2. where we include all of the relevant stationary noise sources. The equations of motion for this model are:

$$M_1\ddot{x}_1(t) + H_1\dot{x}_1(t) + K_1x_1(t) - H_2\dot{x}_2(t) - K_2x_2(t) = F_1(t) - F_2(t) + F_T(t) + \frac{1}{2}M_1L_1\ddot{h}_{xx}(t) \quad (2.1)$$

$$M_2(\ddot{x}_2(t) + \ddot{x}_1(t)) + H_2\dot{x}_2(t) + K_2x_2(t) = F_2(t) - F_T(t) \quad (2.2)$$

$M_{1,2}$ are the effective masses of the bar and mushroom resonator. L_1 is the effective length of the bar. $K_{1,2}$ represent the spring constants of the bar and mushroom resonator. $H_{1,2}$ their respective damping coefficients. $F_{1,2}$ are the Langevin force noise generators associated with the dissipation coefficients of each mass and F_T is the noise generated by a changing magnetic pressure from the superconducting pick-up coil on the small mass resonator. x_1 is the amplitude of the first longitudinal normal mode of the bar, while x_2 is the relative displacement between the bar and the second resonator. The last term on the right hand side of Eq. (2.1) is the component of the gravitational wave tidal force along the bar axis. The model shown does not explicitly include the superconducting circuitry or the SQUID. The voltage out of the SQUID is proportional to the relative displacement of the two masses:

$$V_{out}(t) = Gx_2(t) + \eta(t) \quad (2.3)$$

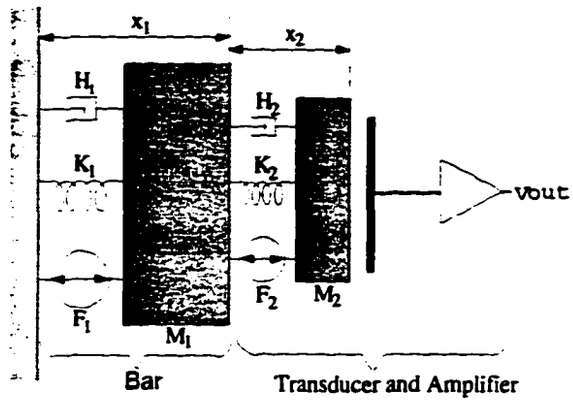

Figure 2.2: A model of the Allegro antenna.

where G is a gain factor and $\eta(t)$ is white noise from the SQUID. The time response of the antenna to a large burst signal provided by the calibrator is shown in Fig. 2.3. The power spectrum of the stationary noise out of the SQUID is shown in Fig. 2.4(a). The two resonant modes, seen clearly in the figure, are at 896.8 Hz and 920.3 Hz. We refer to them as the minus and plus modes respectively. Figure 2.4(b) shows the antenna response to a large burst signal and (c) shows the ratio of the noise to signal which is the stationary noise treated as if it were due to a random flux of gravity waves exciting the bar.

2.2 Data Acquisition

2.2.1 Signal Demodulation

The voltage from the SQUID electronics is sent to a single lockin detector which demodulates and low pass filters the signal. The reference frequency of the lockin is set halfway between the normal mode frequencies of the antenna, thus shifting the frequency of the signal from the normal modes of the antenna to low frequency.

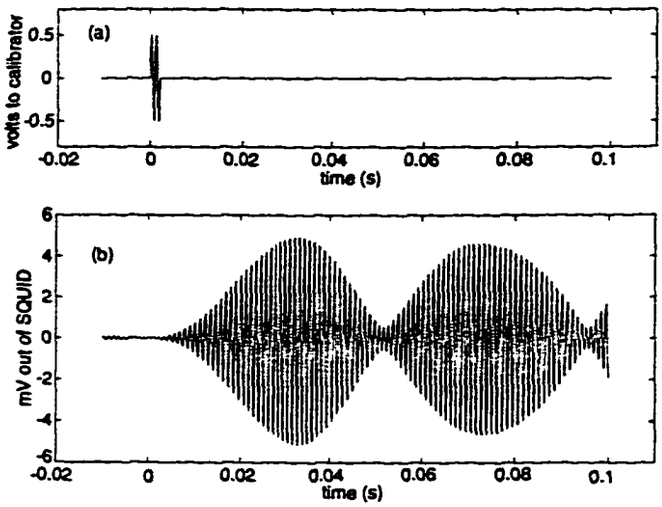

Figure 2.3: Antenna response to a burst signal. (a) The voltage provided to the calibrator. (b) The voltage response out of the SQUID in the time domain.

Because the lockin is set for a wide bandwidth, the frequency response of the detector over its entire bandwidth is monitored, enabling us to measure both the amplitude and phase of each of the resonant normal modes. It is due to the wide bandwidth that the continuous systems test can be applied to the antenna at a frequency far enough removed from the resonant modes as to not interfere with them. Other data collected to help monitor the detector includes a direct low frequency signal from the SQUID, the status of the hardware and SQUID vetos and signals from two seismometers, one of which is located on the floor next to the dewar containing the antenna, the other on top of the vibration isolation table. A schematic of the data acquisition system in shown in Fig. 2.5. The lockin is an EG&G PAR 5210 two phase lockin amplifier with reference frequency set at 908.5220 Hz, although this changes if the mode frequencies shift by a couple of mHz. The reference signal is provided to the lockin by a Hewlett Packard 3325A

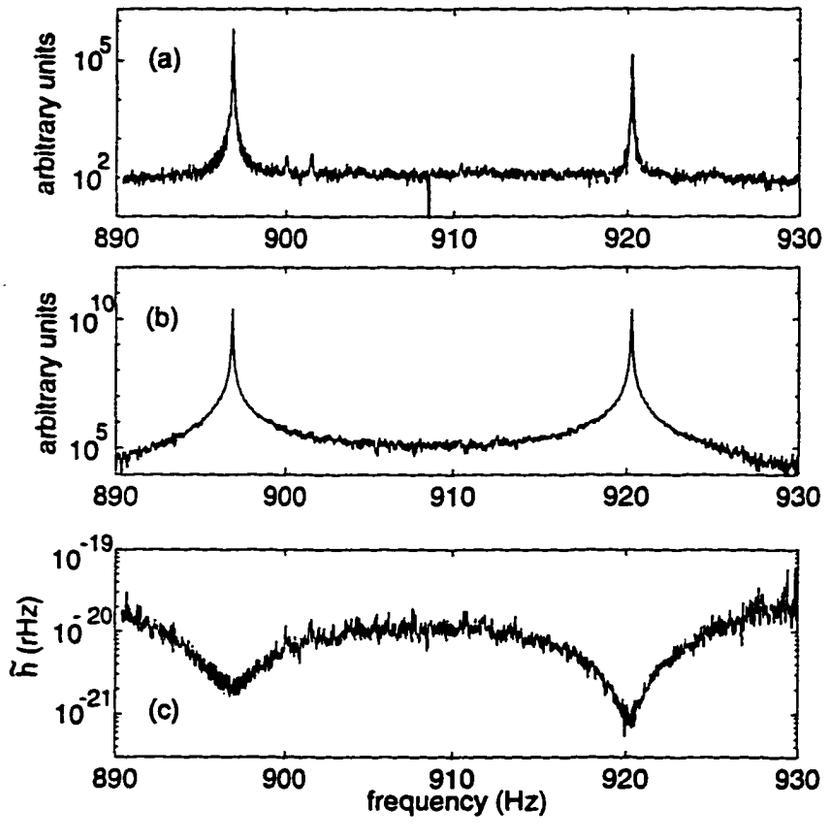

Figure 2.4: (a) The power spectrum of the voltage out of the SQUID due to stationary noise sources acting on the antenna. (b) The power spectrum after the bar has been excited by a large burst signal. (c) The square root of the ratio of (a) and (b), showing the stationary noise as if it were all due to a random flux of gravity waves exciting the bar. Also included in (c) is the predicted strain noise from the full Allegro model (dashed line).

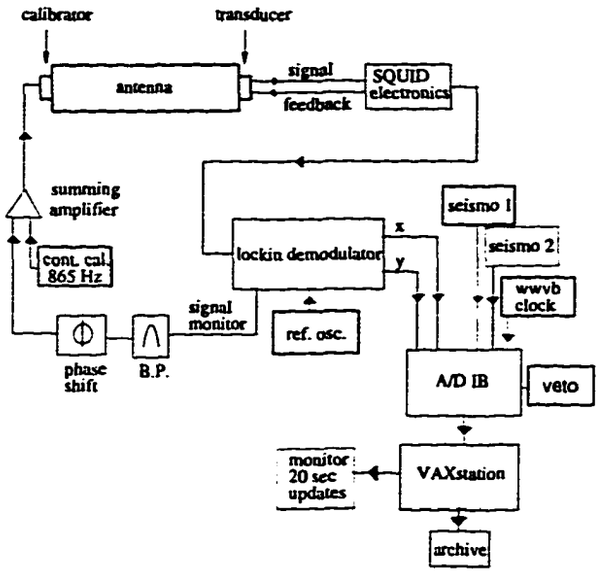

Figure 2.5: Schematic of the Allegro data acquisition system.

function generator equipped with a high stability oscillator. After the lockin, the in-phase and quadrature output voltages are sent through an anti-aliasing filter (cutoff frequency 40 Hz) and then to the A/D Interface Box (A/D IB).

2.2.2 Data Collection

The A/D IB was constructed by the LSU Physics electronics shop and the Gravity Wave Group. It controls the sampling rate of the data, converts the analog signals to digital data streams and sends the data to a VAXstation 3500. An important factor to note is that before any data was collected by the A/D IB rigorous testing was performed on it. A sine wave of amplitude large enough to span the entire range of the A/D converters was input to each A/D and the output inspected to verify: (1) that the A/D converters responded properly, (2) that the time between samples remained constant and that no samples were missed, (3) that the data written to

disk was consistent with the input signal. It was not until the data acquisition system ran for about a week without any problems that it was considered stable enough to collect data.

A Kinemetrics model 60-DC clock provides a 1kHz square wave phase-locked to coordinated universal time (UTC) which the A/D IB uses as a counter. UTC is provided by the National Institute of Standards and Technology (NIST) in Boulder, Colorado over radio station WWVB, transmitting at 60 kHz. When the counter reaches 8 ms the data is sampled and sent to disk, resulting in a sampling time of 8 ms. Data sampled includes: (1) The in-phase and quadrature output channels of the lockin (referred to as x and y respectively), (2) a direct low frequency signal from the SQUID, (3) the signal from the two seismometers, (4) the status of the hardware and SQUID vetos and (5) the sample time in UTC. The voltages out of the lockin are sampled with 16-bit accuracy, the others 12-bit accuracy. This data is referred to as the raw data to denote it has not been subject to any software fiddling. Table 2.1 shows the format of the raw data in a record. Twenty seconds worth of data (2500 samples) is assembled by software into a data block and written to disk. There are 4320 blocks in a full day's worth of data. A DEC 3000 AXP, clustered to the VAXstation 3500, is used for on-line monitoring of the detector and analysis of the data. A week's worth of data (about 875 Mbytes) is allowed to accumulate on disk and is then archived to 4mm DAT tape. Two tapes are made using VMS BACKUP to insure the data is transferred accurately and one tape is made using VMS COPY which allows easy access to the data. One BACKUP tape and the COPY tape are stored in the lab, while the other BACKUP tape is stored off campus.

Table 2.1: Format of raw data record

once a record	
40 bytes	Header
2500 samples in a record of each of the following:	
2 bytes	lockin output x
2 bytes	lockin output y
2 bytes	2 seismometer outputs (12 bit resolution each)
2 bytes	4 veto bits and 12 bits low frequency SQUID output
2 bytes	universal time (unit seconds + milliseconds)(BCD encoded)
in the header	
2 bytes	UT day number
1 byte	File identifier (A...Z)
1 byte	block type
2 bytes	record number in file (1...4320)
2 bytes	run number
8 bytes	VMS time of the first sample in the block
6 bytes	spare
4 bytes	university id
2 bytes	universal time of the first sample in the block
2 bytes	UT word 1
2 bytes	UT word 0
2 bytes	gain code
2 bytes	sampling time
2 bytes	number of samples in a block
2 bytes	number of lockins

2.3 Data Analysis

The data analysis programs read a block of data directly off of the disk. Since the data is written to disk every twenty seconds, it is available twenty seconds or less after being collected. In this way problems with the detector or with the electronics can be identified and corrected quickly. This "on-line" monitoring capability does not affect the taking of data since it is a separate program running at a much lower priority than the collection routine.

A single program, written in the language MATLAB[3], does the majority of the data analysis. The analysis begins by reading in a block of data, removing DC offsets from the in-phase and quadrature signal components and correcting for lockin gain. The program implements two digital lockins which mix x and y with reference frequencies set at the plus and minus resonant frequencies. The outputs of these digital lockins are the in-phase and quadrature components of the amplitude of each mode, written as x_+, x_-, y_+, y_- where + refers to the plus mode and − the minus. The in-phase and quadrature components of each mode are then separately filtered with an 8^{th} order digital Bessel anti-aliasing filter having a corner frequency of 2.35 Hz. The filtered data is then decimated to reduce the amount of data handling. We keep only every tenth sample, truncating the data to an effective sampling time of 80 ms.

The in-phase and quadrature components of each mode are optimally filtered for a burst signal (see Sec. 2.4) and the output squared and added to form the mode burst energies at each sample. Representing the output of the optimal filter

[3]The MathWorks, Inc. 24 Prime Park Way, Natick, Mass.01760

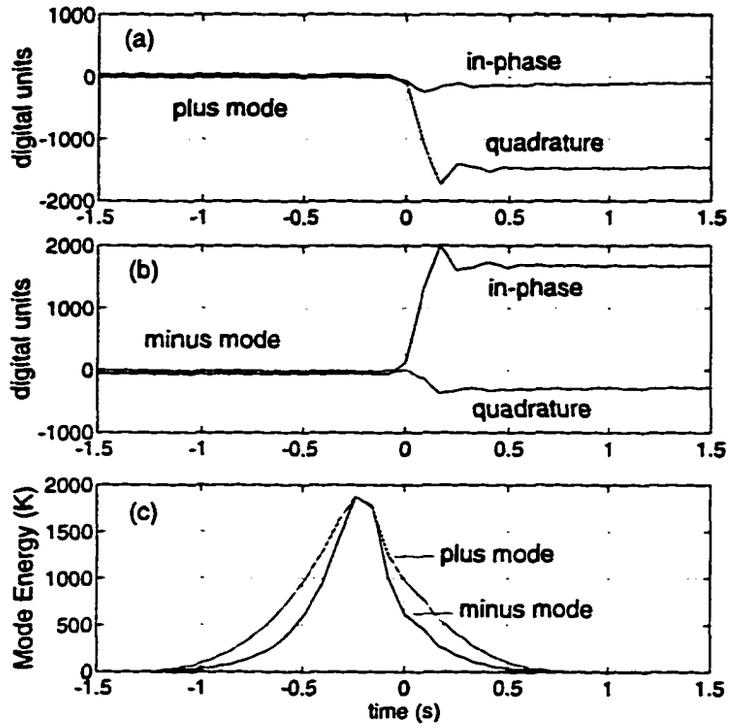

Figure 2.6: (a) The plus and (b) the minus mode amplitudes in response to the signal of Fig. 2.3. (c) The optimally filtered response to the same signal. The offset from zero seconds in (c) is due to a miscalculation of the timing delays introduced by the filtering.

by f_{x+}, f_{y+}, f_{x-} and f_{y-}, the estimate of the burst energy at each sample is

$$E_{\pm} = f_{x\pm}^2 + f_{y\pm}^2. \tag{2.4}$$

The mode response to a large burst both before and after optimal filtering is shown in Fig. 2.6. It has become conventional in this field to express energy in Kelvin. Therefore, a "mode noise temperature" is defined as the mean value of the mode burst energy $T_{\pm} =< E_{\pm} > /k_B$. Burst energy is not to be confused with the energy

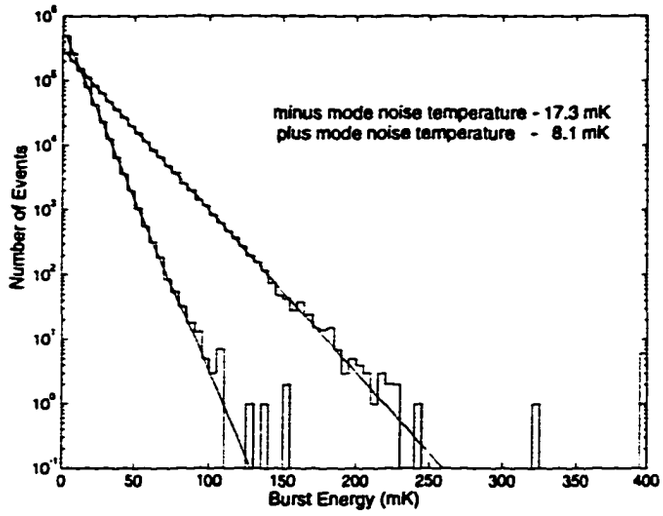

Figure 2.7: A histogram of the energy in each mode for day 200 of 1994. The slope of the histogram gives the noise temperature for each mode.

in a mode as given by the equipartition theory. Instead, it is a measure of the change in energy of the modes between samples. Since the sampling time is much less than the "random walk" time of the antenna (8 ms compared to 40 mins) the noise temperature is much less than the physical temperature of 4.2 K.

To reduce the amount of data handled, a threshold is applied so that only those samples with energy 10× the noise temperature or greater in both modes are recorded each day by the analysis programs. Each sample is tagged with the time in seconds from the start of the day. Above this threshold there are roughly 400-600 Allegro samples per day (Fig. 2.7). Also as part of the analysis the average over each record of x_+, x_-, y_+, y_-, E_+ and E_- is recorded along with the UTC time of the start of each record and the raw low frequency and seismometer data. This information is used primarily for diagnostic checks on the detector.

This is the end of the analysis unless there is to be a coincidence search with other gravity wave detectors, such as the Explorer detector of the University of Rome, or GRO gamma ray data. Before exchanging data, we first edit those excitations of the antenna that can be positively identified as something other than a gravity wave (such as an earthquake or an electronic hiccup). Next the mode noise temperatures (Fig. 2.8) are calculated in six minute averages for the entire span of the coincidence search. The statistically correct way to combine the energy information from both modes is by forming a weighted burst energy

$$E_w = T_w(E_+/T_+ + E_-/T_-) \tag{2.5}$$

where

$$T_w^{-1} = T_+^{-1} + T_-^{-1} \tag{2.6}$$

is the weighted noise temperature (this is the overall noise temperature of the detector) and T_+, T_- are the previously mentioned averages. A threshold is applied to E_w so that only samples with $E_w > 11.5T_w$ are kept. The factor of 11.5 was chosen so that the Allegro event rate for the 1991 coincidence search with the Explorer detector would be about 100 events/day. The consistency of the Allegro detector is demonstrated by the fact that the same threshold produced about 100 events/day for the entire 3 1/2 years of continuous operation. Consecutive samples above threshold are then collapsed into a single time and energy, creating an event. The energy assigned to the event is the energy of the sample in the series of consecutive samples above threshold with the maximum energy value.

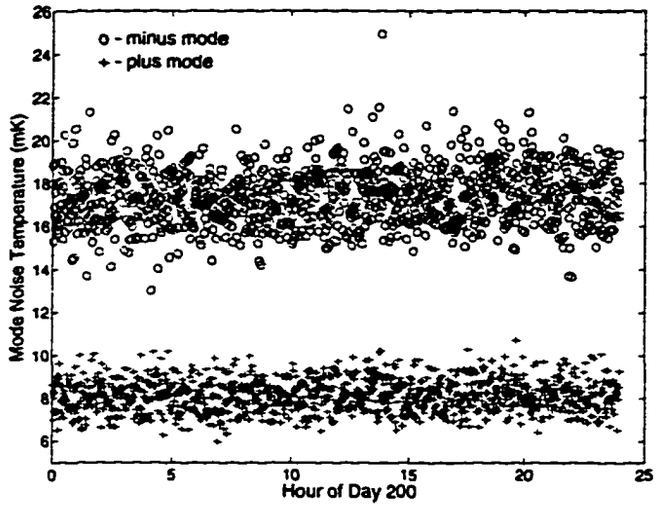

Figure 2.8: The average noise temperature in each mode during day 200 of 1994. Each data point represents a six minute average of the mode burst energies.

The time of the event is given by the time of the first sample in the series plus half the duration of the series, where the duration is defined to be the time of the last sample minus the time of the first sample. The sample time is determined by reading the UTC time at the beginning of the record containing the event and then counting the number of samples (at 80 ms between samples) into the record to that event. Then an offset is subtracted from the resulting time to account for filtering delays. Figure 2.9 shows the final event list for a small section of data.

2.4 The Filtering Algorithm

The optimal filtering on Allegro is done in the time domain so that it can be applied directly to the incoming data. We use the MATLAB *filter* routine which applies the optimal filter to the data using the transposed direct form II structure [21, p.155]. The filter coefficients which will maximize the signal to noise ratio for a

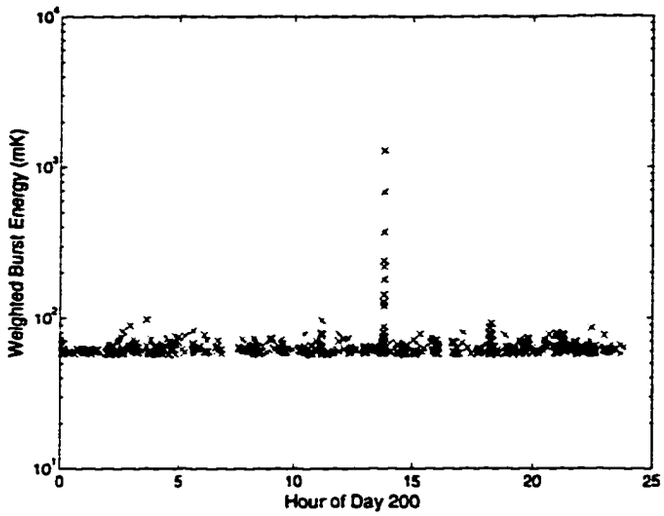

Figure 2.9: The final event list for day 200 of 1994.

sequence of data involving stationary noise are given by [22, pages 184–184], [23, pages 126–135]

$$\underline{a} = \underline{\underline{R}}^{-1}\underline{s} \tag{2.7}$$

where $\underline{a}$ is the vector containing the filter weights, $\underline{\underline{R}}^{-1}$ is the inverse of the auto-correlation matrix of the noise and $\underline{s}$ is the detector's response to the signal being looked for. In the following analysis of the optimal filter we will use a single underline to denote a vector and two underlines for a matrix. Because the in-phase and quadrature components for each mode are statistically similar, they can be averaged to make a single correlation function for the noise in each mode. Also, the in-phase and quadrature components of the signal vector are combined (described later) to form the mode response to a burst. The correlation functions of the two modes are not similar and therefore a pair of filter weights are created, one to filter

the plus mode and the other to filter the minus mode. The details of creating the autocorrelation matrix and the response vector (signal) are described next.

2.4.1 The Signal

The signal vector $\underline{s}$ is obtained by applying a very large calibration pulse to the antenna so that the low pass filtered and decimated output is essentially unaffected by the stationary noise. Next, the mean value of the first few samples is subtracted from each sample in the signal array so that the amplitude just before the pulse hits the antenna is near zero. Then, the squares of the in-phase and quadrature signal components in each mode are added and the square root taken to create the final form of the signal vector (Fig. 2.10)

$$\underline{s_{\pm}} = \sqrt{\left(\underline{s_{\pm}^{x}}\right)^2 + \left(\underline{s_{\pm}^{y}}\right)^2}. \tag{2.8}$$

2.4.2 The Noise

The first step in forming the autocorrelation matrix for the noise is to form the autocorrelation function for one record's worth of low pass filtered and decimated data

$$\underline{R} = \frac{1}{N}\sum_{i=0}^{N-1} n_i n_{i+j} \tag{2.9}$$

with N the number of coefficients in the filter, i the sample index and j the time offset index. This is done every twentieth record for an entire day's worth of data. It is necessary to use such a long time span of data because of the long relaxation times of the normal modes. All events outside the thermal distribution are removed from the data before forming the correlation function as the presence of non-stationary noise will degrade the filter's performance. The length of the

filter, N, was determined experimentally. Filter lengths of 20 to 50 decimated samples were tried and it was found that the noise temperature of the modes decreased up to 40 coefficients (amounting to 3.2 seconds of data). After that, the noise temperature no longer decreased with increasing coefficient number so 40 decimated samples was chosen as the length for the filter.

Next, the values of $\underline{R}$ at each j from each record analyzed are summed and the in-phase and quadrature components added to form the autocorrelation function for a mode. The autocorrelation matrix is formed using the Matlab routine *toeplitz* such that the zero delay components R_{00} lie along the diagonal

$$\underline{\underline{R_{\pm}}} = toeplitz(\frac{1}{2}(\underline{R_{\pm}^{x}} + \underline{R_{\pm}^{y}})). \tag{2.10}$$

Here the in-phase and quadrature components are denoted with an x and y respectively. The inverse of the matrix is formed using the Matlab *inv* routine

$$\underline{\underline{R_{\pm}}}^{-1} = inv\left(\underline{\underline{R_{\pm}}}\right). \tag{2.11}$$

Having obtained the inverse of the autocorrelation function for the noise and the signal vector, the filter weights for both the plus and minus modes are formed by Eq. (2.7). The final form of the weights is shown in Fig. 2.11.

2.4.3 Normalization

Once the optimal filter is constructed the weights are normalized by putting a pulse of known energy into the antenna using the calibrator. A SRS Model DS345 function generator was used to provide 2 cycles of a 908 Hz sine wave of constant

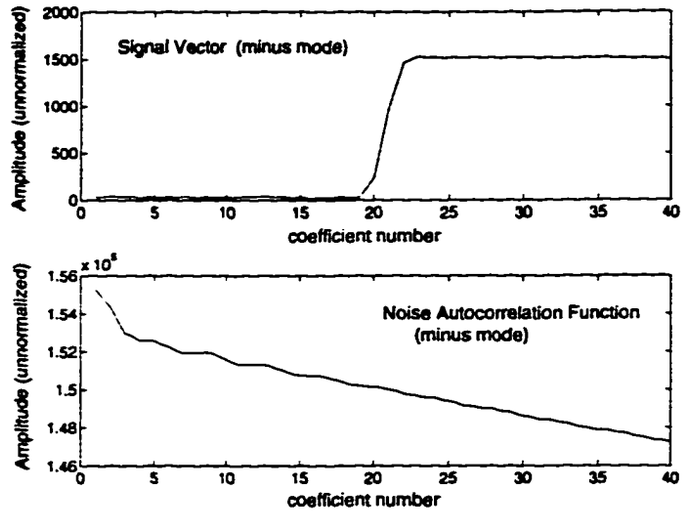

Figure 2.10: The signal vector and noise autocorrelation function used in creating the optimal filter for the minus mode.

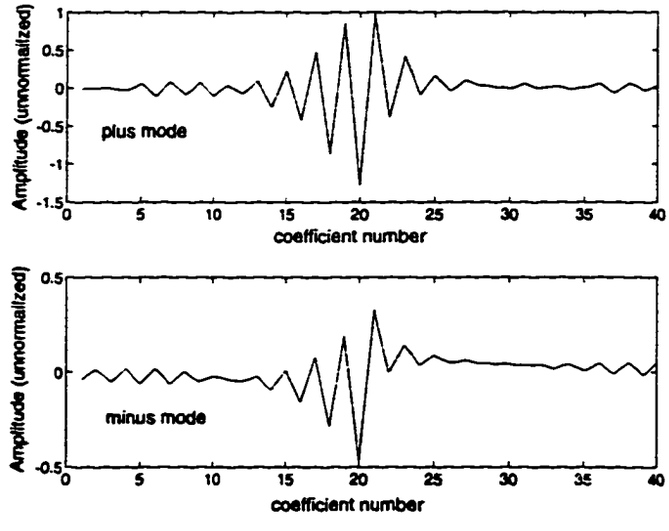

Figure 2.11: The optimal filter weights for the minus and plus modes.

amplitude to the calibrator at twenty second intervals. The energy deposited in each mode of the antenna by a single pulse is [24]

$$E_{cal\pm} = \frac{\pi}{2}\frac{\gamma_{\pm}}{\omega_{\pm}}(NV)^2 \tag{2.12}$$

where $\gamma_{\pm}$ is the calibrator coupling coefficient for each mode, defined as the ratio of the current output from the calibrator to the input driving voltage and were measured in a separate experiment. $\omega_{\pm}$ are the mode frequencies, N is the number of cycles and V is the voltage zero to peak provided to the calibrator. A weighted burst energy is formed with Eq. 2.5.

Approximately 60 pulses were applied having an amplitude large enough so that the effects of stationary noise on the estimate of the resulting burst energies was small. After applying the pulses the data was analyzed as described in Section 2.3 to produce a list of corresponding events. The mean of the mode burst energies of the pulses was compared to the expected energy deposited in the antenna as given by Eq.(2.12) and the filter weights scaled so that the two matched.

The filtering scheme causes a delay between the actual arrival time of a pulse and the recorded arrival time. This delay needs to be measured and removed from the estimate of the timing of events. A very large calibration pulse was applied to the antenna and analyzed to produce a filtered event. This event consisted of approximately 40 decimated samples similar to Fig. 2.6. The time ascribed to this event by the procedure described previously was 14581.672 seconds. Examining the raw data (after lockin and low pass filtering but before any processing by the analysis programs or decimation) it was determined that the first signs of the

calibration pulse effecting the antenna appeared at 14579.936 seconds. Subtracting the two gives a delay of 1.74 seconds, which is then removed when the event times are recorded.

2.5 Event Uncertainties

It is impossible for a single detector to differentiate between a gravity wave passing through the antenna and excitations due to noise. At low energies the thermal spectrum (stationary noise) masks any signal, while above that a signal is indistinguishable from a burst of non-stationary noise. Two or more (the more the better) detectors operating in coincidence, however, can greatly reduce the noise level by demanding that: (1) a gravity wave excite each antenna simultaneously within a few milliseconds, depending on the distance between them and (2) for similar detectors aligned with respect to astrophysical sources, such as Allegro and Explorer, the energy deposited in each be equal. Unfortunately, noise sources add a degree of uncertainty to any measurements of event arrival time and energy with the result that one looks instead for a coincidence: (1) in a window of time which is much greater than the light travel time between detectors and (2) where the energy of a signal is no longer equal in each detector, but lies in some range which we shall show depends on both the noise temperature of the detectors and the strength of the signal. In this section we quantify the uncertainties introduced into these measurements by the stationary noise.

Using the same parameters as described in Section 2.4 a series of calibration pulses was applied to the bar. A signal from the function generator was connected

Table 2.2: The anticipated energy of each calibration pulse and the number of pulses applied at that energy for a given series.

calibration series	pulse energy (mK)	number of pulses
cal2_312	64	100
cal3_312	76	100
cal4_312	110	100
cal1_317	220	100
cal2_317	420	100
cal3_317	1000	100
cal1_327	110	60
cal2_327	150	60
cal3_327	220	60

to one channel of the hardware veto so that at the same time a voltage pulse was applied to the calibrator a veto was recorded. This allowed the sample immediately following excitation of the antenna to be identified. The largest error this procedure can produce in the timing of the pulse is 8 ms which, as we shall see, is much smaller than the final uncertainties in the timing. The anticipated energy deposited by each pulse given by Eq.(2.12) and their number for each calibration series are shown in Table 2.2.

2.5.1 Uncertainties in Timing

The calibration pulses were analyzed with the procedures described in Section 2.3 to produce lists of event times and energies. Call the event time assigned to each calibration pulse the "arrival time" and identify a "pulse application time" with the tripping of the veto. Subtracting the arrival time from the application time produces a timing offset for each calibration pulse. Figure 2.12 shows the offset for each pulse in the calibration series cal1_327. The standard deviation of the offsets

is a measure of the uncertainties in our timing procedures. Figure 2.13 shows the standard deviation of the offsets from each series of pulses, in effect plotting the timing uncertainty as a function of signal strength. Of the nine data points shown, 7 are within one standard deviation of the mean uncertainty, and only the smallest signal (still about $11.5T_w$) is significantly different. What is surprising is that at the highest signal strength, about $180T_w$, the timing is no more accurate than at lower energies. The end result is that for signals above $11.5T_w$ Allegro's timing is accurate to ± 0.1 second.

2.5.2 Uncertainties in Energy

Noise sources acting on the antenna, both thermal and electronic, are stationary distributed with zero mean. This property is not changed by either the lockin or the optimal filtering. In the absence of a signal or non-stationary noise the outputs from the optimal filter are statistically independent zero mean stationary variables with variance $\sigma_{\pm}^2$. Forming the mode energies by Eq. 2.4 results in an exponential distribution

$$p(E_{\pm}) = \frac{1}{T_{\pm}} \exp \frac{E_{\pm}}{-T_{\pm}} \tag{2.13}$$

with $E_{\pm}$ the detector response to stationary noise and $T_{\pm} \equiv 2\sigma_{\pm}^2$. This distribution has a non-zero mean given by

$$< E_{\pm} >= T_{\pm} \, . \tag{2.14}$$

! If a signal of burst energy $E_{cal\pm}$ is present, it can be shown that the mode burst energy of the signal combined with the stationary noise is non-central χ^2

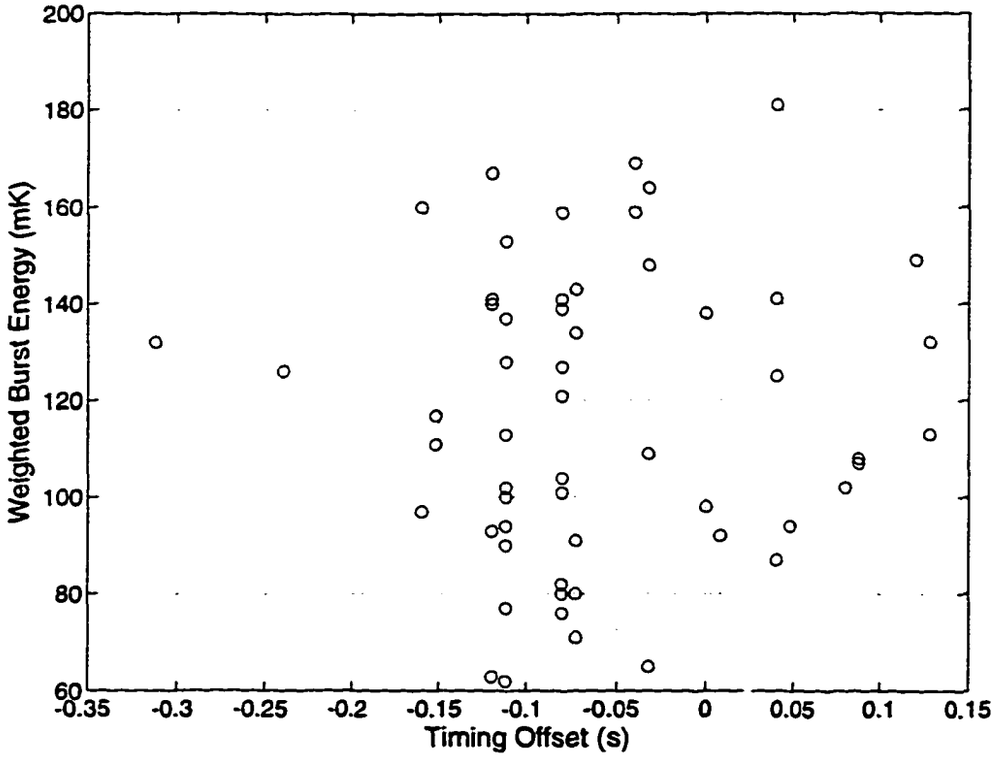

Figure 2.12: The burst energy associated with each calibration pulse in series cal1_327 and the corresponding timing offset. The shift away from zero delay is common to all calibration series having a mean value of $\leq .06$ s.

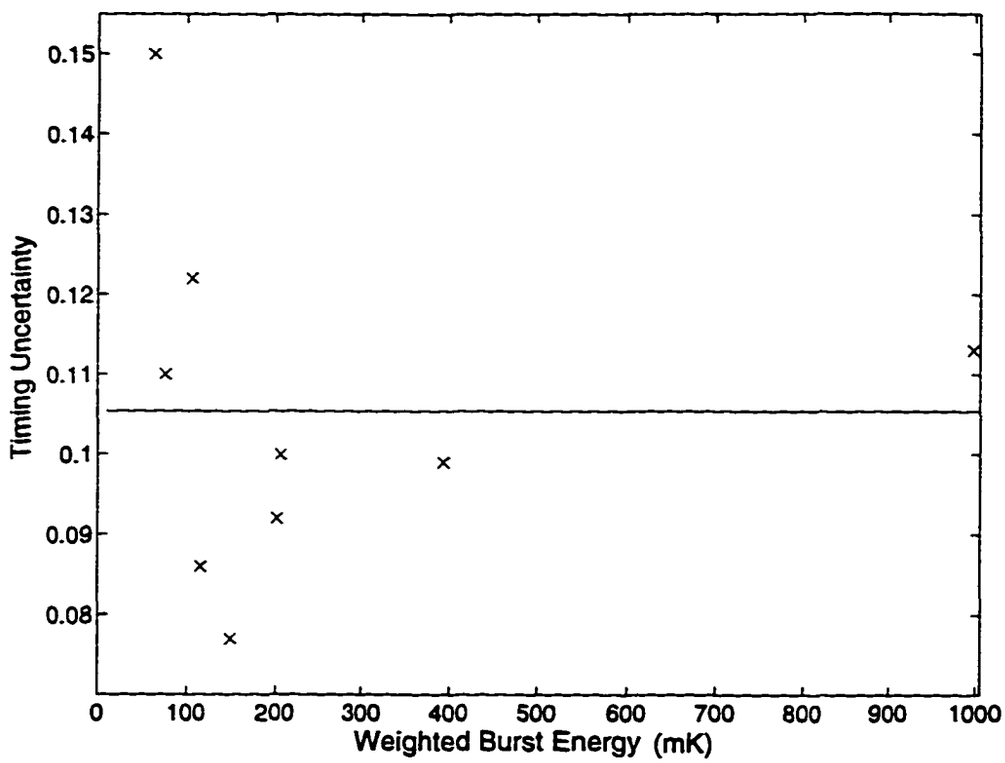

Figure 2.13: The uncertainty in the timing for each calibration series (defined as the standard deviation of the offsets) is represented by the crosses. The solid line in the mean value of the timing uncertainties. The dotted lines are one standard deviation away from the mean value of the nine data points plotted.

distributed with two degrees of freedom [23]

$$p(E_{\pm}) = \frac{1}{T_{\pm}} \exp \frac{(E_{\pm} + E_{cal\pm})}{-T_{\pm}} I_o(\frac{2\sqrt{E_{\pm}E_{cal\pm}}}{T_{\pm}}) \tag{2.15}$$

where I_o is the modified Bessel function of zeroth order. The mean and variance of this distribution are given by

$$< E_{\pm} > = E_{cal\pm} + T_{\pm} \tag{2.16}$$

$$var(E_{\pm}) = 2E_{cal\pm}T_{\pm} + T_{\pm}^2. \tag{2.17}$$

The weighted energy as defined in Eq. (2.5) is fourth order non-central χ^2 distributed [23] with non-central parameter equal to the weighted burst energy of the signal, E_{cal},

$$p(E_w) = \frac{1}{T_w} \exp \frac{(E_{cal} + E_w)}{-T_w} I_1(\frac{2\sqrt{E_w E_{cal}}}{T_w}) \sqrt{\frac{E_w}{E_{cal}}} \tag{2.18}$$

where E_w is the weighted burst energy due to the stationary noise. The mean and variance are given by

$$< E_w >= E_{cal} + 2T_w \tag{2.19}$$

$$var(E_w) = 2E_{cal}T_w + 2T_w^2 . \tag{2.20}$$

Both the distribution for the mode burst energy and the weighted burst energy are described by only two parameters, the size of the signal and the noise temperature of the detector. That the actual data from the detector follows these distributions is shown in Fig. 2.14 and Fig 2.15. Equation (2.20) is the important result with

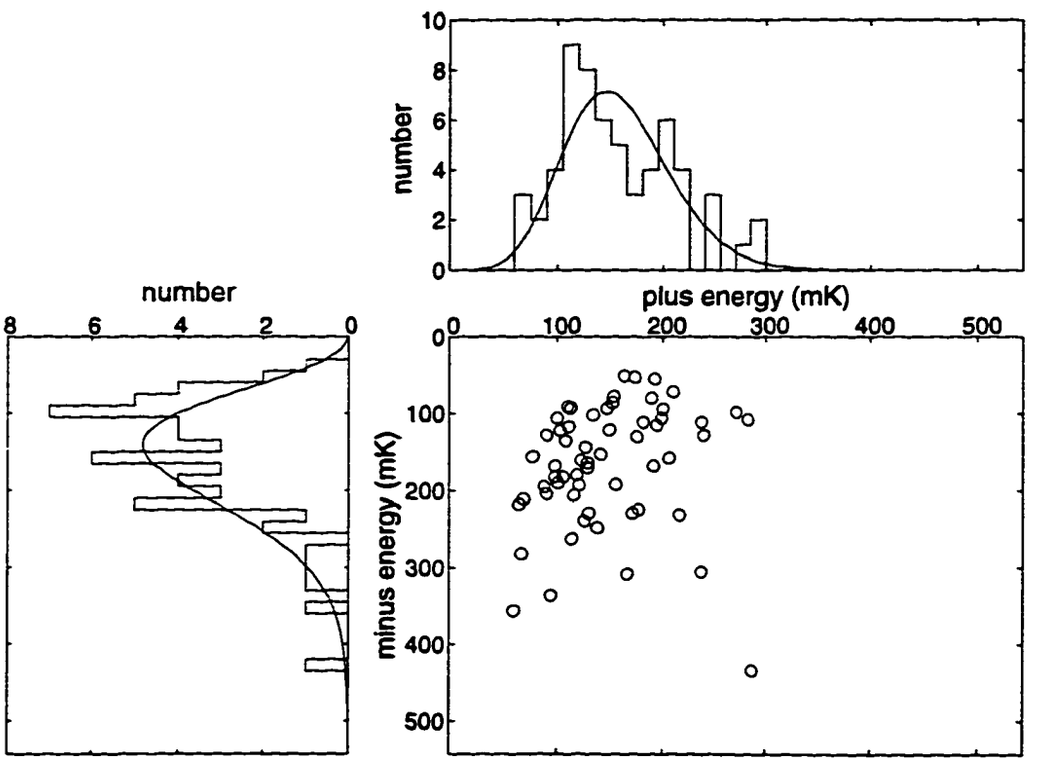

Figure 2.14: The estimate of the energy deposited in the plus mode plotted against that in the minus mode for each pulse in the calibration series cal2_327 . Sharing the same axis are histograms of the mode burst energies and the distribution function of Eq. (2.15).

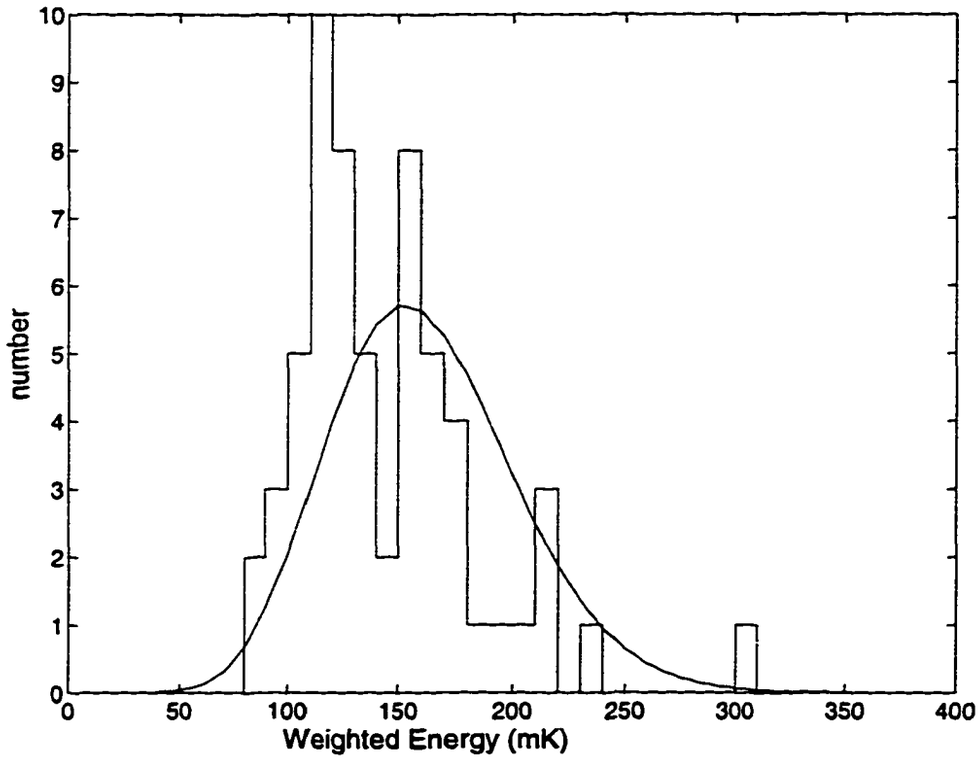

Figure 2.15: The histogram of the weighted burst energies for the calibration series cal2_327 and the distribution function of Eq. (2.18).

regards to a coincidence search. If we identify the spread in energy due to the interaction with the noise as the square root of Eq.(2.20), call it σ_w, then for a given noise temperature the spread increases as the square root of the signal strength. Figure 2.16 demonstrates that the data from Allegro matches the theory well. This curve is used to define the window of a coincidence in energy. Although the spread increases with increasing signal strength, the fractional change in energy, defined as σ_w/E_{cal} decreases as $1/\sqrt{E_{cal}}$ as is shown in Fig. 2.17.

2.6 Non-Stationary Noise

The previous section dealt with the effects of stationary noise on the accuracy of the event parameters time and energy. There is another class of noise, non-stationary noise, which effects the running of the detector as an observatory. Figure 2.18 shows the Allegro energy spectrum from 1991, 1993 and 1994. Each spectrum is divisible in two parts, the low energy stationary noise and the background events which could be from any number of mechanisms related to the detector or surroundings, or could be from gravity waves. The lowering of the background from 1991 to 1993 is attributed to two causes. First, the antenna was warmed to 15 K at the beginning of 1993 which may have reduced trapped flux in the superconductors or released some built up mechanical stress. Second, there were a number of background sources identified after 1991: millisecond electrical transients, earthquakes from around the globe, and buses hitting a pothole outside the Physics Building. Examining the raw data associated with each event outside of the thermal distribution allowed events produced by these sources to be easily recognized and vetoed with only a slight increase in the detector dead time.

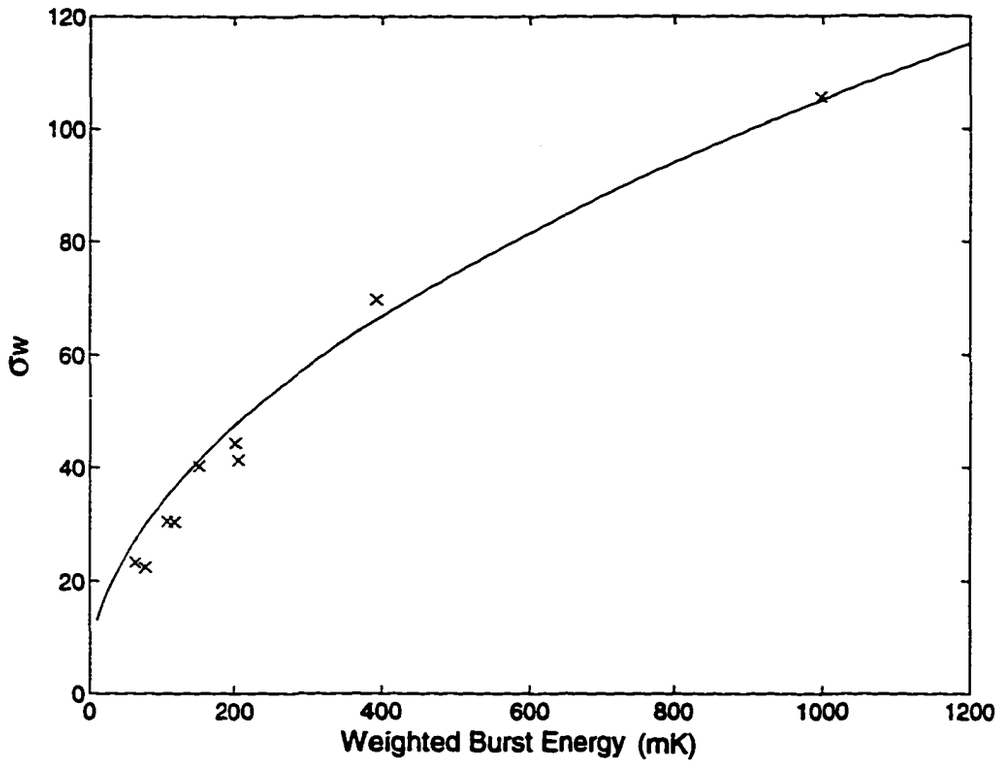

Figure 2.16: The spread in the burst energy of a signal due to stationary noise. Each data point is the standard deviation of the energy estimates for a calibration series. The solid line is a theoretical curve generated from the square root of Eq. (2.20) with a noise temperature of 5.5 mK.

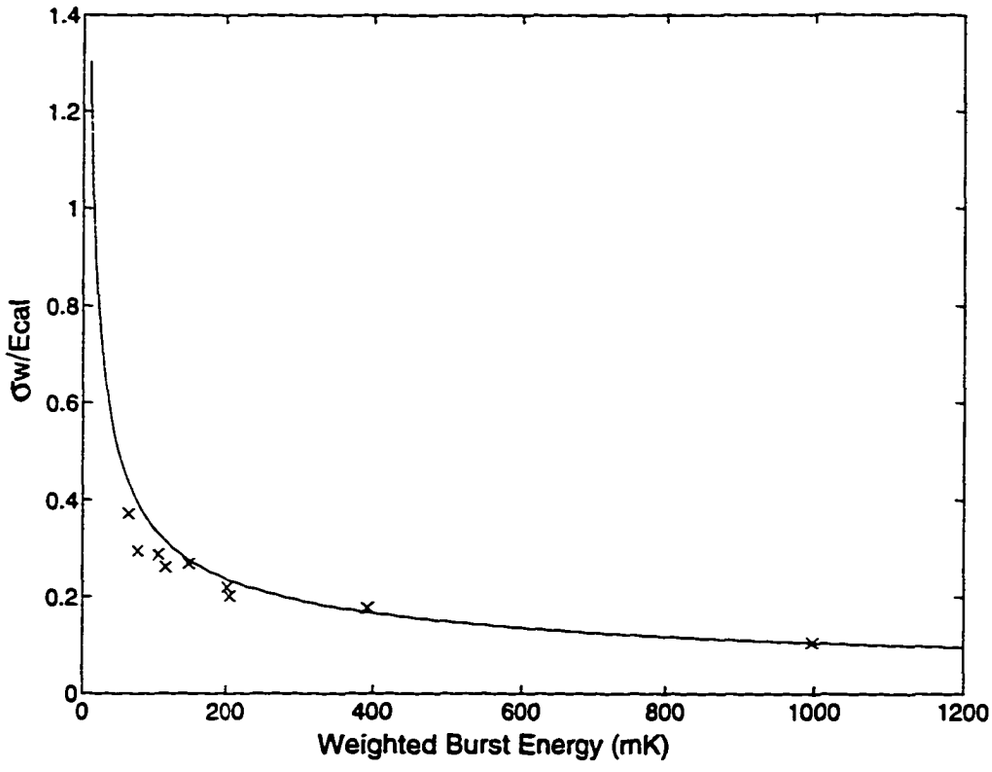

Figure 2.17: The fractional spread in burst energy of a signal mixed with stationary noise. This is simply the results of Fig. 2.16 divided by the mean value of the burst energy.

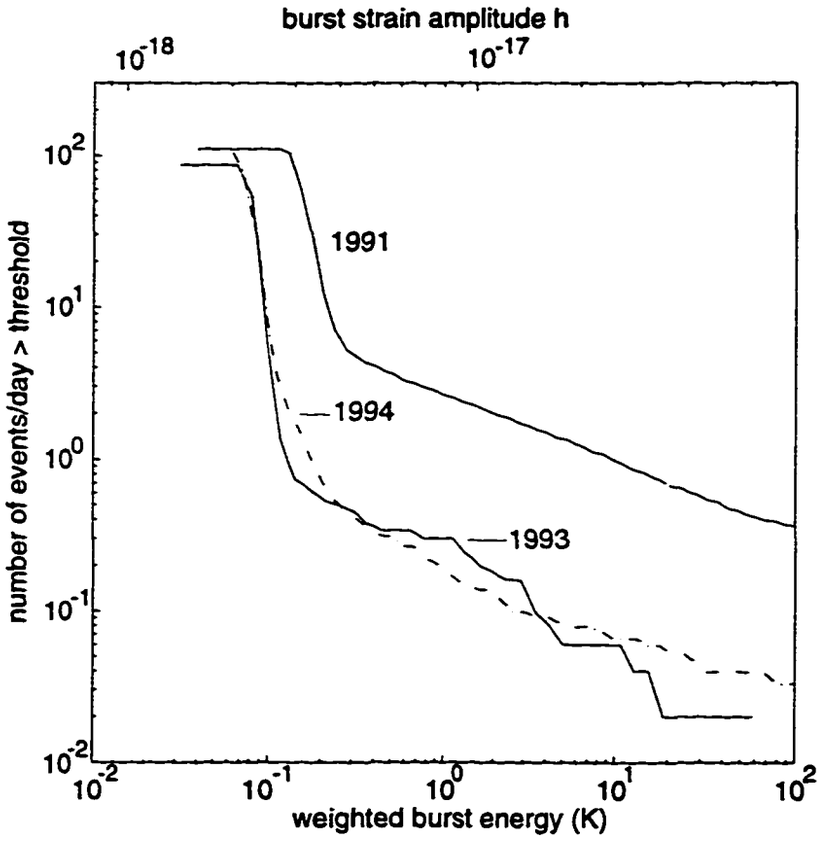

Figure 2.18: Allegro energy spectrum for 1991, 1993 and 1994. The bottom scale gives the signal threshold in Kelvin, the top scale gives the signal threshold in terms of the burst strain amplitude of a gravity wave incident with optimum polarization and direction.

Chapter 3

Continuous Wave Detection

The previous chapter dealt with the techniques used to detect burst signals of gravitational radiation. In this chapter we examine a fundamentally different problem: the detection of a continuous gravitational wave signal (CW) which persists throughout the operational time of the detector. The most likely candidate to produce such a signal is an rotating, non-axisymmetric neutron star. We will refer to this object as a "pulsar" in the following text, even though it may not be emitting detectable electromagnetic radiation.

The Allegro detector is sensitive to gravitational radiation at frequencies near 1 kHz, so only pulsars with spin periods near 2 milliseconds are expected to emit gravitational radiation detectable by Allegro. There are only a small number of known pulsars with spin-periods this low and none of those listed in the 1995 Taylor pulsar catalog [26] qualify as potential sources for Allegro.

With no "assured" source available, we would like to search the entire sky for evidence of a continuous wave signal. This is infeasible computationally. The

search we have performed involved roughly one and a half hours of computational time on a DEC 3000 AXP to fully analyze a single 28 hour record of data for a patch of sky a few arc minutes on a side. To make the most sensitive search possible, the frequency shifting of an arriving signal due to the Earth's motion and the changing antenna sensitivity to the signal must both be accounted for in the analysis. To cover the full sky by analyzing one small patch at a time is clearly unworkable.

Therefore, we directed the search for continuous wave (CW) radiation towards the globular cluster 47 Tucanae (Tuc). In 1991 10 millisecond pulsars were discovered in 47 Tuc using the Parkes radio-telescope [25]. This find doubled the number of millisecond pulsars known at that time and hence was a remarkable number of millisecond pulsars to be located in the same region of the sky. Roughly half of the pulsars found were in binary systems and all had spin periods of less than 6 ms. The close proximity of 47 Tuc (4.5 kpc) to the Earth and the possibility of undetected pulsars there (emitting electromagnetic radiation or not) made it an attractive patch of sky towards which we directed the search.

In section 3.1 of this chapter we describe the target source of gravitational radiation and the expected signal from that source. Section 3.2 describes the interaction of the gravity wave with the Allegro detector. The third section describes the analysis used to look for the anticipated signal in the Allegro data. Finally, the results of the analysis are presented and discussed.

3.1 Target Source

Suppose there is a rotating, non-axisymmetric neutron star with rotational velocity ω_{rot} and non-zero ellipticity ($\epsilon > 0$). The strain amplitude of the emitted gravitational radiation as recorded by an observer located a distance r from the pulsar, at a time t, is calculable from the quadrupole approximation:

$$h_{jk}(t, r) = \frac{2G}{c^4 r}\mathcal{I}_{jk.00}(t') \tag{3.1}$$

where c is the speed of light, G the gravitational constant, and $\mathcal{I}$ is the reduced quadrupole moment of the pulsar. $t' = t - r/c$ is the retarded time between emission of the gravity wave at the source and its arrival at the detector. Here and in the following discussion $A_{jk.00} = \ddot{A}_{jk} = d^2A_{jk}/dt^2$ and latin indicies (j,k,l...) range from 1 to 3. It is convenient to describe the gravitational radiation in a reference frame centered at the pulsar's center of mass with the $\hat{\mathbf{e}}_{z''}$ axis directed along the pulsar's angular momentum vector, but fixed relative to the rotating pulsar. This frame is referred to as the "source frame" and has coordinates (x'', y'', z''). In the source frame the moment of inertial tensor of the pulsar is

$$I'' = \frac{1}{2}\begin{bmatrix} I_1 + I_2 + (I_1 - I_2)\cos 2\omega_{rot}t & -(I_1 - I_2)\sin 2\omega_{rot}t & 0 \\ -(I_1 - I_2)\sin 2\omega_{rot}t & I_1 + I_2 - (I_1 - I_2)\cos 2\omega_{rot}t & 0 \\ 0 & 0 & I_3 \end{bmatrix} \tag{3.2}$$

where I_1, I_2 and I_3 are the principle moments of inertia about the three principle axes fixed in the body frame. For a non-axisymmetric pulsar $I_1 \neq I_2$ and we define

the ellipticity as $\epsilon = (I_1 - I_2)/I_3$. Using Eq. 3.1 to calculate the strain tensor at a distance r from the source along the pulsar's spin axis, we arrive at

$$h(t, r\hat{\mathbf{e}}_{z''}) = \frac{4G}{c^4 r}\epsilon I_3 \omega_{rot}^2 \begin{bmatrix} -\cos 2\omega_{rot}(t - r/c) & \sin 2\omega_{rot}(t - r/c) & 0 \\ \sin 2\omega_{rot}(t - r/c) & \cos 2\omega_{rot}(t - r/c) & 0 \\ 0 & 0 & 0 \end{bmatrix} \tag{3.3}$$

where it is clear that the radiation is emitted at twice the rotation frequency of the pulsar, $\omega_s = 2\omega_{rot}$. There is no reason to expect that the spin axis of the pulsar is along the line of sight to the Earth, so a new coordinate frame with coordinates (x', y', z') is defined, referred to as the "wave frame". This frame also has its origin at the pulsar's center of mass, but is rotated relative to the source frame by an angle γ so that the line of sight from the pulsar to the Earth lies along the $\hat{\mathbf{e}}_{z'}$ axis. Without loss of generality we have chosen the $\hat{\mathbf{e}}_{z'}$ direction to lie in the $(\hat{\mathbf{e}}_{z''}, \hat{\mathbf{e}}_{y''})$ plane. The relative orientation of the source frame to the wave frame is shown in Fig. 3.1.

A simple rotation of the source frame around the $\hat{\mathbf{e}}_{x''}$ axis by γ produces the form of the strain tensor as it appears at the Earth. Once in the wave frame, we express the strain amplitude in the transverse-traceless (TT) gauge. In this gauge, the only non-zero components of the strain tensor are those perpendicular to the direction of propagation. Transformation to the TT gauge is performed using the projection operator which "projects" the gravitational strain tensor onto the plane perpendicular to the direction of propagation. Components of the projection operator are defined as

$$P_{jk} = \delta_{jk} - n_j n_k$$

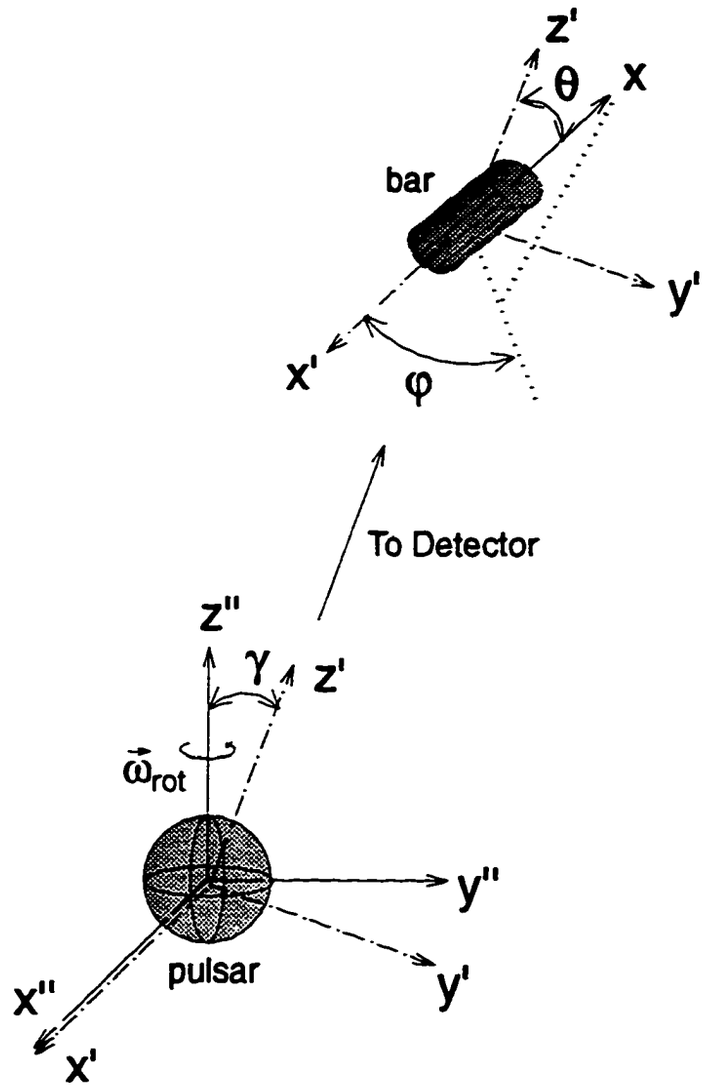

Figure 3.1: The relative orientations of the source frame ($\vec{x''}$), to the wave frame ($\vec{x'}$). Also included is the orientation of the wave frame to the bar frame ($\vec{x}$). The (z'', y'') plane is parallel to the plane of the page.

where n_k is the unit vector in the direction of propagation. For propagation along $\hat{\mathbf{e}}_{z'}$. the only non-zero components of P are $P_{11} = P_{22} = 1$. Calculation of the strain tensor in the TT gauge is from the strain in an arbitrary gauge is given by [28]

$$h_{jk}^{TT} = P_{jl}\, P_{mk}\, h_{lm} - \frac{1}{2} P_{jk}(P_{ml} h_{lm}). \tag{3.4}$$

where the first term on the right hand side of Eq. 3.4 is the transverse part of the strain tensor which then has its trace. given by the second term. subtracted from it.

Using Eq. 3.3 and Eq. 3.4. the transverse-traceless gravitational wave that reaches Allegro (assuming a distance r from the pulsar to the detector) is

$$h^{TT}(t. r\hat{\mathbf{e}}_{z'}) = h_c \begin{bmatrix} -(1+\cos^2\gamma)\,\cos\omega_s t' & (2\cos\gamma)\,\sin\omega_s t' & 0 \\ (2\cos\gamma)\,\sin\omega_s t' & (1+\cos^2\gamma)\,\cos\omega_s t' & 0 \\ 0 & 0 & 0 \end{bmatrix} \tag{3.5}$$

where

$$h_c = \frac{2G}{c^4 r} \epsilon I_3\, \omega_{rot}^2 \tag{3.6}$$

is the "characteristic" strain amplitude of the incident wave [29]. It is conventional to define the "plus" and "cross" polarization states of the gravity wave in the TT gauge as

$$h_+(t) = h_c(1+\cos^2\gamma)\,\cos(\omega_s t) \tag{3.7}$$

and

$$h_\times(t) = h_c(2\cos\gamma)\,\sin(\omega_s t) \tag{3.8}$$

respectively. Notice that when the gravity wave is observed along the spin axis of the pulsar, it is circularly polarized. When it is observed away from the spin axis the gravity wave is elliptically polarized. That the amplitude of the plus polarization is always greater than zero expresses the fact that since the pulsar has a time-dependent quadrupole moment, there will always be gravitational radiation emitted regardless of the orientation of the pulsar to the observer.

3.1.1 Anticipated Signal Amplitude

We used h_c to estimate the amplitude of the CW signal from 47 Tuc. Substituting $\omega_{rot} \sim 2\pi \times 500$ Hz, $r = 4.5$ kpc and $I_3 = 10^{45}$ g cm^2 into Eq. 3.6, the characteristic amplitude is

$$h_c \sim 10^{-20}\epsilon \tag{3.9}$$

where the value given for I_3 is a standard estimate for the moment of inertia of a neutron star [30]. The amplitude of the strain is proportional to the degree of asymmetry in the pulsar. We estimate an upper limit for ϵ by assuming the observed pulsar spin-down rate ($\dot{P}$) for a millisecond pulsar is due entirely to the emission of gravity waves. For pulsars with larger magnetic fields, usually involving slower rotation rates than considered here, the observed spindowns are accounted for by magnetic braking and not the emission of gravitational radiation. The weak magnetic fields of millisecond pulsars result in spin-down values roughly 5 orders of magnitude smaller than those measured for normal pulsars. The rate of emission

of gravitational energy from a pulsar is given by [30]

$$\dot{E}_{gr} = -\frac{32G}{5c^5} I_3^2 \epsilon^2 \omega^6 \tag{3.10}$$

and the spin down energy loss is given by

$$\dot{E}_{rot} = I_3 \omega \dot{\omega}. \tag{3.11}$$

Using $\dot{P} = 10^{-21}(s/s)$ as a fiducial value for the spin down of millisecond pulsars [26] and equating Eq. 3.10 to Eq. 3.11 results in

$$\epsilon \leq 10^{-9}$$

$$h_c \sim 10^{-29}.$$

A strain of this amplitude is unobservable by Allegro. However, it is conceivable that the ellipticity is much larger than this, up to a value of $\epsilon \sim 10^{-4}$ which is the expected upper limit due to the breaking strain of the pulsar's outer crust. Between these two limits the details of the pulsar interior and the pulsar's magnetic field become important in estimating the degree of asymmetry.

3.1.2 Doppler Shifting

The signal of Eq. 3.5 is complicated by the relative motion of the Earth with respect to the pulsar. This motion produces a phase-shift in the observed signal compared to the signal in the wave frame. Figure 3.2 shows the Doppler shift as

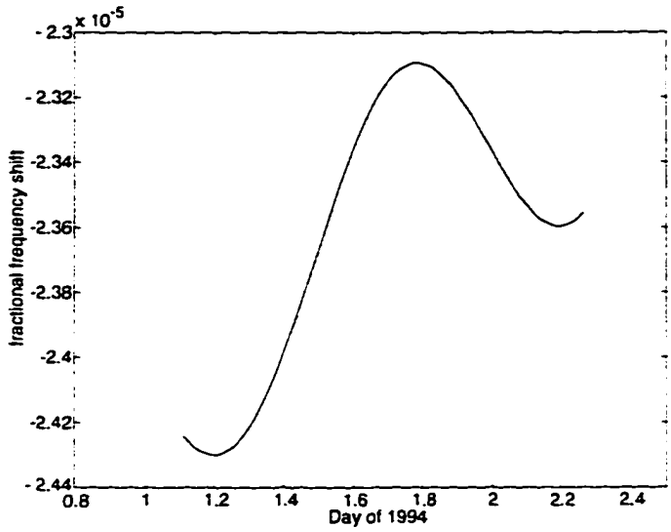

Figure 3.2: Fractional shift in frequency of a signal from 47 Tuc arriving at the Allegro detector on January 1-2, 1994. That the shift is negative reflects the fact that Allegro was moving away from the source at this time. The sinusoidal feature is due to the Earth's rotation about its axis, while the slope of the frequency shift is due to the orbital motion of the Earth around the sun.

the fractional shift in the frequency of a signal arriving at Allegro from 47 Tuc. The amount of the phase shift is calculated by noting that the acceleration of a pulsar which is not in a binary system, relative to the solar system barycenter (SSB), is small enough so that the SSB and the pulsar are in the same inertial frame. This being the case, proper time as measured in a coordinate frame centered at the SSB is essentially the same as proper time as measured in the wave frame. SSB proper time is measured in dynamical barycentric time (TDB). From this, the phase shift of the signal arriving at Allegro is directly proportional to the time difference between the gravity wave arriving at the detector and its arrival at the SSB, with the constant of proportionality equal to the signal frequency ω_s. We will use the notation $\delta(t)$ for the Doppler phase shift in the following sections.

Table 3.1: Timing offset between TDT and UTC. The stated date denotes the start of the period for which the value of the timing difference is valid.

Date	TDT - UTC (s)
1/1/91	26.000 + 32.184
7/1/92	27.000 + 32.184
7/1/93	28.000 + 32.184
7/1/94	29.000 + 32.184

Lab time was specified in coordinated universal time (UTC), which is a hybrid timing scale. It is related to international atomic time (TAI) by an integral number of seconds, but is kept to within $\pm.9$ seconds of universal time (UT), which is based on the diurnal motion of the sun. To keep UTC within a second of UT, "leap seconds" are periodically added to UTC, after the sixtieth second of the last minute of either December 31 or June 30. For astronomical purposes, reporting lab time in terrestrial dynamical time (TDT) was more convenient. TDT is simply offset from TAI by +32.184 seconds. We therefore converted the lab times from UTC to TDT (see Table 3.1) and calculated the time delay between the signal arriving at the lab and the SSB by

$$\Delta t = \text{TDB - TDT} = \frac{1}{c}\vec{r}(t) \cdot \hat{n} + 1.658^{ms} \sin g(t) \qquad (3.12)$$

where $\vec{r}$(t) is a vector from the SSB to Allegro and $\hat{n}$ is the direction from the SSB to the source. The second term is a general relativistic correction due to the Sun's gravitational field and is of the order 1 ms. The angle $g(t)$ is proportional to the day of the year, as shown in Table 3.2.

Table 3.2: Value of the angle g in the general relativistic correction to the time delay for 1991-1994.

Year	g (degrees)
1991	356.38 + 0.98560028 × day of year
1992	356.13 + 0.98560028 × day of year
1993	356.85 + 0.98560028 × day of year
1994	356.60 + 0.98560028 × day of year

The right ascension (α_s-in hours, minutes, seconds) and declination (δ_s-in degrees, minutes, seconds) coordinates for each of the millisecond pulsars in 47 Tuc are

$$\hat{n} = (00:24:06 \pm 240'', \ -72:04:00 \pm 20'').$$

Right ascension and declination are defined in the celestial coordinate frame (CC frame with coordinates X,Y,Z). Celestial coordinates are centered at the SSB with $\hat{\mathbf{e}}_Z$ along the Earth's rotation axis (see Fig 3.3). $\hat{\mathbf{e}}_X$, $\hat{\mathbf{e}}_Y$ are in the Earth's equatorial plane with $\hat{\mathbf{e}}_X$ directed towards the intersection of the equatorial plane with the Earth's orbital plane (the ecliptic) at the vernal equinox. The opposite crossing of the equatorial plane by the ecliptic is called the autumnal equinox. Right ascension is measured in hours of angle (12 hrs = π radians) from the vernal equinox eastward along the celestial equator to the celestial object and declination is measured in degrees North or South of the equatorial plane.

Calculation of $\vec{r}$ in the CC frame was a two step process. First we used a GPS receiver to obtain the latitude and longitude coordinates of Allegro (30.245 N lat, 91.179 W long). These were then converted to cartesian coordinates in a frame centered at the Earth's center of mass. Second, the position of the center of mass

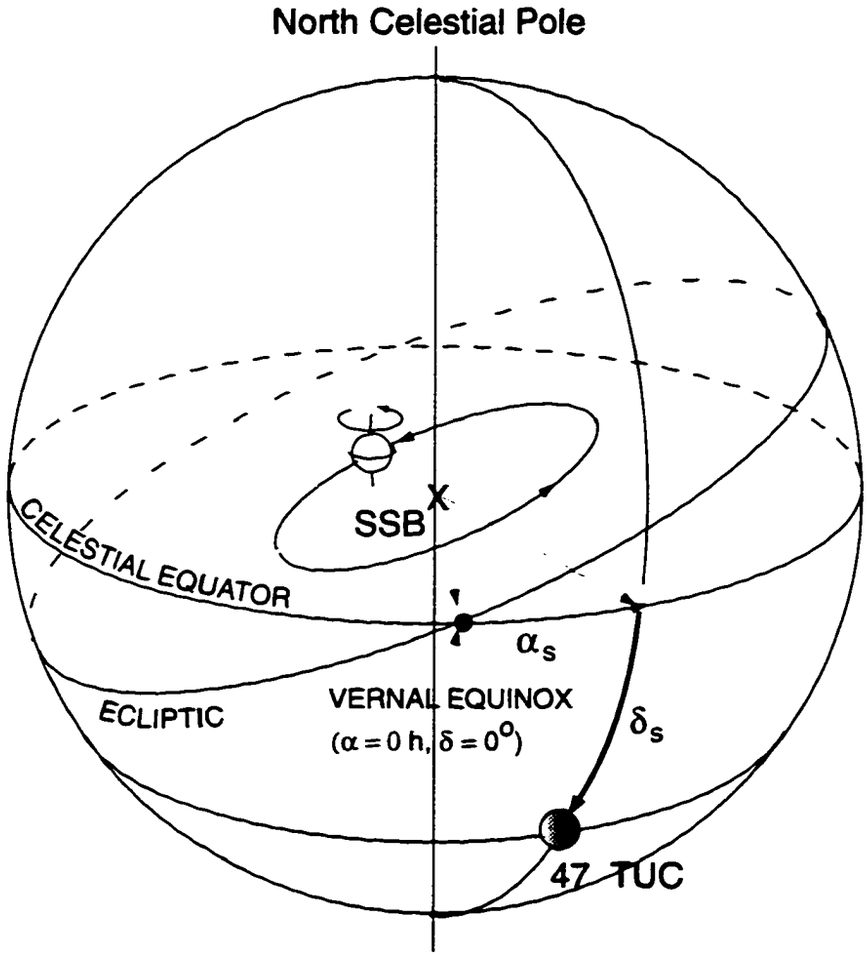

Figure 3.3: Celestial Coordinate Frame

of the Earth relative to the SSB was obtained. The two were added vectorally to produce $\vec{r}$. A commercially available software package from the U.S. Naval Observatory (MICA[1]) provided the position of the Earth's center of mass in cartesian coordinates at user-specified times. MICA uses the Jet Propulsion Laboratory DE200/LE200 ephemeris, the same ephemeris used as the basis for *The Astronomical Almanac*. For MICA, the times needed to be specified in TDT. MICA reported positions of the Earth's center of mass to the nearest 10^{-9} astronomical units (AU), which is of order 10^2 meters. This corresponded to 1/1000 of a wavelength for the signals of interest in this search, enabling an accurate tracking of the phase of the gravitational wave.

MICA produced a text file containing the cartesian coordinates of the Earth's center of mass with respect to the SSB at each requested time. Due to this somewhat awkward interface, we did not use MICA to get a positional reading at each sample time. Instead, we used MICA to provide a template for the Earth's center of mass each day. The template consisted of positional readings at 0,4,6,8,12,16,20, and 24 hours TDT of each day. Allegro's position at each sample time was obtained by interpolating between the template points using the Matlab *interp1* routine. This procedure was rigorously tested to insure that the interpolation results matched those directly calculated from MICA. The cartesian coordinates for the Earth's center of mass were converted to Allegro's distance from the SSB (r), Allegro's local sidereal time (T), and Allegro's declination (δ_A). Local sidereal time is defined as the intersection of the local meridian with the celestial equator measured

[1]Multiyear Interactive Computer Almanac, U.S. Naval Observatory, 3450 Mass. Ave., N.W. Washington, DC 20392

westward to the vernal equinox and is related to Universal Time (UT) by

$$T(\text{in hrs}) = T(0) + 1.00273791 * UT - A_l$$

where A_l is Allegro's longitude (in hours) and $T(0)$ is Greenwich sidereal time at 0 hrs UT. It is important to note that $T(0)$ changes with both the year and the day of the year. The scalar product between $\vec{r}$ and $\hat{n}$ was calculated by

$$\vec{r} \cdot \hat{n} = r\,(\sin\delta_A\,\sin\delta_s + \cos\delta_A\,\cos\delta_s\,\cos(T - \alpha_s))$$

and the corresponding time delay from Eq. 3.12.

3.2 Interaction with Allegro

A passing gravity wave provides the largest fractional change in the length of a bar. and therefore the largest signal in a bar detector, when its direction of propagation is perpendicular to the bar axis and one of the polarizations of the gravity wave lies along the bar axis. In general. the gravity wave is incident to the bar with some angle θ and polarization angle ϕ. Here the polarization angle is defined as the angle between the bar axis and the direction of the plus polarization of the gravity wave. Both angles are shown in Fig. 3.1.

For a gravity wave incident with an arbitrary orientation to the bar axis, it is only the component of the strain tensor along the bar axis which produces a detectable driving force on the bar. This force is commonly written as

$$F(t) = \frac{1}{2}\mu L_e \ddot{h}_b^{TT}(t) \tag{3.13}$$

where $\ddot{h}_b^{TT}(t)$ is the second time derivative of the strain component along the bar axis. The quantities μ and L_e are the effective mass and length of the first longitudinal eigenmode of the bar, obtained by solving the elastic equations of motion for a long, thin cylinder. The effective mass is equal to half the physical mass of the bar ($\mu = 1148$ kg) and $L_e = (4/\pi^2)$L where L is the actual length of the bar (3 m). The force acts on the bar alone as the transducer has too little mass to couple appreciably to the gravity wave.

To find the component of the gravity wave strain along the bar axis, we first define a "bar frame" with coordinates (x, y, z) centered at Allegro's center of mass with $\hat{\mathbf{e}}_z$ pointed towards the local zenith and $\hat{\mathbf{e}}_x$ aligned with the bar axis. The relative orientation of the bar frame to the wave frame, now translated so that its origin is also at Allegro's center of mass, is shown in Fig. 3.1. The component of the gravitational strain along $\hat{\mathbf{e}}_x$ is calculated by rotating the wave frame through ϕ around $\hat{\mathbf{e}}_{z'}$ and then by $\pi/2 - \theta$ around the resulting $\hat{\mathbf{e}}_{y'}$ axis, resulting in

$$h_b^{TT}(t) = \sin^2\theta \cos 2\phi\, h_+(t) + \sin^2\theta \sin 2\phi\, h_\times(t) \tag{3.14}$$

The expressions involving the angles θ, ϕ in Eq. 3.14 form what are called the reception patterns for Allegro, both of which change as the Earth moves with respect to the source. The changing bar sensitivity superimposes a roughly diurnal amplitude modulation on the kilohertz carrier wave of the gravitational radiation, as shown in Fig. 3.4. In signal processing this is called the *envelope* of the signal. The two polarizations of the gravity wave have essentially orthogonal envelopes.

To compute the reception patterns for a CW signal from 47 Tuc. we expressed both the bar frame and the wave frame in CC coordinates. The CC frame is related to the bar frame by the three rotation angles $(T, \pi/2 - l, \eta - \pi)$, where we have used the Euler y-convention [27] to define the axes of rotation. Again, T is the local sidereal time for Allegro, l is Allegro's latitude and η is the angle of the bar axis west of local North. The transformation matrix from CC coordinates to the bar frame is

$$\begin{bmatrix} -\cos\eta\sin l\cos T + \sin\eta\sin T & -\cos\eta\sin l\sin T - \sin\eta\cos T \ldots \\ \sin\eta\sin l\cos T + \cos\eta\sin T & \sin\eta\sin l\sin T - \cos\eta\cos T \ldots \\ -\cos l\cos T & \cos l\sin T \ldots \end{bmatrix}$$

$$\begin{bmatrix} \ldots -\cos\eta\cos l \\ \ldots \sin\eta\cos l \\ \ldots \sin l \end{bmatrix} . \tag{3.15}$$

The angles which relate the wave frame to the CC frame are $(\alpha_p, \pi/2 - \delta_p, -\psi)$, again using the Euler y-convention to define the axes of rotation. Here α_p is the right ascension associated with the wave's propagation and δ_p is the corresponding declination. ψ is the angle between the projection of the polarization axis of the gravity wave on the $(\hat{\mathbf{e}}_X, \hat{\mathbf{e}}_Y)$ plane and $\hat{\mathbf{e}}_X$. The direction of propagation of the gravity wave is related to the source direction by

$$\begin{aligned} \alpha_p &= \alpha_s + 12\text{hrs} \\ \delta_p &= -\delta_s . \end{aligned} \tag{3.16}$$

The transformation matrix from CC coordinates to the wave frame is

$$\begin{bmatrix} \cos\psi\sin\delta_p\cos\alpha_p + \sin\psi\sin\alpha_p & \cos\psi\sin\delta_p\sin\alpha_p - \sin\psi\cos\alpha_p & \ldots & \cos\psi\cos\delta_p \\ \sin\psi\sin\delta_p\cos\alpha_p - \sin\psi\sin\alpha_p & \sin\psi\sin\delta_p\sin\alpha_p - \cos\psi\cos\alpha_p & \ldots & \sin\psi\cos\delta_p \\ -\cos\delta_p\cos\alpha_p & -\cos\delta_p\sin\alpha_p & \ldots & \sin\delta_p \end{bmatrix} . \tag{3.17}$$

Having expressed the axes of both the wave frame and the bar frame in CC coordinates, the angle between the gravitational wave's direction of propagation and the bar axis was simply calculated from

$$\begin{aligned} \cos\theta &= \hat{\mathbf{e}}_x \cdot \hat{\mathbf{e}}_{z'} \\ &= \cos\eta\sin l\cos\delta_p\cos(T-\alpha_p) - \sin\eta\cos\delta_p\sin(T-\alpha_p) - \cos\eta\cos l\sin\delta_p \end{aligned}$$

and the desired modulation term by

$$\sin^2\theta = 1 - \cos^2\theta\,. \tag{3.18}$$

The angle between the polarization direction of the gravity wave and the bar axis is calculated from the following:

$$\begin{aligned} \cos\phi &= \hat{\mathbf{e}}_x \cdot \hat{\mathbf{e}}_{x'} \\ &= -\cos\psi(\cos\eta\sin l\sin\delta_p\cos(T-\alpha_p) - \sin\eta\sin\delta_p\sin(T-\alpha_p) \\ &\quad + \cos\eta\cos l\cos\delta_p) \\ &\quad + \sin\psi(\cos\eta\sin l\sin(T-\alpha_p) + \sin\eta\cos(T-\alpha_p)) \end{aligned}$$

$$\begin{aligned}\sin\phi &= \hat{\mathbf{e}}_x \cdot \hat{\mathbf{e}}_{y'} \\ &= -\sin\psi(\cos\eta\sin l\sin\delta_p\cos(T-\alpha_p) - \sin\eta\sin\delta_p\sin(T-\alpha_p) \\ &\quad + \cos\eta\cos l\cos\delta_p) \\ &\quad - \cos\psi(\cos\eta\sin l\sin(T-\alpha_p) + \sin\eta\cos(T-\alpha_p))\,.\end{aligned}$$

From these

$$\cos 2\phi = (\hat{\mathbf{e}}_x \cdot \hat{\mathbf{e}}_{x'})^2 - (\hat{\mathbf{e}}_x \cdot \hat{\mathbf{e}}_{y'})^2 \tag{3.19}$$

and

$$\sin 2\phi = 2(\hat{\mathbf{e}}_x \cdot \hat{\mathbf{e}}_{x'})\,(\hat{\mathbf{e}}_x \cdot \hat{\mathbf{e}}_{y'})\,. \tag{3.20}$$

The quantity ψ is the initial angle between the polarization direction of the gravity wave and the bar axis. It can also be described as the unknown phase of the signal envelope. This is most easily seen by defining

$$A(t) = \cos\eta\sin l\sin\delta_p\cos(T-\alpha_p) - \sin\eta\sin\delta_p\sin(T-\alpha_p) \tag{3.21}$$

and

$$B(t) = \cos\eta\sin l\sin(T-\alpha_p) + \sin\eta\cos(T-\alpha_p) \tag{3.22}$$

and substituting these into the expressions for $\cos 2\phi$ and $\sin 2\phi$. Both $A(t)$ and $B(t)$ are completely determined by the source location, the detector location, and the sidereal time. Making the substitutions, the angle ϕ separates into a known time dependent part and the unknown phase ψ:

$$\begin{aligned}\cos 2\phi(t) &= (A^2(t) - B^2(t))\cos 2\psi - 2A(t)\,B(t)\,\sin 2\psi \\ &\rightarrow \cos 2(\phi^{'}(t) + \psi) \end{aligned} \tag{3.23}$$

and

$$\begin{aligned}\sin 2\phi(t) &= 2\,A(t)\,B(t)\,\cos 2\psi + (A^2(t) - B^2(t))\,\sin 2\psi \\ &\rightarrow \sin 2(\phi^{'}(t) + \psi) \end{aligned} \tag{3.24}$$

where we have defined

$$\begin{aligned}\cos 2\phi^{'}(t) &= A^2(t) - B^2(t) \\ \sin 2\phi^{'}(t) &= 2A(t)\,B(t)\,. \end{aligned}$$

We further introduce the *complex* signal envelope for each polarization as

$$C(t) = \sin^2\theta(t)\cos 2\phi(t)\,e^{i\delta(t)} \tag{3.25}$$

for the plus polarization and

$$D(t) = \sin^2\theta(t)\sin\phi(t)\,e^{i\delta(t)} \tag{3.26}$$

for the cross polarization, where the phase shift of the arriving gravity wave has been included in the envelope.

Taking the Fourier transform of both sides of Eq. 3.13 the driving force on the bar is

$$\tilde{F}(\omega) \simeq -\frac{1}{2}\mu L_e \omega^2 \tilde{h}_b(\omega) \tag{3.27}$$

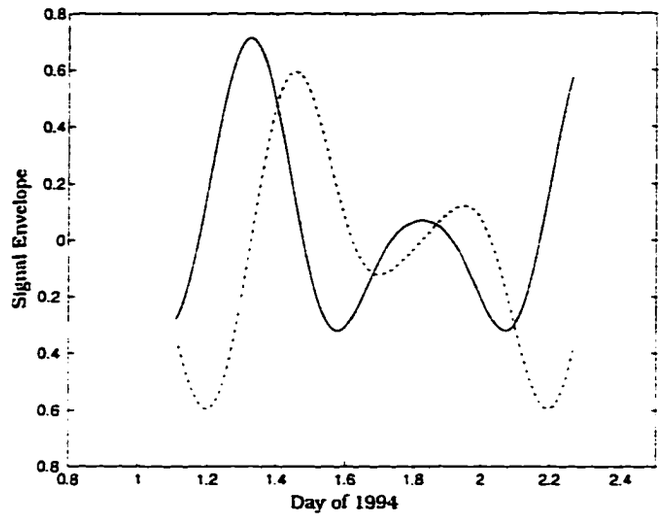

Figure 3.4: The reception patterns for the plus polarization (solid line) and the cross polarization (dot-dashed line) of a gravity wave from 47 Tuc for ψ=0.

where the Fourier transform of the signal is

$$\begin{aligned}\tilde{h}_b(\omega) &= \frac{1}{2}h_c\,(1+\cos^2\gamma)\,(\cos 2\psi\,\tilde{C}(\omega-\omega_s)-\sin 2\psi\,\tilde{D}(\omega-\omega_s)\,) \\ &\quad +\frac{1}{2}h_c\,(2\cos\gamma)\,(\cos 2\psi\,\tilde{D}(\omega-\omega_s)+\sin 2\psi\,\tilde{C}(\omega-\omega_s)\,) \qquad (3.28)\end{aligned}$$

with identical terms at negative frequencies. The driving force on the bar produced a voltage out of the SQUID electronics given by

$$\tilde{M}(\omega)=\tilde{G}(\omega)\,\tilde{F}(\omega) \qquad (3.29)$$

where $\tilde{G}(\omega)$ is the frequency response of the voltage out of the SQUID electronics to a force applied to the bar. The shape of $\tilde{G}(\omega)$ is shown in Fig. 2.4 b) and its theoretical calculation is described in detail in section 3.2.1.

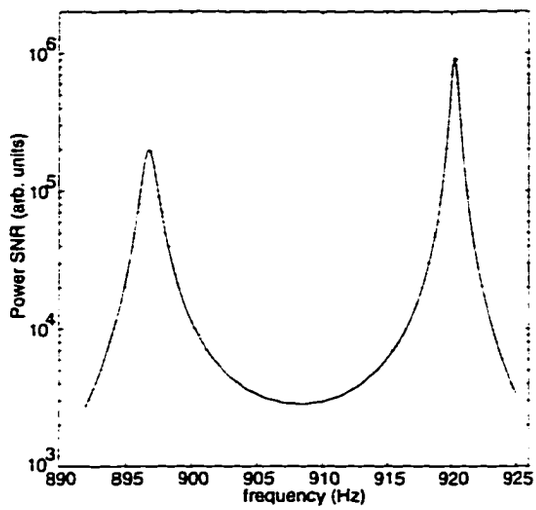

Figure 3.5: The Allegro power signal to noise ratio.

As was explained in section 2.2.1. the voltage out of the SQUID electronics is demodulated from 1 kHz down to approximately 10 Hz before being sampled and written to disk. To save on analysis time and storage requirements. we further demodulated the data in software to a 1 Hz bandwidth around each of the resonant modes. restricting the search to the intervals 896.3-897.3 Hz and 919.76-920.76 Hz where Allegro is the most sensitive (see Fig. 3.5). The details of demodulating the data to its final bandwidth are described in section 3.3.1.

After the software demodulation. the voltage produced by the driving CW force is

$$\tilde{M}_{k'} = \tilde{G}_k \tilde{F}_k e^{i\phi_r} \tag{3.30}$$

which is essentially Eq. 3.29 expressed in terms of discrete Fourier components and not in the continuous frequency domain. The demodulated frequencies were given

by $\omega_{k'} = 2\pi k'/N\Delta t$ where Δt is the time between samples (8 ms) and N is the total number of samples involved in a single discrete Fourier transform (the details for determining N are given in section 3.2.2). The demodulated frequency components were bandlimited to $-2\pi(.5) < \omega_{k'} < 2\pi(.5)$. They were related to the original kilohertz frequencies by $\omega_{k'} = \omega_k - \omega_c$, where ω_c is the reference frequency used in the software demodulation. The reference frequency is discussed in section 3.3.1. The extra factor e^{ϕ_r} is the unknown phase between the carrier wave of the CW signal and the oscillator providing the reference signal to the lockin detector.

By substituting Eq. 3.27 and Eq. 3.28 into Eq. 3.30, we obtained the form of the CW signal which was targeted by the analysis:

$$\begin{aligned} M_{k'} = \; & (1+\cos^2\gamma)\, h_c\, e^{i\phi_r}\, \tilde{R}_k\, (\cos 2\psi\, \tilde{C}_{k-s} + \sin 2\psi \tilde{D}_{k-s}) - \\ & (2\cos\gamma)\, h_c\, e^{(i\phi_r+\pi/2)}\, \tilde{R}_k\, (\cos 2\psi\, \tilde{D}_{k-s} + \sin 2\psi \tilde{C}_{k-s}) \end{aligned} \tag{3.31}$$

where we have collected a number of terms into

$$\tilde{R}_k = \frac{1}{4}\mu L_e\, \omega_k^2 \tilde{G}_k$$

for convenience and ω_s is the signal frequency.

3.2.1 The Detector Response

As can be seen from Eq. 3.31, it was necessary to calculate the bar response function in order to explicitly know the form of the CW signal in the recorded Allegro data. To do this we used the "full" model of the Allegro detector, which is essentially that shown in Fig. 2.2 (with the associated equations of motion), except the

superconducting circuitry is also included. This model has been written down and solved computationally elsewhere [33, 34].

As it was necessary for later analysis, we also calculated the total noise power spectral density (PSD) of the stationary noise processes effecting the antenna. Both quantities are provided as a current at the SQUID input. The response function converts a force on the bar to a current at the SQUID input and has units of amperes/Newtons. The noise PSD has units amperes^2/Hz. Conversion to voltages written to disk, called "digital units" (du), was done by scaling the white noise level of the noise PSD as provided by the model to the power spectrum as calculated from the recorded data. The scaling factor was found to be $c_{da} = 2.27 \times 10^{25}$ du^2/amps^2. The combination $\sqrt{c_{da}}\tilde{G}_k$ is what is presented as simply $\tilde{G}_k$ (with units volts/newton) in Eq. 3.30.

With the high frequency resolution of this search, slight changes in the operating conditions of the detector produced noticeable effects in the data which were not explicitly included in the model. For example, slight temperature changes inside the dewar shifted the antenna resonant frequencies over time as shown in Fig. 3.6. To account for the changing resonant frequencies, the noise PSD was calculated from the model and shifted in frequency so that it matched the PSD as calculated from the actual data. This information was then used to shift the antenna response function for each mode to the proper frequency. Figure 3.7 shows the plus mode noise PSD after alignment and Fig. 3.8 the same information for the minus mode.

The other condition effecting the antenna was the amount of feedback used to damp the mode amplitudes. The feedback decreased the damping times of each

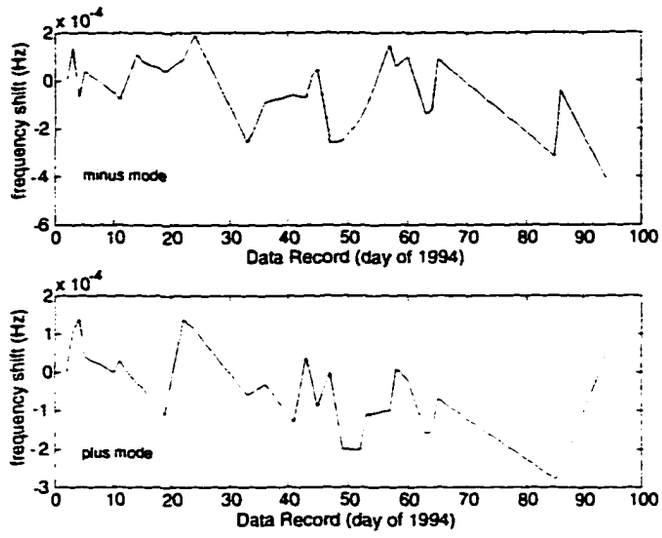

Figure 3.6: The change in the resonant frequencies over the first three months of 1994. The amount of drift is given relative to the first measured value.

mode from tens of minutes to on the order of one minute. Calibration pulses and large burst events were used to periodically measure the mode damping times and their values in the model were adjusted accordingly. Since the amount of feedback was small and added no noise to the system, the values of the Langevin forces acting on the bar remained constant in the equations of motion.

3.2.2 Frequency Resolution

It has become conventional in this field to describe the stationary noise level of a detector as an incident flux of gravity waves on the detector (see Fig. 2.4 c)

$$\tilde{h}_{rms} = \sqrt{S_h \Delta f}$$

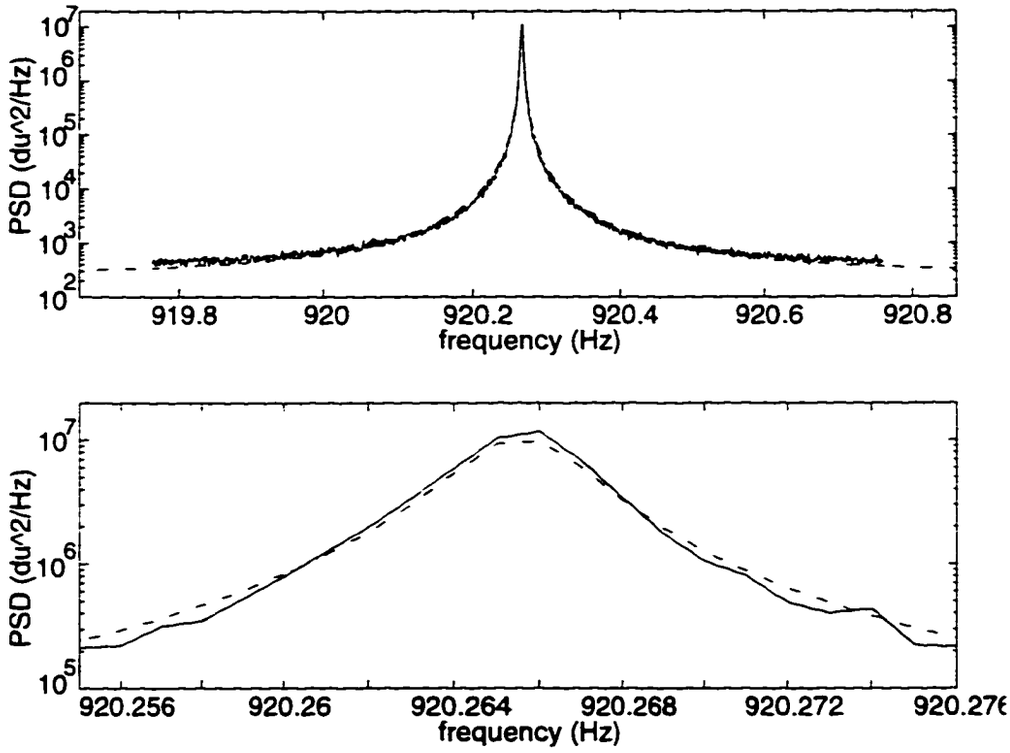

Figure 3.7: The noise power spectral density for the plus resonant mode. The solid line is the PSD calculated from the data, the dot-dashed line is calculated from the model. The bottom plot shows the frequencies near resonance.

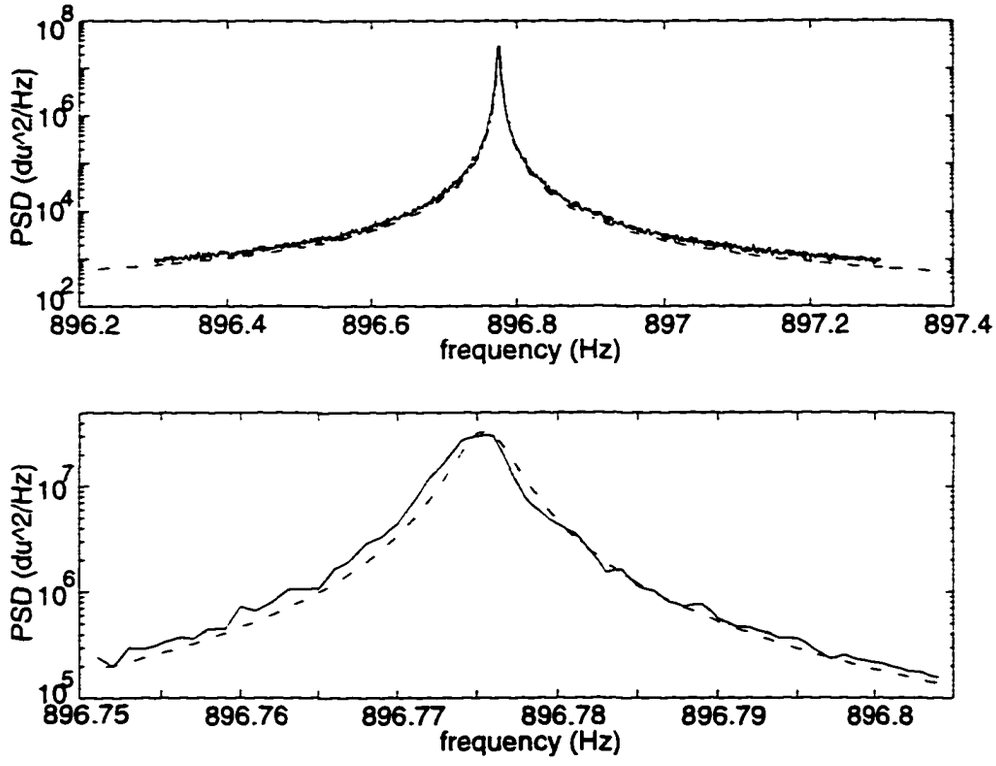

Figure 3.8: The noise power spectral density for the minus resonant mode. The solid line is the PSD calculated from the data, the dot-dashed line is calculated from the model. The bottom plot shows the frequencies near resonance.

where S_h is the noise PSD written as an incident flux of gravity waves. From this it is easily seen that the noise level of the search decreases as the square root of the frequency resolution. Therefore, we would have liked to be limited only by the amount of data the computer could Fourier transform at one time. Unfortunately, this was not the case as the frequency resolution of the search was limited instead by our electronics.

The reference signal provided to the lockin detector by the Hewlett-Packard function generator (HP) had some error in the frequency it generated. The measured value of this uncertainty set the limit on the minimum frequency spacing between adjacent resolvable signals. To measure the frequency uncertainty the long-term phase drift between the HP and the oscillator providing the driving voltage to the calibrator at 865 Hz was analyzed. The calibration signal was alternately provided by three oscillators in turn. (1) a SRS model DS345 function generator. (2) the same SRS but phase-locked to a high-stability Austron oscillator. (3) a SRS model DS345 function generator with the high-stability option (HSO). We first narrowbanded the signal at 865 Hz with the procedure explained in the previous section. The phase difference between oscillators was measured as the ratio of the imaginary calibration signal amplitude to the real calibration signal amplitude. To isolate the long-term phase behavior, we averaged the phase difference over one record and repeated the measurement for each record for an entire days worth of data (4320 records). The frequency drift from one record to the next is simply given by

$$\Delta f = \frac{1}{2\pi}\frac{\Delta\phi}{\Delta t}$$

where $\Delta\phi$ is the difference between consecutive record averages and Δt is the time between phase measurements (20s). The frequency drift was measured over a number of days, the results of which are shown in Table 3.3. It is important to note that this procedure resulted in a determination of the phase drift between TWO oscillators, not the overall drift of ONE oscillator. Figure 3.9 shows the frequency drift between the SRS (no option) and the SRS equipped with the HSO. It is clear that the large drifts were not due to the HP. Figure 3.10 shows the results of the HP/SRS (with HSO) and HP/SRS (synched to the Austron). We could not determine uniquely which oscillator was responsible for the observed uncertainty in frequency, so to be on the safe side we associated all the drift with the HP. Examination of Table 3.3 reveals that for the majority of available data, $\Delta f \sim 10^{-6}$ Hz. However, since there were only a few measurements, the least optimistic value (from day 311) is the number we decided to use. This allowed a small margin for error as well as simplifying the data handling requirements. Performing a discrete Fourier transform on 10^5 seconds (slightly less than 28 hours) of data resulted in the desired frequency resolution. With a sampling rate of 2.5 samples/second, there were $N = 2.5 \times 10^5$ samples of data to Fourier transform and analyzed at one time.

Since there is no known pulsar with the right rotation rate to produce gravity waves detectable be Allegro, we *assumed* that there was a *potential* signal in each frequency bin. This approach resulted in having to optimally filter for 2×10^5 possible signals at different frequencies (2 modes $\times$ 1 Hz bandwidth/mode $\div 10^{-5}$ Hz frequency resolution). Including filtering for each polarization and having to

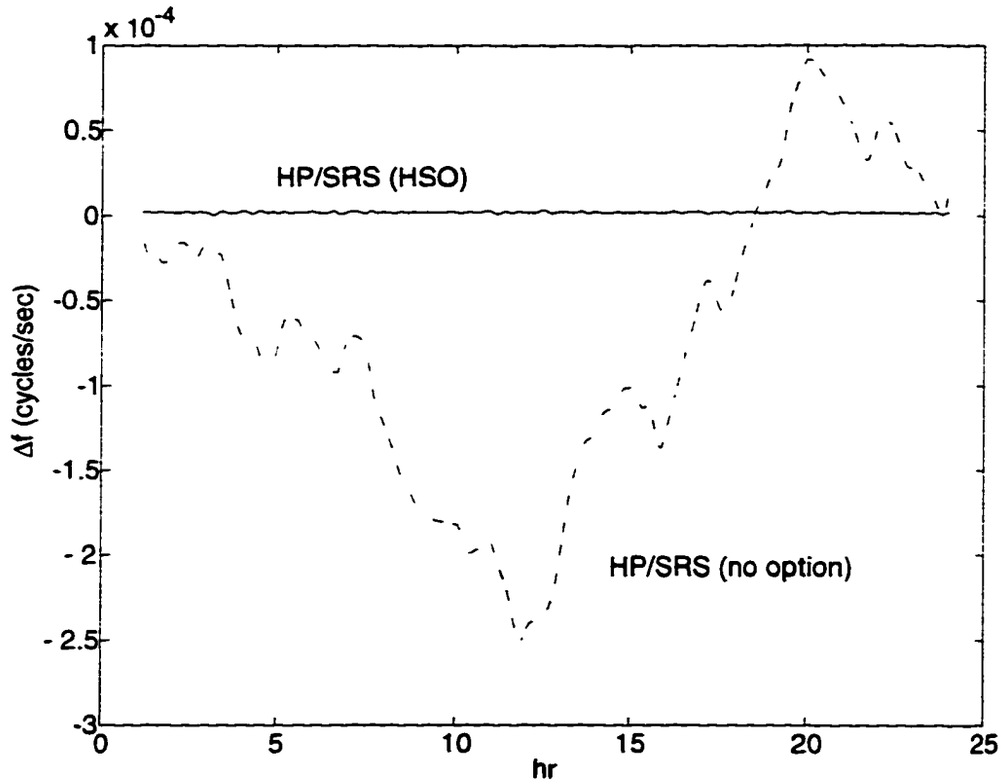

Figure 3.9: Frequency drift between HP/SRS (no option) and HP/SRS (HSO) over a day.

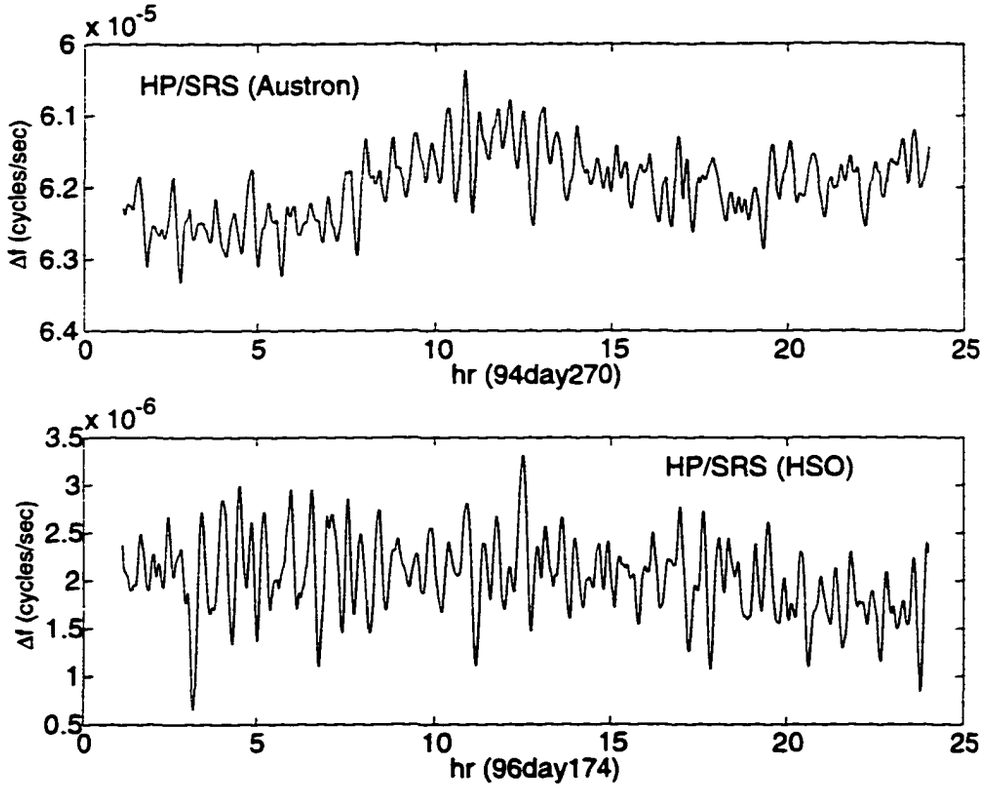

Figure 3.10: Frequency drift as measured with the high-stability oscillators.

Table 3.3: The measured uncertainty in the frequency provided to the lockin by the HP function generator.

date (yr/day of year)	Δf ($\times 10^{-6}$ Hz)
94/269	±1.5
94/270	±1.5
94/311	±5.0
96/166	±1.5
96/168	±1.0
96/174	±1.5

calculate the signal to noise ratio for each filter (all described in the following sections), the analysis became very time consuming on a DEC 3000 AXP. It was possible, however, to decrease the computational times by two procedures which are described in section 3.5.2.

3.3 CW Analysis

Equation 3.31 gives the form of the CW signal as it would appear in the Allegro data. We now ask: "Is this signal in the data?" Since the strength of the signal is small compared to the detector noise (otherwise we would see it on a spectrum analyzer!), some work needs to be done to answer this question. There is an enormous amount of literature on the subject of detecting signals buried in noisy data. The techniques and notation used in this section, especially section 3.5 and section 3.5.1, will closely follow that of "Extraction of Signals from Noise", L. A. Wainstein and V. D. Zubakov, Chapter 5.

Essentially, the analysis was a three step process, with each stage being described in detail below. First, the recorded data was read off tape and narrow-banded to a 1 Hz bandwidth at each resonant mode. Then the mode amplitudes

were "cleaned" of large, transient events. Finally, the cleaned data was DFT'ed and optimal filters for the signal of Eq. 3.31 were applied in the discrete frequency domain.

3.3.1 Narrowbanding the Data

Narrowbanding the data around each of the resonant modes was a three step process: demodulation, applying anti-alias filters and then resampling the data. To begin, one record (20s) was read off disk and the in-phase and quadrature outputs of the lockin combined to form the complex amplitude

$$\mathbf{z} = \mathbf{x} + i\mathbf{y}$$

where $\mathbf{x} = \{x(t_1), x(t_2), \ldots, x(t_N)\} = \{x_1, x_2, \ldots, x_N\}$ represents the time-ordered sequence of N samples from the in-phase channel, $\mathbf{y}$ the time-ordered sequence from the quadrature channel and $i = \sqrt{-1}$. Demodulation to the mode frequencies was performed by simply multiplying the time sequence of the complex amplitude $\mathbf{z}$ by the time-dependent phase factor

$$\mathbf{z}\,(demod) = \mathbf{z}\,exp\{-2\pi\, i(f_c - f_r)\,\mathbf{t}\}$$

where the sample times $\mathbf{t}$ were reported in seconds UTC from the start of the year and f_r was the reference frequency supplied to the EG&G PAR 5210 lockin detector. The software reference frequency, f_c, was specified by each of the following frequencies in turn:

$$f_c = \begin{cases} 896.80 & \text{Hz for the minus mode} \\ 920.26 & \text{Hz for the plus mode} \\ 865.00 & \text{Hz for the continuous systems test .} \end{cases}$$

After demodulation there were three separate data streams: the amplitude of the antenna oscillations at the plus resonant mode, the amplitude at the minus resonant mode, and the amplitude of the continuous calibration signal. The calibration signal was included as a useful diagnostic tool. The combination $f_c - f_r$ assured that regardless of the actual value of the lockin reference frequency, which changed over time, a constant bandwidth was analyzed. The resulting complex amplitudes were filtered with a 6th order Butterworth filter to remove aliasing effects before the data was resampled. The Butterworth filter coefficients were obtained using the Matlab *butter* routine and applied to the data with the *filter* routine. The cutoff frequency was chosen to be 1 Hz so that the data within $\pm 1/2$ Hz of f_c was unaffected by either the low pass filtering or aliasing. The amplitudes were then resampled at 2.5 samples/second and recorded. The next record was read in and the procedure repeated with the results appended to those of the previous record. This continued until N=2.5×10^5 consecutive samples, roughly 28 hours of data, had been accumulated. The resulting array was then Fourier transformed using the Matlab *fft* routine to produce the Fourier coefficients of the narrowbanded signal, $M_{k'}$. It is important to note that the bandwidth of the search could be extended simply by resampling the data at a higher rate, or the search could be shifted to a different frequency range by demodulating at other reference frequencies.

3.4 Data Selection

Even with Allegro's high duty cycle, there were periods of missing or unusable data. In this section we describe the nature of the down times and how accumulation of data was affected.

Data losses came in basically three flavors. (1) Transient electronic effects which lasted on the order of a second. (2) Longer periods when the detector was undergoing some form of maintenance. (3) The clock losing phase lock to WWVB. The transient disturbances were the most frequent, occurring at a rate of a couple per day. They usually involved a sudden change in the flux threading the SQUID loop (hence the name "flux jumps"). The majority of the flux jumps occurred when the dc level of the SQUID reached a pre-determined maximum (5 volts). The electronics controlling the SQUID then reset the dc voltage to zero, causing a short and violent jump in the x and y channels of the data, as shown in Fig. 3.11. Frequently electronic interference reaching the SQUID caused flux jumps. In the past when data tapes were erased (the degaussing takes place in a separate room from the main experiment), the end of the degaussing cycle produced a noise spike which traveled through the wiring in the wall, through the computers, through the A/D box, and from there to the SQUID. Once recognized, an isolating transformer was placed between the degausser and the wall socket, fixing the problem. Another common type of transient signal is a "spike". These look similar to flux jumps in the data and there is some suspicion that they are in fact flux jumps, but essentially they are of unknown origin. All of these noisy periods were short enough so that the effected data could be removed and the resulting gap interpolated across. This

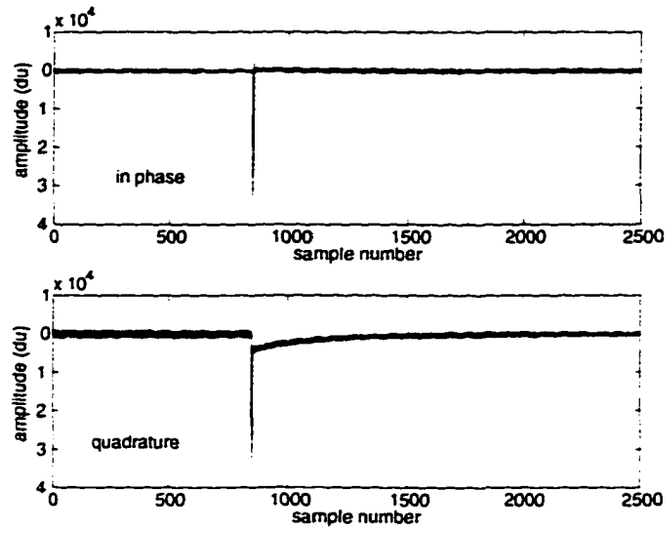

Figure 3.11: A SQUID reset in the raw data.

was done using the Matlab *interp1* routine. Interpolation was performed on the resampled data. It was usual to interpolate across 1-5 seconds of data. using the 10-20 seconds of data before and after the gap for the interpolation template. An example of the interpolation is shown in Fig. 3.12.

As described in Chapter 1. the Allegro detector (and in fact all gravitational wave detectors have this problem) was subject to occasional burst events of large amplitude. In a CW search. a burst event produces unwanted sidebands in the spectrum of the data. To avoid corrupting the spectra, we used a two step process. The short period of the actual excitation was interpolated across as described previously. The 1-2 minutes of mode amplitude decay following the excitation, however, was perfectly good data for a CW search. We therefore decided not to remove this data or interpolate across it. Instead, we fit the in-phase and quadrature amplitudes of each mode to a decaying sinusoid and subtracted the

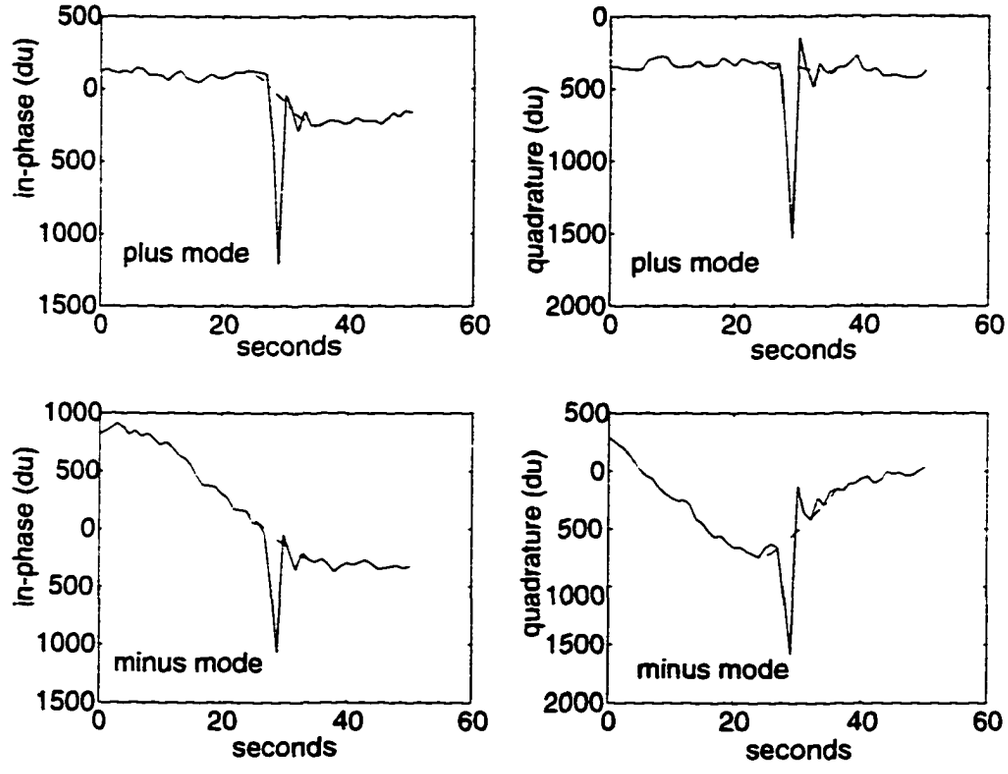

Figure 3.12: The effects of interpolating across the reset of Fig. 3.11. The solid lines are the real and imaginary mode amplitudes showing the transient nature of the reset. The dot-dash line is the interpolation.

fit from the data. This had the effect of preserving any CW signal present while removing the disruptive large amplitude. Of course, if the excitation was so large that the A/D's became saturated, the analysis had to be stopped at that point and restarted after the detector had calmed down.

For longer sections of unusable data or for periods of missing data, the analysis was stopped and restarted after the disturbance. By "restarted" we mean that the accumulation of data was stopped, the counter N was reset to zero, and the accumulation was restarted from the beginning. The most common cause of data loss was transferring liquid helium into the dewar which removed a couple of hours of data every week. Another cause of long stretches of unusable data were large excitations of the resonant modes due to earthquakes around the globe. Earthquakes were identified by a unique signature in the low frequency housekeeping channel. It was usual for an earthquake to produce multiple large excitations over a few tens of minutes, often resulting in saturation of the A/D's. Computer down time, calibration of the detector and other maintenance all caused gaps in the data, although infrequently. Careful attention to where the large gaps were situated allowed for the maximum amount of data to be utilized. This information was obtained from the lab log book and the daily electronic log files.

The final type of data loss was associated with the WWVB clock. Frequently when the weather between Baton Rouge and NIST at Boulder, Colorado was bad, the clock we used to control the sampling of the data lost phase lock to the WWVB radio signal. When this happened, the clock's internal oscillator "freewheeled" with the result that the time between samples was no longer consistently 8 ms.

Deviations in the sampling rate from 8 ms were called "timing jumps". A jump in the time between when samples were taken produced a corresponding jump in the phase of modes and the calibrator signal as shown in Fig. 3.13. The most frequent jumps were on the order of 1-2 ms, producing a phase jump in a sinusoidal signal at the mode frequencies of approximately 1/100 of a cycle. This was considered an acceptable level of uncertainty in the ability to track the phase of a potential gravity wave signal. These small jumps were noted but ignored. Larger jumps produced correspondingly larger jumps in phase and were considered unacceptable. When they occurred, the analysis was stopped at the timing jump and restarted again after the glitch. The frequency and size of the timing jumps were highly variable. During the winter of 1994 the smaller jumps occurred almost once per day while the larger jumps rarely happened. By the spring of that year, the trend was reversed and much data was lost due to the inconsistency of the clock. It was long known that the clock would occasionally lose the WWVB signal, but the extent of the problem was not known until this research.

3.5 The Likelihood Function

Suppose we have the time-ordered, digitized detector output

$$\mathbf{z} = \mathbf{x} + i\mathbf{y}$$

as presented previously, except now the data includes zero mean, Gaussian distributed noise and may possibly not include the signal. That being the case, $\mathbf{z}$ involves one of two processes:

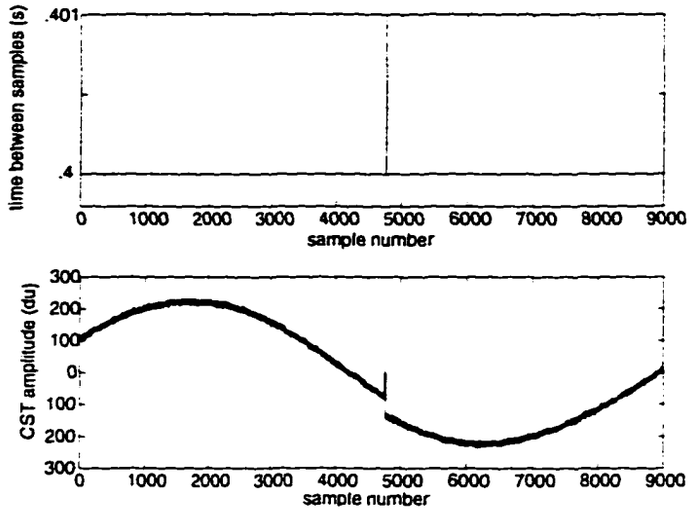

Figure 3.13: A 1 ms jump in the sampling time as it appears in the CST signal.

$$\begin{aligned} \mathbf{z} &= \mathbf{m} + \mathbf{n} \quad \text{if the signal as identified by } \mathbf{m} \text{ is present in the noise } \mathbf{n} \\ &= \mathbf{n} \quad \text{if no signal is present.} \end{aligned}$$

From the statistical properties of the stationary noise acting on the detector we can calculate the probability that the observed data stream, $\mathbf{z}$, was due to entirely to noise. Given the form of the signal we can also calculate the probability that the data was a mixture of signal and noise. If this latter probability is sufficiently high, it indicates the detection of a CW source. The probability that the signal is present in the data is expressed using Bayes' Rule, which is simply a re-statement of the definition of conditional probability:

$$P_{\mathbf{z}}(\mathbf{m}[\tau]) = \frac{p(\mathbf{m}[\tau])\, P_{\mathbf{m}[\tau]}(\mathbf{z})}{P(\mathbf{z})} \tag{3.32}$$

where the various terms involved in forming the conditional probability are described below.

$P_{\mathbf{z}}(\mathbf{m}[\tau])$ is the *a posteriori* probability that given the data $\mathbf{z}$ has been collected, the useful signal is present with parameters τ in the range $(\tau,\ \tau + d\tau)$.

$p(\mathbf{m}[\tau])$ is the *a priori* probability density that the useful signal occurs with parameters τ in the range $(\tau,\ \tau + d\tau)$.

$P_{\mathbf{m}[\tau]}(\mathbf{z})$ is the conditional probability of receiving the observed detector output given that the signal is present with parameters τ in the range $(\tau,\ \tau + d\tau)$.

$P(\mathbf{z})$ is the *a priori* probability of receiving the observed detector output. Here the parameter τ is used to represent all the unknown quantities that specify the signal. Specifically,

$$\tau = \{a, b, \psi, \phi_\tau\}$$

where $a = (1 + \cos^2\gamma)\, h_c$ and $b = (2\cos\gamma)\, h_c$. The signal frequency, which is also an unknown quantity, is not included in the list for reasons described later. We further expand the *a priori* probability of receiving the observed data under the assumptions that the signal is present and that the signal is absent, so that

$$P(\mathbf{z}) = \int p(\mathbf{m}[\tau])\, P_{\mathbf{m}[\tau]}(\mathbf{z})\, d\tau + P(0) P_0(\mathbf{z})$$

and

$$p(\mathbf{m}[\tau]) = P(\mathbf{m})\, p_m(\tau).$$

P_0 is the *a priori* probability the signal is absent.

$P_0(\mathbf{z})$ is the conditional probability of receiving the observed detector output given that the signal is absent.

$p_{\mathbf{m}}(\tau)$ is the conditional probability density that, given the signal is present, it has parameters τ in the range $(\tau, \tau + d\tau)$.

$P(\mathbf{m})$ is referred to as the "prior" probability or simply the "prior" because it describes the analyst's expectation of the signal *before* any data has been collected. In this instance the prior is the probability distribution which describes the possible amplitudes of each polarization of the gravity wave and the distributions of the unknown carrier phase and envelope phase.

The conditional probability is normalized so that

$$\int p_{\mathbf{m}}(\tau)d\tau = \int p_{\mathbf{m}}(\tau_1, \tau_2, \ldots)d\tau_1 d\tau_2 \ldots = 1.$$

Substituting for $P(\mathbf{z})$ and $p(\mathbf{m}[\tau])$ in Eq. 3.32 and rearranging terms, the probability that the signal is in the data can be expressed as

$$P_{\mathbf{z}}(\mathbf{m}[\tau]) = \frac{\Lambda(\tau)}{\Lambda + P(0)/P(\mathbf{m})} \tag{3.33}$$

where we have introduced the quantities

$$\Lambda(\tau) = p_{\mathbf{m}}(\tau)\, P_{\mathbf{m}[\tau]}(\mathbf{z})/P_0(\mathbf{z})$$

and

$$\Lambda = \int \Lambda(\tau)d\tau\,.$$

$\Lambda(\tau)$ is called the likelihood ratio for measuring the parameters τ.

At this stage the decision was made *not* to explicitly calculate the probability that the signal was present in the data. Instead we utilized the fact that $P_{\mathbf{z}}(\mathbf{m}[\tau])$ is

an increasing function of $\Lambda(\tau)$, so that the larger the likelihood function, the higher the probability the data included the signal. Furthermore, the assumption was made that the conditional probabilities for the signal were constant. Determination of the signal's presence or absence is now dependent only on the ratio of conditional probabilities

$$\frac{P_{\mathbf{m}}(\mathbf{z})}{P_0(\mathbf{z})}.$$

In situations where not much data is available, this may not be the optimal procedure. With almost 5 years of Allegro data, the prior probabilities should have very little effect on the outcome of the experiment so we proceed as described.

In the absence of a signal, the samples of $\mathbf{z}$ are jointly Gaussian with a distribution given by [22, eq. 59.26]

$$P_0(\mathbf{z}) = \frac{1}{(4\pi)^N ||R_{gh}||} \exp(-\frac{1}{2} \sum_{g,h=0}^{N-1} R_{gh}^{-1} z_g z_h^*) \tag{3.34}$$

where

$$R_{gh} = R(|g-h|\Delta t)$$

is the autocorrelation matrix of the noise and $||R_{gh}||$ is the determinate of R_{gh}. Since $\mathbf{z}$ is complex, R_{gh} has the following properties:

$$R_{gh} = \Re(R_{gh}) + i\Im(R_{gh})$$

with

$$\begin{aligned} \Re(R_{gh}) &= \Re(R_{hg}) \\ \Im(R_{gh}) &= -\Im(R_{hg}) \end{aligned} \tag{3.35}$$

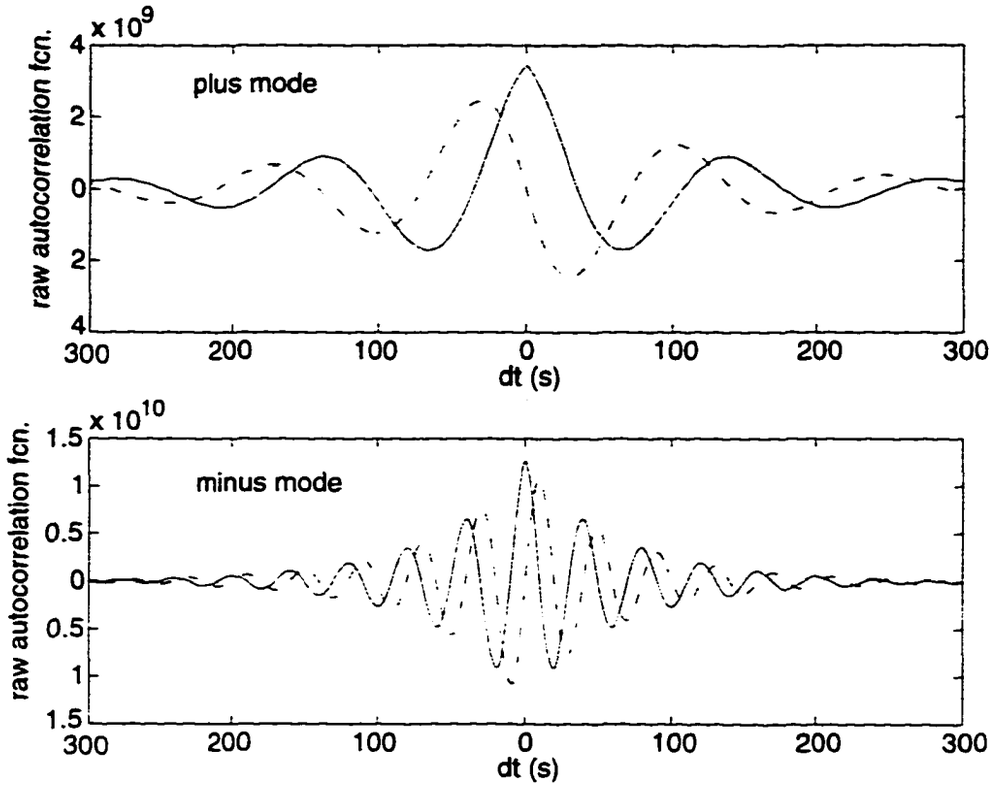

Figure 3.14: The measured Allegro autocorrelation function. The solid line is the real part of the autocorrelation function. the dashed line the imaginary.

where $\Re$ means "take the real part" and $\Im$ means "take the imaginary part". Figure 3.14 shows the autocorrelation function for for each of Allegro's resonant modes.

If the data also includes the signal. the distribution is slightly different

$$P_{\mathbf{m}}(\mathbf{z}) = \frac{1}{(4\pi)^N ||R_{gh}||} \exp(-\frac{1}{2} \sum_{g,h=0}^{N-1} R_{gh}^{-1}(z_g - m_g)(z_h - m_h)^*). \qquad (3.36)$$

The ratio of Eq.s 3.36 to Eq. 3.34, using the properties of the autocorrelation

matrix from Eq. 3.35, is

$$\frac{P_{\mathbf{m}}(\mathbf{z})}{P_0(\mathbf{z})} = \exp\{\Re(\sum_{g,h=0}^{N-1} R_{gh}^{-1} z_g m_h^*) - \frac{1}{2}\sum_{g,h=0}^{N-1} R_{gh}^{-1} m_g m_h^*\} \tag{3.37}$$

It can be shown that [31]

$$\sum_{g,h=0}^{N-1} R_{gh}^{-1} m_g m_h^* = 2\sum_{k=0}^{N-1} \frac{\tilde{M}_k \tilde{M}_k^*}{S_{nk}^{(1)}} \Delta f \tag{3.38}$$

where $\tilde{M}_k$ is the Fourier component of the signal at $\omega_k = 2\pi k/N\Delta t$ and $S_{nk}^{(1)}$ is Fourier component of the one-sided power spectral density of the Gaussian noise at ω_k . Using Eq. 3.31 and Eq. 3.38, we rewrite Eq. 3.37 as

$$\frac{P_{\mathbf{m}}(\mathbf{z})}{P_0(\mathbf{z})} = \exp\{\Re(q) - \rho^2/2\} \tag{3.39}$$

where

$$q = 2\sum_{k=0}^{N-1} \frac{\tilde{Z}_k \tilde{M}_k^*}{S_{nk}^{(1)}} \Delta f \tag{3.40}$$

and

$$\rho^2 = 2\sum_{k=0}^{N-1} \frac{|\tilde{M}_k|^2}{S_{nk}^{(1)}} \Delta f\,. \tag{3.41}$$

3.5.1 Optimal Filtering

The expressions for q and ρ^2 were arrived at from a statistical argument of signal present versus signal absent. Both are well known quantities from the theory of signal detection. q is the output of applying the optimal linear filter to the data

in the discrete frequency domain. The optimal linear filter maximizes the signal to noise ratio for a given signal and detector noise PSD. The signal to noise ratio (power) is defined as the quantity ρ^2 for a one-sided noise PSD. Up to a constant phase factor. the optimal filter coefficients in the (continuous) frequency domain are given by $\tilde{M}^*(\omega)/S_n(\omega)$ where $\tilde{M}^*(\omega)$ is the complex conjugate of the Fourier transform of the anticipated signal and $S_n(\omega)$ is the power spectrum of the detector noise. The optimal filter is applied to the collected data (again in the continuous frequency domain) by

$$q = \int_{-\infty}^{\infty} \frac{\tilde{Z}(\omega)\tilde{M}^*(\omega)}{S_n(\omega)} df$$

where we refer to q as the "filtered output".

Substituting Eq. 3.31 for $\tilde{M}_k$ in Eq. 3.40:

$$\begin{aligned} q &= 2\Delta f\, e^{-i\phi_r} \sum_{k=0}^{N-1} \frac{\tilde{Z}_k \tilde{R}_k^*}{S_{nk}^{(1)}} \times (\, a\cos 2\psi \tilde{C}_{k-s}^* + a\sin 2\psi \tilde{D}_{k-s}^* \\ &\quad -ib\cos 2\psi \tilde{D}_{k-s}^* + ib\sin 2\psi \tilde{C}_{k-s}^* \,) \,. \end{aligned} \tag{3.42}$$

As can be seen from Eq. 3.42 there are four separate filters to apply to the data. given by:

$$\tilde{R}_k^*/S_{nk}^{(1)} \times \{\tilde{C}_{k-s}^*, \tilde{D}_{k-s}^*, i\tilde{D}_{k-s}^*, i\tilde{C}_{k-s}^*\} \,.$$

The output produced after applying each filter to the data provides an estimate of a particular combination of the signal parameters $\{a, b, \psi, \phi_r\}$, as shown below.

$$\begin{aligned} q_1 \rightarrow \tilde{C}_{k-s}^* &\rightarrow a\, e^{i\phi_r} \cos 2\psi \\ q_2 \rightarrow \tilde{D}_{k-s}^* &\rightarrow a\, e^{i\phi_r} \sin 2\psi \end{aligned}$$

$$q_3 \rightarrow i\tilde{D}^*_{k-s} \rightarrow be^{i\phi_r}\cos 2\psi$$
$$q_4 \rightarrow i\tilde{C}^*_{k-s} \rightarrow be^{i\phi_r}\sin 2\psi \qquad (3.43)$$

The filter outputs can then be combined to estimate the amplitude of each polarization, the polarization direction of the gravity wave, and the initial phase of the gravity wave. From knowledge of the polarization amplitudes, the ellipticity of the pulsar and the orientation of the pulsar with respect to the line of sight to the Earth can be determined. This depends on first identifying a gravity wave signal, then measuring its parameters.

For the purposes of detection, we were only interested in calculating the energy of the gravitational wave. Specifically, the energy flux is given by

$$-T_{0z'} = \frac{\pi}{4}\frac{c^3}{G} f_s^2(a^2 + b^2)$$

where $T_{0z'}$ is the stress-energy tensor for the wave, c is the speed of light and G is the gravitational constant. Calculation of the signal energy took place in three stages. First, the square of the absolute value of each of the filtered outputs was formed for one 28 hour data record. At the same time, the signal to noise ratio was calculated for each of the four filters from Eq. 3.41. This was done for each data record analyzed. The signal to noise ratio needed to be recalculated for each data record so that the change in detector sensitivity as a signal was Doppler shifted across a mode resonance would be accounted for. Since it was not possible to track the phase of the gravity wave from one data record to the next (see section 3.2.2), the individual records were statistically independent and the squared filter outputs,

as well as the calculated signal to noise ratios, were added together:

$$\begin{aligned} |\mathbf{q}|_j^2 &= \sum_{i=1}^{S} |q_i|_j^2 \\ \rho_{j\tau}^2 &= \sum_{i=1}^{S} \rho_{ij}^2 \end{aligned} \tag{3.44}$$

where j refers to the jth filter, i refers to the ith data record, and there were S total records.

Next, each filtered output was related to a strain amplitude by

$$h_j(f_s) = \sqrt{|\mathbf{q}|_j^2} \; / \; \rho_{j\tau}^2$$

where f_s is the assumed signal frequency. This ranged in 10 micro-Hertz steps from 896.3-897.3 Hz for the minus mode and from 919.76-920.76 Hz for the plus mode.

Finally, the estimated amplitudes from each filter were combined in quadrature,

$$h^2(f_s) = \sum_{j=1}^{4} h_j^2(f_s) = a^2 + b^2 \tag{3.45}$$

which is, to factors, the measured energy of a gravity wave with polarization amplitudes a and b. In the following text we will usually refer to the strain amplitude at a particular signal frequency, as given by the square root of Eq. 3.45, and not the energy of the gravity wave.

The analysis just described is essentially what is called *envelope* detection in signal processing. For a sinusoidal signal of unknown phase, the best chance of detection occurs if two filters are applied to the data. One filter assumes a signal

phase of 0 radians (in-phase). The other filter assumes a signal phase of $\pi/2$ radians. The two outputs are then squared and added together. This technique assumes that the signal envelope is completely known, which was not the case for this search. As the phase of the carrier wave and the envelope were unknown, both were reduced to in-phase and quadrature components, which were then squared and added together.

3.5.2 CPU Reduction

Even though this search was directed towards only a small section of the sky, it was still cpu intensive on a DEC 3000 AXP. Applying 2×10^5 different filters, where each new set of filter coefficients requires a Fourier transform on a time sequence of 10^5 elements, is prohibitively time consuming.

We determined, however, that it was not necessary to calculate the amount of Doppler shift experienced by an arriving signal for each assumed signal frequency. Instead, calculating the phase shift at three specific signal frequencies per mode was sufficient to approximate the phase shift for the other signal frequencies. The argument goes as follows: For a signal from 47 Tuc, the maximum fractional Doppler shift of an incoming signal over the course of a year is

$$\frac{\delta f}{f_s} \sim \pm 5 \times 10^{-5}.$$

To approximate all phase shifts in a range of signal frequencies $f_s \pm \Delta f_s$ with a calculation at a single signal frequency, then the error made must be less than the

frequency resolution of the search. Defining the error as

$$\delta f(f_s \pm \Delta f_s) - \delta f(f_s) = 5 \times 10^{-5} \Delta f_s$$

we have the maximum range of signal frequencies over which the approximation is valid is given by

$$|\Delta f_s| < .2 \text{ Hz}.$$

The Doppler shift was calculated at 896.45 Hz, 896.80 Hz and 897.15 Hz for the minus mode and 919.91 Hz, 920.26 Hz and 920.61 Hz for the plus mode.

The second procedure for reducing the computational costs was to exploit the fact that only the Fourier coefficients of the signal envelope within a millihertz of the assumed signal frequency were non-zero. This reduced the number of coefficients of $\tilde{C}_k$ and $\tilde{D}_k$ from 10^5 to roughly 200, a substantial savings in the computational effort.

Using both of the described techniques, the cpu time needed to make a complete search of one data record (28 hours) was roughly 1.5 hours. Without these techniques, the estimated cpu time for the same analysis would be over a year.

3.6 Candidate Signals

The final result of the analysis is a "spectrum" of strain amplitude versus signal frequency, as shown in Fig. 3.15 for the minus resonant mode and Fig. 3.16 for the plus resonant mode. It is important to remember that the abscissa for both plots is *not* a Fourier frequency, but rather the *assumed* frequency of the gravitational

wave. Both plots were made by averaging 30 data records from the first 3 months of 1994. Unlike Allegro's duty cycle for burst events, which was near 95%, only about 40% of the data was available for the CW search. This is partially due to a conservative approach to utilizing "questionable" data and partially due to the unanticipated data losses due to the WWVB clock discussed in section 3.4.

From Fig. 3.15 and Fig. 3.16, the noise floor of the strain amplitudes is a few times 10^{-24}, which is very close to the expected maximum strain for CW radiation from 47 Tuc (see section 3.1.1). To lower the noise floor would require coherently averaging over time-scales longer than 28 hours. As described in section 3.2.2, this means replacing the existing HP function generator. There are significantly more stable frequency generators available than is currently being used on Allegro, and at the time of writing there are plans to purchase a much better frequency standard.

If the strain value at one (or more) signal frequencies was significantly larger than the others (an "outlier"), it would be a candidate for a CW signal. There was one outlier near the minus resonant mode with a strain amplitude of roughly 1.2×10^{-23} at $f_s = 896.56$ Hz. There were three outliers near the plus resonant mode at signal frequencies f_s=920.2804 Hz, 920.2807 Hz and 920.4058 Hz. The respective strain amplitudes are 4.6×10^{-24}, 4.5×10^{-24}, and 5.0×10^{-24}.

To get a clearer idea of how significantly these "potential signals" deviated from their measured distributions, we normalized the strain amplitude in each frequency bin to its expected value. The histogram of the resulting normalized spectra for the minus mode is shown in Fig. 3.17. The previously identified outlier is now clearly

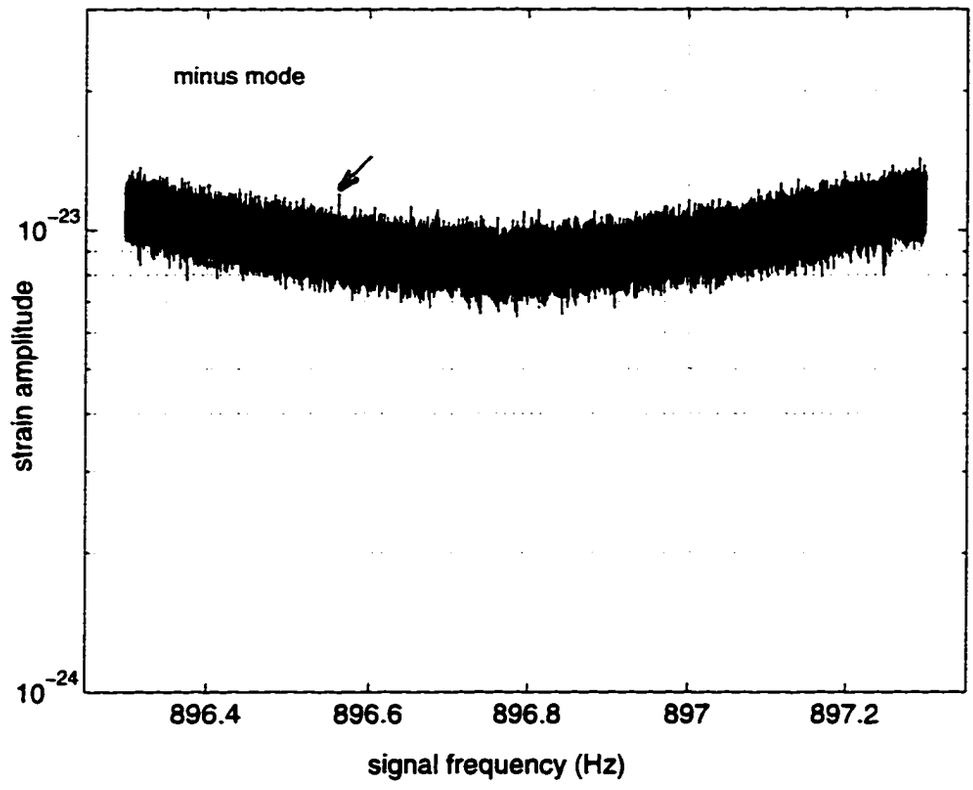

Figure 3.15: The strain amplitude at each assumed signal frequency near the minus resonant mode. The arrow points to the CW signal candidate.

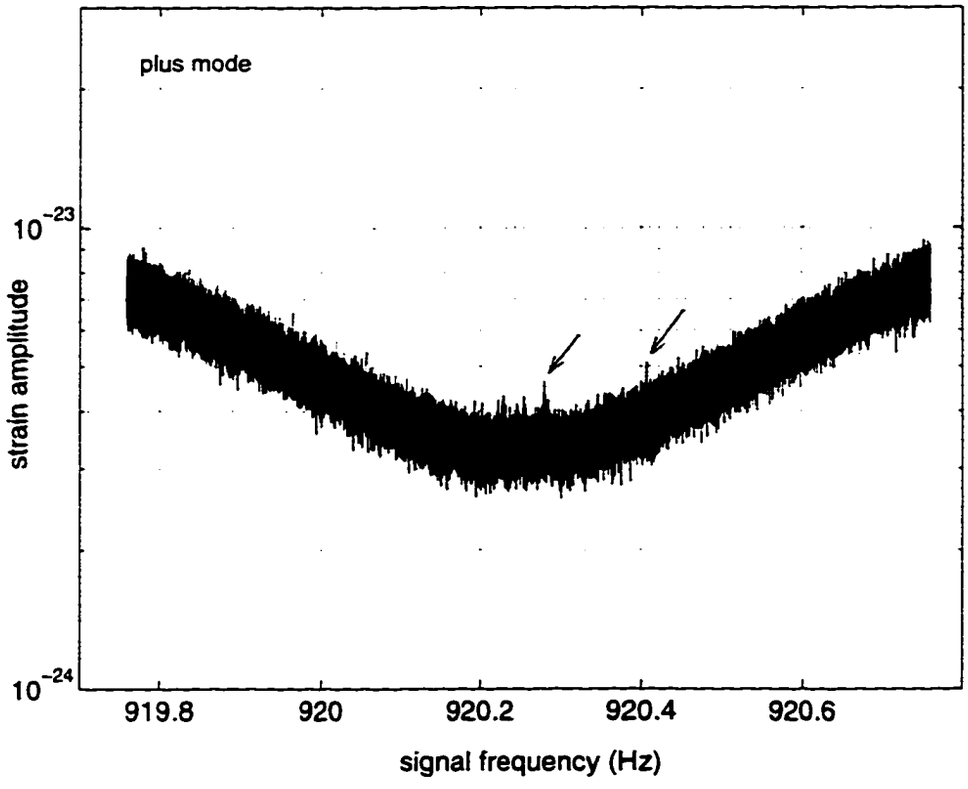

Figure 3.16: The strain amplitude at each assumed signal frequency near the plus resonant mode. The lower values of the strains relative to the minus mode are due to the higher mechanical Q of the plus mode. The arrows point to CW signal candidates.

seen to be outside the given distribution, but not very far outside, being only 1.8σ away from the mean. A similar histogram for the plus mode again clearly shows the outliers to be $1.8\sigma - 2\sigma$ away from the mean of the distribution.

None of the outliers from either mode are significant as gravity waves at this stage of the analysis. However, as more data gets analyzed and more records averaged together the variance in the strain amplitude from one frequency bin to the next will decrease while any signal will slowly accumulate. A real gravity wave signal in one (or more) bins will therefore continually move away from the distribution produced by the majority of bins, which contain only noise (we do not expect the detector to be dominated by sources of CW radiation from 47 Tuc).

We performed one test on the analyzed data to determine if the outliers were genuine CW candidates. We do not expect a real CW signal to appear in any one data record, as it is only through repeated averaging that the signal is expected to distinguish itself. Therefore, if any of the observed outliers appeared strongly in one record or a small subset of records, then it was not due to the CW signal we were searching for. By this reasoning, the two candidates at 920.2804 Hz and 920.2807 Hz are not CW signals. Almost all the observed amplitude appears in the data record taken from days 10-11 of 1994. It is unclear whether this is due to the data itself or a failure of the analysis on this day. The other candidates at 896.56 Hz and 920.41 Hz do not appear particularly strongly in any one data record and therefore remain viable candidates for CW signals.

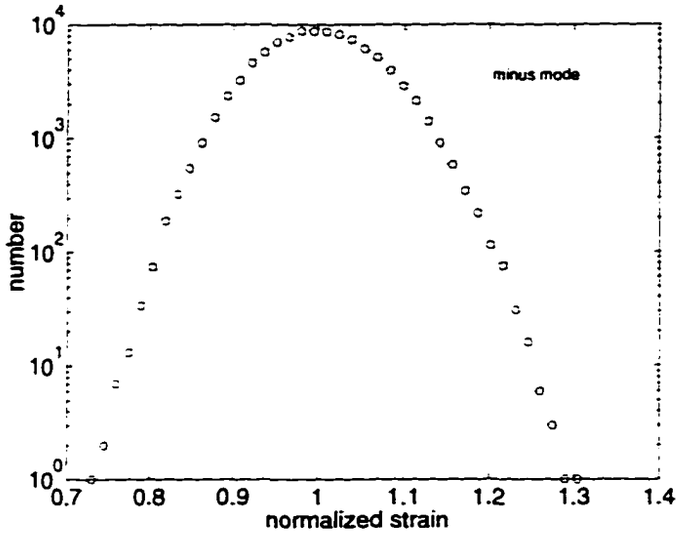

Figure 3.17: Histogram of the normalized spectrum for the signal frequencies near the minus mode.

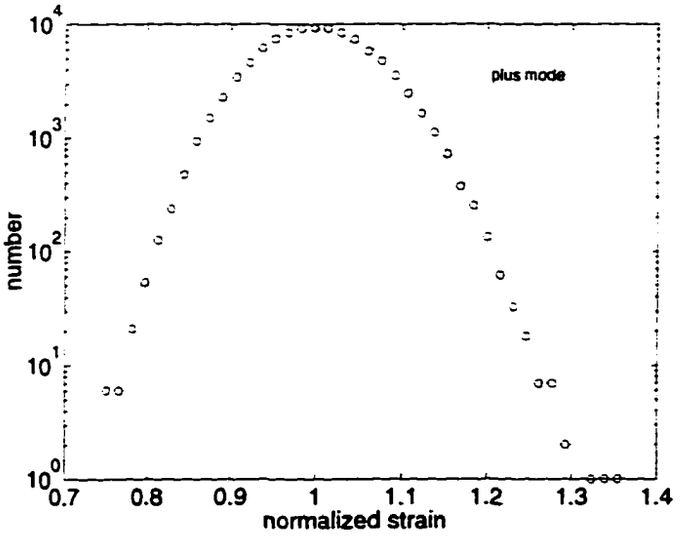

Figure 3.18: Histogram of the normalized spectrum for the signal frequencies near the plus mode.

Chapter 4

Summary

The first half of this dissertation introduced the Allegro gravitational wave detector. We described the data acquisition system and the analysis procedures used to look for burst events. Creation of the optimal filter for bursts was discussed in detail. including calibration of the filter coefficients. Uncertainties in assigning a time and energy to an event due to stationary noise were calculated and shown to match the data. setting the windows for both quantities in coincidence searches.

The second half of this dissertation detailed the search for a continuous gravitational wave (CW) signal. The expected signal from a pulsar in the globular cluster 47 Tucanae was determined, including amplitude modulation and frequency shifting of the CW signal due to the Earth's orbital and rotational motion. Interaction of the CW signal with Allegro was described. We described the effects of unusable or missing periods of data on the analysis and their handling. A statistical argument was shown to lead to the theory of optimal filtering and the optimal filters were applied to the data. Data from the first three months of 1994 was analyzed at

roughly a 40% duty cycle. No detection was claimed, but several candidate signals were identified. The analysis put a constraint of 3×10^{-24} on the amplitude of possible CW signals from 47 Tucanae.

The next step in this project is simply to continue the analysis on the rest of the available Allegro data. This will allow for further study of the CW candidates already identified, as well as produce new candidates.

References

[1] J. Weber. Phys. Rev., 117, 306, (1960).

[2] J. Weber. Phys. Rev. Lett., 22, 1320. (1969).

[3] W. M. Fairbank, W. O. Hamilton, and C. W. F Everitt, in *Relativity*, edited by M. Carmelli, S. I. Fickler, and L. Whitten (Plenum Press, New York, 1970).

[4] H. J. Paik. Ph.D. Dissertation. Stanford University. (1974).

[5] W. O. Hamilton, in *Proceedings of the Sixth Marcel Grossmann Conference on General Relativity and Gravitation*, edited by H. Sato and T. Nakamura (World Scientific Publishing Co., Singapore. 1992).

[6] P. Astone et al. *Physical Review D*, 47, 362 (1993).

[7] D. G. Blair et al. *Phys. Rev. Lett.*, 74, 1908 (1995).

[8] R. Forward. General Relativity Gravitation 2, 149, (1971).

[9] W. W. Johnson and S. M. Merkowitz. *Phys. Rev. Lett.*, 70, 2367, (1993).

[10] A. Abramovici et al. *Science*, 256. (1992).

[11] A. Giazotto, in *Proceedings of the Seventh Marcel Grossmann Conference on General Relativity and Gravitation*, edited by R. Jantzen and G. Keiser (World Scientific Publishing Co., Singapore, 1996).

[12] P. Bender et al. *LISA: Laser Interferometric Space Antenna for the Detection and Observation of Gravitational Waves, pre-phase A report.* Max-Plank Institut für Quantenoptik Internal Report 208 (1995).

[13] J. H. Taylor and J. M. Weisberg. Further experimental tests of relativistic gravity using the binary pulsar psr 1913+16. *The Astrophysical Journal*, 345:434, (1989).

[14] E. Amaldi et al. *Astron. Astrophys.* 216, (1989), 325-332.

[15] P. Astone et al., in *Proceedings on the X Italian Conference on General Relativity and Gravitational Physics*, edited by M. Cerdonio, R. D'Auria, M. Francaviglia and G. Magnano (World Scientific Publishing Co., Singapore, 1994).

[16] T. Suzuki, in *Proceedings of the First Edoardo Amaldi Conference on Gravitational Wave Experiments*, edited by E. Coccia, G. Pizzella, and F. Ronga (World Scientific Publishing Co., Singapore, 1995).

[17] T. M. Niebauer et al. *Physical Review D*, 47, (1993), 3106-3123.

[18] E. Ford et al. Evidence from quasi-periodic oscillations for a millisecond pulsar in the low mass x-ray binary 4U 0614+091. *Los Alamos National Archive*, astro-ph/9010110 15 October 1996.

[19] E. Mauceli et al. The Allegro gravitational wave detector: Data aquisition and analysis. *Physical Review D*, 54, (1996), 1264-1275.

[20] N. Solomonson, W. O. Hamilton, and W. Johnson. Construction and performance of a low noise inductive transducer for the Louisiana State University gravitational wave detector. *Rev. Sci. Instrum.*, 65(1):174, (1994).

[21] A. V. Oppenheim and R. W. Schafer. *Digital Signal Processing*. Prentice-Hall, (1975).

[22] L. A. Wainstein and V. D. Zubakov. *Extraction of Signals from Noise*. Dover Press, New York, 1962.

[23] A. D. Whalen. *Detection of Signals in Noise*. Academic Press, New York and London, 1971.

[24] S. Boughn et al. Method for calibrating resonant-mass gravitational wave detectors. *Rev. Sci. Instrum.*, 61(1):1, 1990.

[25] R. N. Manchester et al. Discovery of ten millisecond pulsars in the globular cluster 47 Tucanae. *Nature*, 352, 219-221 (1991).

[26] J. H. Taylor et al. Catalog of 706 pulsars (1995 update). *ApJS*, 88, 529, 1993.

[27] H. Goldstein. *Classical Mechanics*. Addison-Wesley, Massachusetts, 1980.

[28] C. Miser. K. Thorne, and J. A. Wheeler. *Gravitation* W. H. Freeman and Co., San Francisco.

[29] K. C. B. New et al. Millisecond pulsars: Detectable sources of continuous gravitational waves? *ApJ*, 450, 757-763, 1995

[30] S. L. Shapiro and S. A. Teukolsky. *Black Holes, White Dwarfs and Neutron Stars.* Wiley, New York. 1983.

[31] L. S. Finn. Detection, measurement. and gravitational radiation. *The Physical Review D*, 46, 1992 5236-5249.

[32] A. Papoulis *Signal Analysis.* McGraw-Hill Inc.. New York, 1977.

[33] N. Solomonson. Ph.D. Dissertation. Louisiana State University. 1990.

[34] Z. Geng Ph.D. Dissertation. Louisiana State University, 1994.

Appendix A

Test of the CW Analysis

An artificial CW signal was added to the raw data from January 1-2 1994 to test the analysis procedures. The signal was a linearly polarized (plus polarization only) gravity wave at a source frequency of 920.51 Hz. The signal included both frequency shifting and amplitude modulation due to the Earth's orbital and diurnal motion, as described in section 3.1.2 and section 3.2. The amplitude of the gravity wave was chosen to be 10^{-21} so that it would appear above the noise in the spectrum of the raw data, as shown in Fig. A.1. The signal was added to the real data before the narrowbanding process, the combination of noisy data and signal was then analyzed as usual.

There are two features of the signal as it appears in the raw data to note: 1) The signal frequency has been red-shifted from its value in the wave frame (920.51 Hz) by 22 mHz. The observed shift away from the source frequency is due mostly to the orbital motion of the Earth. 2) The signal is spread over a bandwidth approximately 1 mHz and has a double peaked structure. Both are effects of

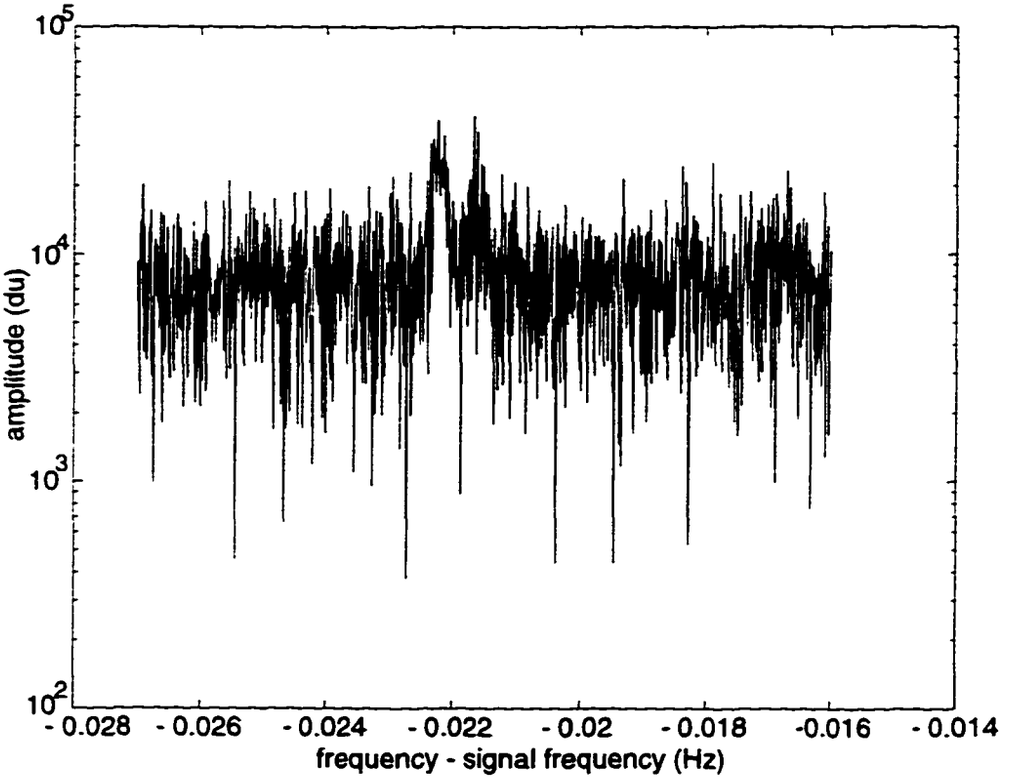

Figure A.1: The artificial signal in the raw Allegro data from Jan. 1-2 1994.

the Earth's daily rotation about its axis. As the detector rotates away from the source, the signal is red-shifted. Since roughly half the day is spent in this phase, the gravity wave possesses a lot of its energy at frequencies below "dc". Here "dc" is used to describe the signal frequency after the orbital shift has been included. There is a short transition period and then the detector begins to rotate towards the source, blue-shifting the signal. Since the second half the day is spent in this phase, the gravity wave also has a lot of energy at frequencies above "dc". The spectrum of such a signal will have the observed double peak structure.

The analysis routines are designed to produce a "spectrum" of measured signal amplitude versus signal frequency *in the wave frame*. A small section of the full spectrum is shown in Fig. A.2. If the analysis is working properly, the value of the measured strain amplitude at a signal frequency of 920.51 Hz should stand out from the amplitudes measured at all other signal frequencies. As can be seen from Fig. A.2, the maximum value of the spectra does occur at the frequency of the signal in the wave frame. There is also considerable amplitude in the adjacent frequency bins.

The "spreading" out of the signal is most likely due to the decision to analyze data in 28 hour sets. Spectral "leakage" is a well known phenomenon associated with Fourier transforming data sets of fixed length ($< \infty$). Components of data which are not periodic over the interval of the data set appear to "leak" out into frequency bins adjacent to the correct spectral value. Since the signal envelope is periodic with an interval of twelve hours (two cycles in 24 hours), the four hours of data left over can explain the large observed amplitudes at signal frequencies near the correct value.

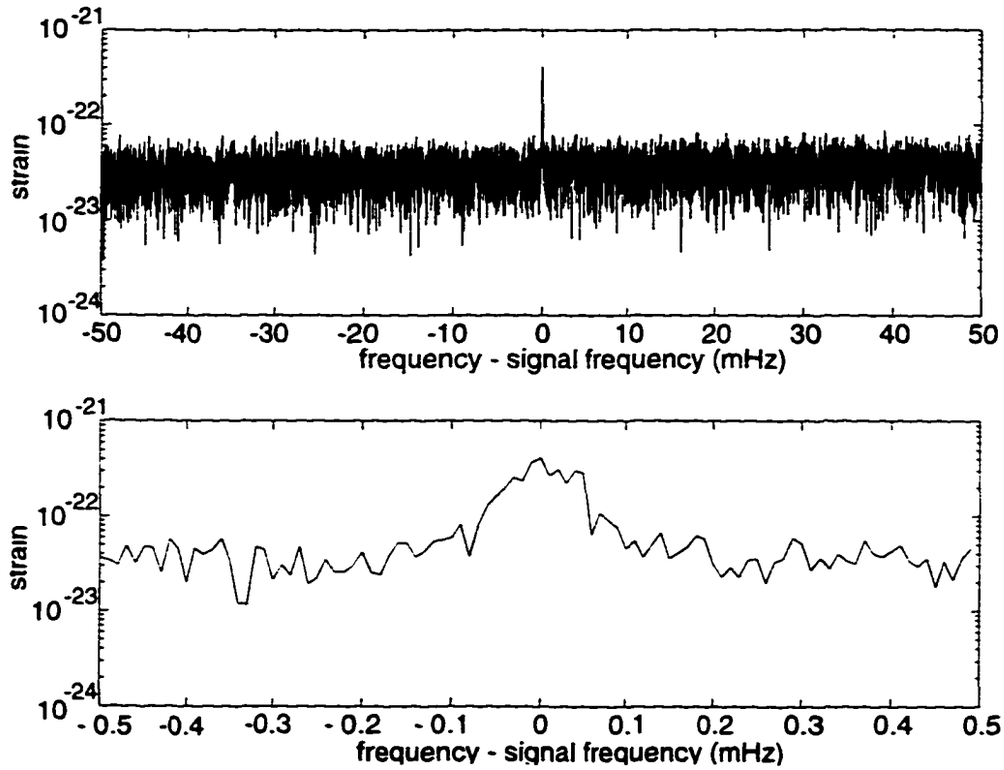

Figure A.2: The filtered output for a small portion of the plus resonant mode spectrum. The embedded signal of Fig. A.1 has clearly appeared at the correct frequency. The bottom plot shows the filtered output in more detail at the signal frequency.

The usual method of reducing this problem is to "window" the data with a Hanning (or similar) window. The windowing process tapers the data stream in the time domain so that the beginning and end of the data has amplitude near zero and the amplitude is maximum at the halfway point. We have chosen not to window our data because of the added complication it produces to calculating the optimal filter coefficients.

Appendix B

Source Location

The listed positions of the pulsars in 47 Tuc are only accurate to $\pm 4'$ in right ascension and $\pm 20''$ in declination around the listed values of 00:24:06 and -72:04:00 respectively (section 3.1.2). The data analysis assumes that the source is exactly at the listed position. If the source is instead slightly offset from the center, but still within the globular cluster, the frequency of the radiation will be mis-identified by the analysis. The amount of error depends on the distance of the actual source from the anticipated location. Figure B.1 shows the amount of this error as the actual source location is varied with respect to the anticipated location. The x-axis is the declination offset, in minutes of a degree. The y-axis is the offset in right ascension, in minutes of an hour. The position (0,0) corresponds to $\alpha_o = 00:24:06$, $\delta_o = -72:04:00$. The vertical dark band across the middle of the graph represents the region where the error in estimating the signal frequency is less than 10^{-5} Hz, or 1 bin. For comparison, the lightest regions at (-4,4) and (4,-4) involve a mis-identification of the signal by .15 mHz. A source at the expected declination

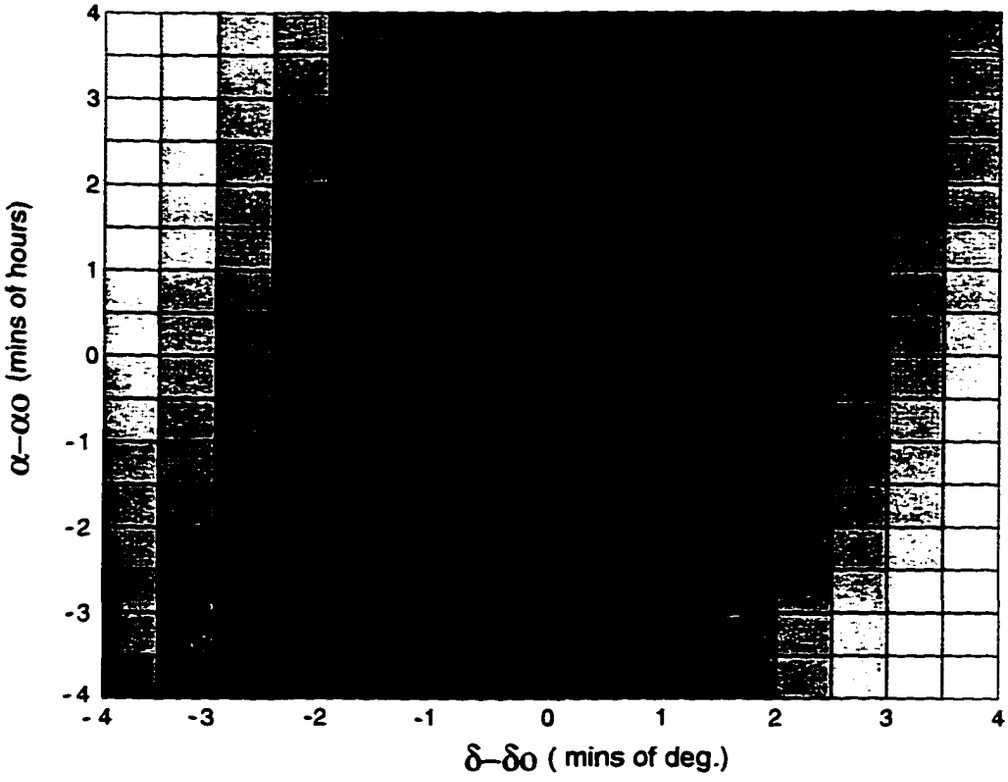

Figure B.1: The effects of uncertainties in the source location on the observed frequency of the gravitational radiation.

($\delta = \delta_o$) can be offset in right ascension from its anticipated location by roughly $\pm 1'$ before the signal frequency is mis-identified. If the source is at the anticipated right ascension, there can be an offset of only $\pm .25'$ in the declination before the observed signal frequency is shifted by one bin.

Appendix C

Programs

The following programs are all written in MATLAB. They are included as a helpful guide to those who might wish to continue the CW search.

DATA ANALYSIS PROGRAM CHAIN

CWAVE.M

[HOUSKEEPING PROGRAMS]

FIND_CW.M

FILT_FCN.M

SPECTRE.M AMPMOD.M ALIGN.M

ORBIT4.M

Y-FILES TO_TDT.M GR_ANGLE.M LMST.M

CWAVE.M - The main program to get the data off disk and into a form suitable for filtering (signal.m and filt _fcn.m). Reads in the data one block at a time. Forms the complex amplitude,anti-alias filters and resamples. Writes partial output (if not enough data yet to filter) to leftovers.mat and a full data set to an "ampl" file.

FIND_CW.M - loads in an ampl file. defines the sample times. sends the appropriate data to FILT_FCN.M and then writes an output file of the filtered data and SNR for each mode and polarization.

function [Oplus.Ocros.mplus.mcros.res_f] = FILT_FCN(fc.ampl.dec_time.year.day_of_year.N1.c_factor) This is the workhorse filtering program. Creates the optimal filter components (signal from ampmod.m. noise PSD from norb.m and align.m) and applies them to the data. Also calculates the power signal to noise ratio for the particular signal and noise PSD. Data is put into the proper form by cwave.m.

fc - center frequency of the mode to be filtered

ampl - time sequence of the mode amplitude to be filtered

dec_time - sample times (s) from start of year

N1 - the non-zero Fourier comps. of the signal

c_factor - conversion from amps^2 to du^2 (gotten by scaling white noise levels of PSD from model and data).

function [total time delay,sinsqrd,costwophi,sintwophi] = ORBIT4(year,day_of_year,dec_time); Calculate the vector from the solar system barycenter (SSB) to the center of mass of the detector, the time delays due to orbital motion around the sun, rotation and GR. Report back the time delays (with respect to the SSB) and the reception patterns.

function [A,B] = AMPMOD(dec_time,sig_approx,year, day_of_year) calculates the complex envelope of the signal. specially designed to be included in the optimal filter.

function [Sn,res_freq,R] = ALIGN(Z,f,fdata,R,Sn,fc) shifts the resonant peak from the model to match the "raw" spectrum which may drift due to temp. changes. Returns the shifted noise PSD and detector response.

Z - PSD of "raw" data

f - frequencies at which the model is evaluated

fdata - frequencies at which the data is evaluated

R - detector response at freqs f (from norb.m)

Sn - PSD of Gaussian noise at freqs f (from norb.m, 1sided)

fc - digital lockin ref. frequency

function [f.S] = SPECTRE(data.samp_rate,fref.fc) calculates the Fourier transform and the frequencies of the input data. Needs the lockin ref frequency, the digital lockin ref frequency and the sampling frequency.

data - time sequence of data

samp_rate - number of samples per second

fc - digital lockin ref. frequency

```
%   CWAVE.M - The main program to get the data off disk and into
%   a form suitable for filtering (signal.m/filt_fcn.m).  Reads
%   in the data one block at a time.  Forms the complex amplitude,
%   anti-alias filters and resamples.  Writes parital output
%   (if not enough data yet to filter) to leftovers.mat and a full
%   data set to an ''ampl'' file.

! set file/version_limit=2 leftovers.mat

filen = '94day002 ';
time_through = 2;

first_rec = 1;

year = eval(filen(1:2));
day_of_year = eval(filen(6:8));

outfile = [filen(1:2),'amp',filen(6:8)];
file = ['data2:[mauceli]',filen,'.dat'];
eval(['[dum,fref,fp,fm]=getpars',filen(1:2),'(filen(6:9));']);


%%%%%%%%%%%%%%%%%%%%%%%%%%%%%%%%%%%%%%%%%%%%%%%%%%%%%%%%%%%%%%%%%%%%%%%%%%%

%  daily affirmations

%  open the datafile
eof = 0; lockins = 0; numsamps = 0; lun = 1;
[lockins,numsamps,blocktype] = open_datafile(file,lun);
[label,x,y,s1,s2,veto,secs,lowf,eof] = ...
        readblock_type2(lun,1,lockins,numsamps,blocktype);
sampletime = label(18)/1000;
rsecs=[0:numsamps-1]'*sampletime;

last_rec = count_records(1,10000,lun,lockins,numsamps);
```

```
decm = 50;
new_sampl = numsamps/decm;
max_pos_data = 2.5e5;
if time_through == 1
 init
else
  load leftovers
end

%   set up the anti-aliasing filter for resampling
order=6;
[b,a]=butter(order,.016);

%%%%%%%%%%%%%%%%%%%%%%%%%%%%%%%%%%%%%%%%%%%%%%%%%%%%%%%%%%%%%%%%%%%%%%%%%%%%


%  examine the added vetos

%av_start = []; av_stop = [];
%gltcher = [];  num_gltchs = [];

%   find the added vetos for the day
%gltcher = find(fix(V2(:,1)) == day_of_year);
%num_gltchs = length(gltcher);
%if num_gltchs > 0;
%  av_start = V2(gltcher,2)/24 + day_of_year;
%   av_stop  = V2(gltcher,3)/24 + day_of_year;
%end


%%%%%%%%%%%%%%%%%%%%%%%%%%%%%%%%%%%%%%%%%%%%%%%%%%%%%%%%%%%%%%%%%%%%%%%%%%%%


%   load in prev. info and analyze one record at a time
recnum = first_rec;

while recnum <= last_rec
```

```
x=zeros(numsamps,1); y=x; secs=x; veto=x; time_in_rec=x;
i=[];  j=[];  k=[];  l=[]; i2=[];  j2=[];  n=1;

   %   read in one record of data
   [label,x,y,s1,s2,veto,secs,lowf,eof] = ...
      readblock_type2(lun,recnum,lockins,numsamps,blocktype);

   clear s1 s2 lowf

%   get UT time for the 1st sample of the record (in decimal days)
%   and the clock acc. code, then assign a time to each sample in
%   the record
   [utd,uth,utm,uts,acc] = get_ut(label);
   time_start_rec = utd + uth/24 + utm/(24*60) + uts/(24*60*60);
   time_in_rec = time_start_rec*(60*60*24) + rsecs;
   dec_time(recs_analyzed+2) = time_start_rec*(60*60*24);

%%%%%%%%%%%%%%%%%%%%%%%%%%%%%%%%%%%%%%%%%%%%%%%%%%%%%%%%%%%%%%%%%%%%%%%%%%%%

%   get the vetos

%  if the clock screws up, add the entire record to the veto
%  array, add 10 so that clock vetos are distinguishable from
%  other vetos.  Remember that secs goes from 0-9.992 0-9.992
%  in a good record

   remv = []; normal_jump=[]; ok_jumps=[]; screw_up=[];
   dif_secs = diff(secs);
   screw_up = find(dif_secs > (sampletime + .002) | ...
                   dif_secs < (sampletime - .002));

   normal_jump = find(dif_secs < -9);
   while n <= length(normal_jump);
     ok_jumps = find(normal_jump(n) == screw_up);
     remv = [remv;ok_jumps];
     n = n+1;
   end
```

```
        screw_up(remv) = [];
        if length(screw_up > 0)
          veto = veto + 10; tot_veto=61;
        end


        on_veto = find(veto>0);
        tot_veto = length(on_veto)*sampletime + tot_veto;

        clear dif_secs secs normal_jump ok_jumps screw_up


%%%%%%%%%%%%%%%%%%%%%%%%%%%%%%%%%%%%%%%%%%%%%%%%%%%%%%%%%%%%%%%%%%%%%%%%%%%%

        if (tot_veto<=60)

%       add in the signal
%      [td,gwx,gwy] = orbit_test(year,day_of_year,time_in_rec,fref);
%      x=x+5e0*gwx; y=y+5e0*gwy;


           in_p=zeros(numsamps,1); qd_p=in_p; in_m=in_p; qd_m=in_p;
                  in_c=in_p; qd_c=in_p;
           p_arg = zeros(numsamps,1); m_arg=p_arg; c_arg=p_arg;

           p_arg = exp(-sqrt(-1)*2*pi*(920.26-fref)*(time_in_rec));
           m_arg = exp(-sqrt(-1)*2*pi*(896.80-fref)*(time_in_rec));
           c_arg = exp(-sqrt(-1)*2*pi*(865.00-fref)*(time_in_rec));

           %  form the complex amplitude of the data
           z = x+sqrt(-1)*y;

           %  demodulate at plus, minus and cal. freqs
           [P,zip] = filter(b,a,(z.*p_arg),zip);
           [M,zim] = filter(b,a,(z.*m_arg),zim);
           [C,zic] = filter(b,a,(z.*c_arg),zic);

           %  resample the data
```

```
            P = P(decm:decm:numsamps);
            M = M(decm:decm:numsamps);
            C = C(decm:decm:numsamps);

            ampl_plus(i3:i3+new_sampl-1) = P;
            ampl_minus(i3:i3+new_sampl-1) = M;
            ampl_calib(i3:i3+new_sampl-1) = C;
            i3 = i3+new_sampl;

            recnum=recnum+1;
            recs_analyzed = recs_analyzed+1;

            if recs_analyzed == 5000
              nl = length(ampl_plus);
              if nl>max_pos_data
                first_sampl = new_sampl + 1;
                ampl_plus=ampl_plus(first_sampl:nl);
                ampl_minus=ampl_minus(first_sampl:nl);
                ampl_calib=ampl_calib(first_sampl:nl);
                dec_time=dec_time(2:length(dec_time));
              end
              outvars1 = [' ampl_plus ampl_minus ampl_calib'];
              outvars2 = [' recs_analyzed dec_time fref tot_veto'];
              eval(['save ',outfile,outvars1,outvars2]);
              init
    end
       else
          init
          recnum = recnum+1;
          disp('too many vetos'),disp([recnum-1 sum(veto)])
       end  % "if tot_veto ..."
if rem(recnum,100)==0
  disp([ recnum (tot_veto)])
  if acc>0
    disp(['clock warning!'])
  end
end
```

```
end  %  "while recnum<last_rec ..."

save leftovers ampl_plus ampl_minus ampl_calib i3 ...
    recs_analyzed dec_time zip zqp zim zqm zic zqc ...
    tot_veto fref
```

```
%    FIND_CW.M - loads in an ampl file, defines the sample times,
%    sends the appropriate data to FILT_FCN.M and then writes an
%    output file of the filtered data and snr for each mode and
%    polarization.


datafile = '94ampl019';
filter_range = 123920:124120;

eval(['load ',datafile]);
outfile = ['94ampl',datafile(7:9)];

%  make some room
clear ampl_calib

yr=eval(datafile(1:2));
doy=eval(datafile(7:9));

dec_time=dec_time(1)+[0:(1/2.5):1e5-(1/2.5)]';

[Omp,Omc,Mmp,Mmc,mres_f] = filt_fcn(896.80,ampl_minus, ...
   dec_time,yr,doy,filter_range);

[Opp,Opc,Mpp,Mpc,pres_f] = filt_fcn(920.26,ampl_plus, ...
   dec_time,yr,doy,filter_range);

outvars = ' Omp Omc Mmp Mmc Opp Opc Mpp Mpc mres_f pres_f';

eval(['save ',outfile,outvars]);

%!beep
```

```
function [Oplus,Ocros,mplus,mcros,res_f] = ...
                    filt_fcn(P1,P2,P3,P4,P5,P6);

%  function [Oplus,Ocros,mplus,mcros,res_f] =  ...
%    FILT_FCN(fc,ampl,dec_time,year,day_of_year,N1,c_factor);
%  This is the workhorse filtering program.  Creates the optimal
%  filter components (signal from ampmod.m, noise PSD from
%  norb.m/align.m) and applies them to the data.  Also calculates
%  the power signal to noise ratio for the particular signal and
%  noise PSD.  Data is put into the proper form by cwave.m.
%
%  fc = center frequency of the mode to be filterd
%  ampl = time sequence of the mode amplitude to be filtered
%  N1 = the non-zero Fourier comps. of the signal
%  c_factor = conversion from amps^2 to du^2 (gotten by scaling
%       white noise levels of PSD from model and data).

fc = P1;
ampl = P2;       clear P2
dec_time = P3;   clear P3
year = P4;
day_of_year = P5;
N1 = P6;              %  the non-zero Fourier comps. of the signal
c_factor = 2.27e25; %  from amps^2 to digital units^2

%   initialize some stuff
N=1e5;
zrs=zeros(N,1);
Oplus=zrs; Ocros=zrs;
mplus=zrs; mcros=zrs;

sig_approx_m = [896.45 896.80 897.15];
sig_approx_p = [919.91 920.26 920.61];
Df = .55;


%%%%%%%%%%%%%%%%%%%%%%%%%%%%%%%%%%%%%%%%%%%%%%%%%%%%%%%%%%%%%%%%%%%%%%%%%%%%
```

```
%   Fourier trans. the data, get the detector resp. and noise PSD
%   from the model.  Match to data to account for temp. drifts,...

[f,Z] = spectre(ampl,2.5,fc);  clear ampl

if fc==920.26

%   restrict the bandwidth to the interesting region, leave some
%   room so that the filter can operate on a full Hz
%   the model needs a slightly larger bandwidth (100 mHz) so that
%   it can be shifted to match the data.

  a1 = find(f>(fc-(.1+Df)) & f<=(fc+(.1+Df)));
  fp = f(a1);  clear a1

  a2 = find(f>fc-Df & f<=fc+Df);
  Z=Z(a2); f=f(a2); clear a2

  [Rp,Snp] = norb(fp,zeros(size(fp)));
  R = sqrt(c_factor)*conj(Rp);    % du (conjugation for filters)
  clear Rp
  Sn = c_factor*Snp;
  clear Snp

  f1=920.08;
  f2=920.44;

  [A,B] = ampmod(dec_time,sig_approx_p,year,day_of_year);
  [Sn,res_f,R] = align(Z,fp,f,R,Sn,fc);

else

  a1 = find(f>(fc-(2*.1+Df)) & f<=(fc+(.1+Df)));
  fm = f(a1);  clear a1

  a2 = find(f>fc-Df & f<=fc+Df);
  Z=Z(a2); f=f(a2); clear a2
```

```
  [Rm,Snm]=norb(fm,zeros(size(fm)));
  R = sqrt(c_factor)*conj(Rm);
  clear Rm
  Sn = c_factor*Snm;
  clear Snm

  f1=896.62;
  f2=896.94;

  [A,B] = ampmod(dec_time,sig_approx_m,year,day_of_year);
  [Sn,res_f,R] = align(Z,fm,f,R,Sn,fc);

end

%%%%%%%%%%%%%%%%%%%%%%%%%%%%%%%%%%%%%%%%%%%%%%%%%%%%%%%%%%%%%%%%%%%%%%%%

%  do the filtering

A = A(N1,:);
B = B(N1,:);
zrs = ((Z.*R)./Sn)/N;

s=max_dop_shift+1;          %  starting signal frequency
while f(s)<=f1
  A1=A(:,1);  B1=B(:,1);
  range = s-(1.25e5 - N1');
  s2=s-max_dop_shift;

  Oplus(s2) = abs(sum(zrs(range).*A1))^2;
  Ocros(s2) = abs(sum(zrs(range).*B1))^2;
  mplus(s2) = (1/N)*sum(abs(R(range).*A1).^2./Sn(range));
  mcros(s2) = (1/N)*sum(abs(R(range).*B1).^2./Sn(range));

  s=s+1;
end
while f(s)>f1 & f(s)<=f2
```

```
  A1=A(:,2);  B1=B(:,2);
  range = s-(1.25e5 - N1');
  s2=s-max_dop_shift;

  Oplus(s2) = abs(sum(zrs(range).*A1))^2;
  Ocros(s2) = abs(sum(zrs(range).*B1))^2;
  mplus(s2) = (1/N)*sum(abs(R(range).*A1).^2./Sn(range));
  mcros(s2) = (1/N)*sum(abs(R(range).*B1).^2./Sn(range));

  s=s+1;
end
while s<=N+max_dop_shift;

  A1=A(:,3);  B1=B(:,3);
  range = s-(1.25e5 - N1');
  s2=s-max_dop_shift;

  Oplus(s2) = abs(sum(zrs(range).*A1))^2;
  Ocros(s2) = abs(sum(zrs(range).*B1))^2;
  mplus(s2) = (1/N)*sum(abs(R(range).*A1).^2./Sn(range));
  mcros(s2) = (1/N)*sum(abs(R(range).*B1).^2./Sn(range));

  s=s+1;
end
```

```
function [f, S] = spectre(P1, P2, P3)

%  SPECTRE calculates the Fourier transform and the frequencies
%    of the input data.  Needs the lockin ref frequency, the
%    digital lockin ref frequency and the sampling frequency.
%
%  [f,S] = spectre(data,samp_rate,fref,fc)
%       data = time sequence of data
%       samp_rate = number of samples/second
%       fc = digital lockin ref frequency


data = P1;
samp_rate = P2;
fc = P3;

len = length(data);
dt = 1/samp_rate;
df = samp_rate/len;

z = fft(data)*dt;
S = [z(len/2+2:len);z(1:len/2+1)];
if rem(len,2)==0
    f = ((-len/2+1):(len/2))'*df + fc;
else
    f = (-(len-1)/2:(len/2-1))'*df + fc;
end
```

```
function [A,B] = ampmod(P1,P2,P3,P4);

%   function [A,B] = AMPMOD(dec_time,sig_approx,year,day_of_year)
%   calculates the complex envelope of the signal, specially
%   designed to be included in the optimal filter.

dec_time = P1;
clear P1

sig_approx = P2;
year = P3;
day_of_year = P4;
dt=.4;  % (s)

N=length(dec_time);
n=length(sig_approx);

A=zeros(N,n); B=A;
time_delay=zeros(N,1); phase_delay=zeros(N,n);
s_pat=zeros(N,1); cp=s_pat; sp=s_pat; S1=s_pat;
S2 = s_pat;

[time_delay,s_pat,cp,sp] = orbit4(year,day_of_year,dec_time);
S1 = s_pat.*cp;   clear cp
S2 = s_pat.*sp;   clear sp

for  i=1:n
   phase_delay(:,i) = exp(sqrt(-1)*2*pi*sig_approx(i)*time_delay);
   A(:,i) = fft(S1.*phase_delay(:,i))*dt;
   B(:,i) = fft(S2.*phase_delay(:,i))*dt;
end
clear time_delay phase_delay dec_time S1 S2

A = conj([A((N/2+2):N,:);A(1:(N/2+1),:)]);
B = sqrt(-1)*conj([B((N/2+2):N,:);B(1:(N/2+1),:)]);
```

```
function [Sn,mode_freq,R] = align(P1, P2, P3, P4, P5, P6)

% ALIGN shifts the resonant peak from the model to match the
%    "raw" spectrum which may drift due to temp. changes.
%    Returns the shifted noise psd and detector response.
%
% [Sn,res_freq,R] = align(Z,f,fdata,R,Sn,fc)
%    Z = PSD of "raw" data
%    f = frequencies at which the model is evaluated
%    fdata = frequencies at which the data is eval.
%    R = detector response at freqs f (from norb.m)
%    Sn = psd of Gaussian noise at freqs f (from norb.m, 1sided)
%    fc = center frequency

if nargin == 6
  Z = P1;
  fmodel = P2;
  fdata = P3;
  r = P4;
  sn = P5;
  fc = P6;
  T = 1e5;
else
  Z = P1;
  fmodel = P2;
  fdata = P3;
  sn = P4;
  fc = P5;
  T = 1e3;
end

%   the range to do the correlation
dr = find(abs(Z)==max(abs(Z)));
dr1=fdata(dr)-.01;  dr2=fdata(dr)+.01;

mr = find(sn==max(sn));
mr1=fmodel(mr)-.01;  mr2=fmodel(mr)+.01;
```

```
nd = (fdata(dr)-fmodel(mr))*T;
a3 = find( (fmodel > fdata(1)-1e-6) & (fmodel < fdata(1)+1e-6) );

%   isolate the relevent frequencies for the correlation
r1 = find(fmodel>=mr1 & fmodel<=mr2);
r2 = find(fdata>=dr1 & fdata<=dr2);

xc = xcorr(sn(r1),abs(Z(r2)));
lxc = length(r1);
mxc = find(xc==max(xc));
f_away = lxc-mxc-nd;
ind =  [(a3+f_away):(a3+f_away+length(fdata)-1)];

if nargout == 3
  Sn = sn(ind);
  ms=find(Sn==max(Sn));
  mode_freq=fdata(ms);
  R = r(ind);
elseif nargout == 2
  Sn = sn(ind);
  ms=find(Sn==max(Sn));
  mode_freq=fdata(ms);
elseif nargout == 1
  Sn = sn(ind);
end
```

```
function [total_delay,sinsqrd,costwophi,sintwophi] ...
                  = orbit4(P1,P2,P3);

%function [total time delay,sinsqrd,costwophi, ...
%           sintwophi] = orbit4(year,day_of_year,dec_time);
%
% Calculate the vector from the solar system barycenter (SSB)
% to the center of mass of the detector, the time delays due
% to orbital motion around the sun, rotation and GR.  Report
% back the time delays (with respect to the SSB) and the
% reception patterns.

year = P1;
day_of_year = P2;
dec_time = P3;   clear P3
N=length(dec_time);

%%%%%%%%%%%%%%%%%%%%%%%%%%%%%%%%%%%%%%%%%%%%%%%%%%%%%%%%%%%%%%%%%%%%%%%%%%%%

%   define astronomical parameters

%   source direction  (right ascention - hr:min:sec,
%           declination - deg:min:sec)

%  47 Tucanae
%RA_source = 0 + (24)/60 + 6/3600;
%dec_source = -1*(72 + (4)/60 + 0/3600);

%   galactic center
RA_source = 17 + (43)/60 + 0/3600;
dec_source = -1*(28.9);

%   the constants
deg_to_rad = pi/180;
hr_to_rad  = pi/12;

Astr_unit    = 1.49597870e11;           % one AU in meters
```

```
Earth_radius = 6362954;                  % at LSU, in meters
           c = 2.99792458e8;             % speed of light in m/s

Allegro_latitude  = 30.245*deg_to_rad;  % in rad., geocentric
Allegro_longitude = 91.179*deg_to_rad;  % in rad. (W)
          bar_dir = 40.4*deg_to_rad;    % rad W of N for bar dir.

%   change from GW dir of source to dir of propagation and make
%   everything radians for matlab

   prop_RA_rad   =  (RA_source + 12)*hr_to_rad;
   prop_dec_rad   =  (-1*dec_source)*deg_to_rad;

     c_lat = cos(Allegro_latitude);
     s_lat = sin(Allegro_latitude);
     cp_dec = cos(prop_dec_rad);
     sp_dec = sin(prop_dec_rad);

tdt_to_ut = 57.9579;  % in secs
utc_to_tdt = to_tdt(year,day_of_year);   % in secs
g1 = gr_angle(year);          % in degrees

%%%%%%%%%%%%%%%%%%%%%%%%%%%%%%%%%%%%%%%%%%%%%%%%%%%%%%%%%%%%%%%%%%%%%%%%%%%%

%  initialize a lot of stuff

dtime=zeros(size(dec_time)); tdt=dtime; ut1=dtime;
g = []; mt1=g; mx1=g; my1=g; mz1=g; mt=g; mx=g; my=g; mz=g;
mica_time=g; mica_x=g; mica_y=g; mica_z=g;

dec_time=dec_time/(24*60*60);       %  in dec. days of the year

%  Convert UTC to TDT (terrestrial dynamical time) and UT1
%  (both in dec. hrs)

        dtime = dec_time-day_of_year;
        if dtime(1)*24 < -24
          dtime = dec_time-(day_of_year-1);
```

```
        elseif dtime(1e5)*24>48
          dtime = dec_time-(day_of_year+1);
        end
tdt = (dtime)*24 + 32.184/(60*60) + utc_to_tdt/(60*60);
        ut1 = tdt - tdt_to_ut/(60*60);
        clear dtime

%  load the data from Mica (dec. hrs)
        eval(['y',num2str(year),'_',num2str(day_of_year-1)]);
        mt1 = (-1)*mica_time(7:-1:1);
        mx1 = mica_x;
        my1 = mica_y;
        mz1 = mica_z;

        eval(['y',num2str(year),'_',num2str(day_of_year)]);
        mt=mica_time(2:7); mx=mica_x(2:7); my=mica_y(2:7);
        mz=mica_z(2:7);

        eval(['y',num2str(year),'_',num2str(day_of_year+1)]);
        mica_time=[mt1 mt (24+mica_time(2:7))];
        mica_x=[mx1 mx mica_x(2:7)];
        mica_y=[my1 my mica_y(2:7)];
        mica_z=[mz1 mz mica_z(2:7)];

%  Calculate (from Mica data) the local (at the Allegro detector)
%  siderial time from ut1

        Allegro_sidtime = zeros(size(dec_time));
        lst_rad = zeros(size(dec_time));
 [Allegro_sidtime] = lmst(ut1,Allegro_longitude,year,day_of_year);
        lst_rad = Allegro_sidtime*hr_to_rad;
        clear Allegro_sidtime

%  Calculate from Mica data the (x,y,z) coords of the center of
%  mass of the Earth relative to the solar system barycenter

cme_xpos = zeros(size(dec_time)); cme_ypos = cme_xpos;
cme_zpos = cme_xpos; cmd_xpos = cme_xpos;; cmd_ypos = cme_xpos;
```

```
cmd_zpos = cme_xpos; Allegro_xpos = cme_xpos;
Allegro_zpos = cme_xpos; Allegro_ypos = cme_xpos;


cme_xpos = interp1(mica_time,mica_x,tdt,'cubic')*Astr_unit;
cme_ypos = interp1(mica_time,mica_y,tdt,'cubic')*Astr_unit;
cme_zpos = interp1(mica_time,mica_z,tdt,'cubic')*Astr_unit;

%  Calculate the (x,y,z) coords of the center of mass
%  of the detector relative to the center of mass of the Earth

cmd_xpos = c_lat*cos(lst_rad)*Earth_radius;
cmd_ypos = c_lat*sin(lst_rad)*Earth_radius;
cmd_zpos = s_lat*Earth_radius;

%  Form the vector from the SSB to the center of mass of Allegro

        Allegro_xpos = cmd_xpos + cme_xpos;
        Allegro_ypos = cmd_ypos + cme_ypos;
        Allegro_zpos = cmd_zpos + cme_zpos;

        clear cmd_xpos cmd_ypos cmd_zpos
        clear cme_xpos cme_ypos cme_zpos

%   Calculate the angle between the vector to allegro and the
%   source direction, the signal delay due to Earth's motion and
%   the total signal delay due to motion+GR

r=zeros(size(Allegro_xpos)); A_RA=r; A_dec=r;
total_delay=r;

   r = sqrt(Allegro_xpos.^2 + Allegro_ypos.^2 + Allegro_zpos.^2);
   A_dec = asin(Allegro_zpos./r);
   A_RA = atan2(Allegro_ypos,Allegro_xpos);

   clear Allegro_zpos Allegro_ypos Allegro_zpos

%   in Matlab atan2 runs from -pi to pi
```

```
if A_RA < 0
  A_RA = A_RA + 2*pi;
end

Dop_ang = cos(dec_source*deg_to_rad)*cos(A_dec).* ...
 cos(A_RA-RA_source*hr_to_rad) + sin(A_dec)* ...
 sin(dec_source*deg_to_rad);

%   the GR correction (degrees)
g = g1 + 0.98560028*day_of_year;

total_delay = r.*Dop_ang/c + 0.001658*sin(g*deg_to_rad);
clear r Dop_ang

%    Now calc. the reception pattern (see notes for terminology)

hr_ang = lst_rad - prop_RA_rad;
clear lst_rad

%   angle twx dir of prop. and bar axis
xdotz = cos(bar_dir)*s_lat*cp_dec*cos(hr_ang) - ...
        sin(bar_dir)*cp_dec*sin(hr_ang) - ...
        cos(bar_dir)*c_lat*sp_dec;

%   angle twx bar axis and gw polarization
xdotxA = cos(bar_dir)*s_lat*sp_dec*cos(hr_ang)- ...
         sp_dec*sin(bar_dir)*sin(hr_ang) + ...
         cos(bar_dir)*c_lat*cp_dec;

xdotxB = cos(bar_dir)*s_lat*sin(hr_ang) + ...
         sin(bar_dir)*cos(hr_ang);

sinsqrd = 1 - xdotz.^2;

costwophi = xdotxA.^2-xdotxB.^2;
sintwophi = 2*xdotxA.*xdotxB;
```

```
function    u_to_t = to_tdt(year,day_of_year);

%  1991 value as of Jan. 1
u_to_t = 26.00;

if ((year==92 & day_of_year>=183)|(year==93 & day_of_year<182))
   u_to_t = 27.00;
elseif ((year==93 & day_of_year>=182)| ...
            (year==94 & day_of_year<182))
   u_to_t = 28.00;
elseif (year==94 & day_of_year>=182)
   u_to_t = 29.00;
end
```

```
function g = gr_angle(year)

if year==91
   g = 356.38;
elseif year==92
   g = 356.13;
elseif year==93
   g = 356.85;
elseif year==94
   g = 356.60;
end
```

```
function  [Ast] = lmst(ut,Allegro_longitude,year,day_of_year)
const = 0.0657098243*day_of_year + 1.00273791*ut;
%  calc. the Greenwich mean siderial time in hrs
if year == 91
  GMST = 6.6106172 + const;
elseif year == 92
  GMST = 6.5947030 + const;
elseif year == 93
  GMST = 6.6444987 + const;
elseif year == 94
  GMST = 6.6285846 + const;
end
Ast = GMST - (Allegro_longitude*12/pi);
```

Appendix D

Letter of Permission

Most of chapter 2 was previously published in *Physical Review D.* It is reprinted with permission from *Physical review D* 54. 1264 (1996), "The Allegro gravitational wave detector: Data acquisition and analysis" by E. Mauceli et al. Copyright 1996 The American Physical Society. Included below is a copy of the letter requesting permission for reprinting as well as the letter granting permission.

January 6, 1997

Associate Publisher
The American Physical Society
One Physics Ellipse
College Park, MD 20740-3844

Dear Associate Publisher,

I am preparing my Ph.D. dissertation entitled: "Data Analysis of the Allegro Gravitational Wave Detector" to be reproduced and distributed by UMI Dissertation Services. I would appreciate your permission to use the materials in our paper: "The Allegro gravitational wave detector: Data acquisition and analysis", Evan Mauceli et. al, Physical Review D 54 (2), p. 1264-1275 July 1996. Credit to this journal will be given.

Thank you very much for your timely response.

Sincerely,

Evan Mauceli

LA St Univ
504 - 388 - 5860
504 - 388 - 5855 (fax)

The American Physical Society
One Physics Ellipse, College Park, MD 20740-3844 (301) 209-3200

March 7, 1997

Evan Mauceli
Louisiana State University

Dear Evan Mauceli:

This is further to your request for permission to use materials from The American Physical Society (APS) journals.

Permission is hereby granted for the one time reproduction -- in print only and as per the requirements indicated below -- of the following article:

see attached request

to appear in your Ph.D. dissertation entitled "Data Analysis of the Allegro Gravitational Wave Detector" to be reproduced and distributed by UMI Dissertation Services.

[XX] 1. The following credit line must appear in all copies (please fill in the information in CAPITAL LETTERS): "Reprinted (abstracted) with permission from FULL CITATION. Copyright YEAR The American Physical Society."

[XX] 2. NOTE: This permission does not apply to figures, tables, or other materials credited to sources other than the APS.

[XX] 3. Obtain the authors' permission to use the material. The author's address can be obtained from the article.

[ ] 4. Remit a permissions fee of $_____. Please make check payable to The American Physical Society. **PLEASE NOTE: PERMISSION IS NOT VALID UNTIL PAYMENT IS RECEIVED.**

Thank you for requesting permission to use materials copyrighted by the APS. Please do not hesitate to contact us should you have further questions.

Gail Gronlund
Marketing Assistant

Vita

Evan Anthony Mauceli was born on August 23, 1967, in Glen Cove, New York, to Eugene and Bronwyn Mauceli. In 1985 he graduated from Mascoma Valley Regional High School in Canaan, New Hampshire.

He attended the University of New Hampshire in Durham, New Hampshire and graduated with a Bachelor of Science degree in Physics in 1989. He spent a misguided 1989-1990 at the University of Connecticut with the idea of becoming a theoretical relativist. Upon learning that he could be involved in *experimental* general relativity, he transferred in the fall of 1990 to Louisiana State University. After passing his exams for admission to the doctoral program, he joined the Experimental Relativity Lab under the direction of his major professor, William O. Hamilton. He is currently a candidate for the degree of Doctor of Philosophy.

DOCTORAL EXAMINATION AND DISSERTATION REPORT

Candidate: Evan Mauceli

Major Field: Physics

Title of Dissertation: Data Analysis of the Allegro Gravitational Wave Detector

Approved:

Major Professor and Chairman

Dean of the Graduate School

EXAMINING COMMITTEE:

Date of Examination:

May 8, 1997